Design and Development of a Torsional Ventricular Assist Device

Submitted in partial fulfillment of the requirements for

the degree of

Doctor of Philosophy

in

Biomedical Engineering

Elaine Soohoo

B.S., Bioengineering, University of California Berkeley
M.S., Biomedical Engineering, Carnegie Mellon University

Carnegie Mellon University
Pittsburgh, PA

January 2019

Acknowledgments

I am truly grateful for the support and guidance of all those involved in my journey towards this doctoral degree. Many thanks to my doctoral advisor, Professor Dennis R. Trumble, PhD for offering me the opportunity to be your first student. Your flexibility and support of my various pursuits has ultimately made it a well-rounded and gratifying experience. Also, thank you to the members of my thesis committee —Professor James F. Antaki, PhD, Professor Keith Cook, PhD, Dr. Walter McGregor, MD, and Professor Conrad Zapanta, PhD —for lending their time and expertise to ensure that this thesis meets the highest standards of scholarship set by the Department of Biomedical Engineering at Carnegie Mellon University. To Jim, Keith and Conrad especially, I appreciate all of the opportunities you have given me to grow in different teaching and leadership roles, the many conversations over the years, the introductions you have made for me, and the doors you have opened for me.

I would also like to thank the many collaborators who helped make this work possible: *(UC San Diego)* Professor Andrew McCulloch, PhD, Professor Jeff Omens, PhD, *(John Hopkins)* Professor Sung Hoon Kang, PhD, Ozan Erol, PhD, *(Carnegie Mellon)* Professor Newell Washburn, PhD and Professor Stefanie Sydlik, PhD.

I especially would like to express my great appreciation for Dr. Lewis K. Waldman, PhD for his time, expertise, and patience in working with me. Without you, none of this work would have been possible, and I have learned and grown so much from working with you.

Also, I would like to thank the sources of funding that made this work possible: ***The National Institute of Biomedical Imaging and Bioengineering*** – Computational and In Vivo Analysis of Applied Apical Torsion for Cardiac Support (5R21EB017807-02), University of Pittsburgh's Training in Biomechanics in Regenerative Medicine (5T32EB003392-10) – and

Innovation Works – University Innovation Grant (2012W.CZ01551E-1). I would also like to express my sincere appreciation to Mr. Bradford Smith and Mrs. Diane Smith and Mr. Ting-Lung Liang and Dr. Tung Au for their generosity in establishing the ***Bradford and Diane Smith Fellowship*** and ***Liang Ji-Dian Graduate Fellowship,*** respectively, at Carnegie Mellon University, which helped to fund the first and last years of my graduate studies.

Thank you, also, Kristin Kropf, Maryia Rakach, Misti West, and Keri Baker for all of your support and advice, and my lab mates – Jooli Han, Edgar Aranda-Michel, Anne Alcasid, Hsuan "Michelle" Ma, Satyajit Balial, and Mathew Kubala – for all of your help and hard work. I would especially like to thank my undergraduate (and now masters) student, Molly Kaissar, for the time and effort that she has put into our projects together. You have grown tremendously over the last few years, and it was been such a rewarding and great learning experience working with you.

I especially want to thank all of the patients, families, nurses, doctors, and coordinators that I have worked with these last few years. The experience, perspectives, and relationships (thank you Lisa Carey Lohmueller, Salim Olia, Ricardo Londono, Luke Ziegler, Dan Crompton, Blue Martin, Salem Kamal, Alex May, and Marty Hashchak) that I have gained have been incredibly meaningful, and I greatly appreciate Dr. Rick Schaub, PhD and the Artificial Heart Program at the University of Pittsburgh Medical Center for the opportunity.

On a more personal note, I would also like to acknowledge all of the friends and family that have supported me through my academic journey. To my cohort – Stefanie Baker, Angela Lai, Andrew Lee, David Li, Caitlin Malesick, and Rei Ukita – I'm very glad to have gone through this experience with you and grateful for the friendships that we have made. To my PhD elders – Molly Blank, PhD, Rebecca Duffy, PhD, Rachelle Palchesko Simko, PhD, and

Stephanie Wong-Noonan, PhD – thank you for always being such group of strong and wise women that I could look to for advice, reassurance, and good company. To my Big Brothers, Big Sisters little, Isabelle Novak, thank you for being such a great little sister and exploring Pittsburgh with me. To the friends that I've made at Carnegie Mellon and in Pittsburgh along the way – Stephen Liu, Samson Huang, Drew Hackman, Maxwell Li, Connie Yen, Jenny Shi, Derek Lau, Cameron Low, Joseph Robertson, Ben Antoine, Kiera Davis, Kameron Bradley, Brent Ifemembi, Kevin Huang, Brandon Light, Dan Garcia, Edmund Chow, Travis Carless, and Samuel Kim– thank you for helping to make Pittsburgh feel more like home. Also, big shout out to the best IM basketball team at CMU, Cam, Joe, Kiera, Kam, Brent, Nate, Kevin, Nikki, Dan, Brandon, Lindsay, Kajae, and Edmund, for all those IM basketball championships shirts during my time here. To my friends from home – Margaret Yu, Winne Yan, Adele Zhang, Joanna Burtner, Camellia Ching, Erika Quan, Jeffrey Yang, Ivan Chan, Nathan Ho, Marc Tsukahira, Ryan Kageyama, Teryn Hara, Melissa Ho, Nicole Louie and Jaclyn Chan – thank you for always making time for me on the rare occasions I'm home and picking up the phone and being there for me, despite the 3 hour time difference. Thank you to my cousins Stephanie, Diane, and Derek Soohoo, for always reaching out and checking on me, especially when I least expect it. To my baby cousins Meiling, Jacquie, Jaylynn, and Amy Tan, thank you guys for all the laughs (and always forgetting that there is a 3 hour time difference when you call me) and keeping me young and hip over the years.

To Nathanuel Frezzell, thank you for being such a wonderful, supportive partner through this journey, especially in these last few stressful months. You have been such an important part of my experience at Carnegie Mellon since the very beginning, and I'm very grateful that through everything, our foundation of friendship has remained strong.

I would like to express my deepest gratitude to my Mom and Dad– Liping Beatrice Tan Soohoo and Yiuting Oliver Soohoo – and my grandparents – Zhong Chang Tan and Zhan Rong Sun – who have, without a doubt, raised me to be the woman that I am today. Grandma and Grandpa, thank you for everything that you have done over the years for me, from picking me up from school, making sure I always had my favorite snacks (sometimes, too much so), taking me to my tennis practices and basketball games, or always having my back so I wouldn't get in too much trouble for not practicing piano (sorry, Mom). Your work ethic, patience, and ability to give everything to your children and grandchildren have taught me so much. Mom, thank you for *literally* everything. You are the epitome of a humble, strong, and selfless woman, and I have learned so much about what it means to persevere, love unconditionally, and how to find a good deal. Although we may not always see eye to eye (I'm very sorry I did not pick up yours and dad's chemistry genes), I want you to know that there is no one I owe more to for my success.

我要向我的妈妈谭荔萍，我已故的爸爸司徒耀庭，我的外公谭宗暢和好婆（我从小给我外婆的昵称）孙占荣表示最深切的谢意。毫无疑问，是因为你们无私的付出让我成长为今天的我。公公和好婆，感谢你们多年来为我所做的一切，从背着我去幻儿园，开车送我读小学，中学，带我参加网球练习和篮球比赛，确保我总是有吃不完的最喜欢的零食，还有护着我不会因为不练钢琴而被妈妈指责。你们的耐心和愿意为孙女付出一切的爱心教会了我很多。妈妈，谢谢你为我付出的一切。你是一个谦虚，坚强，无私的女人的缩影，我从你身上学到了很多关于坚持不懈，无条件地爱，以及如何去全面考量找到最好的方案。虽然我们的看法可能并不总是一致，还有，很抱歉，我也没有继承你的化学基因，但我知道没有人比你为我的成长和成功而付出更多。最后，我想把这篇论文献给我已故的父亲。事情的结果总是令人惊讶，但我知道，不管怎么说，你总是会在天堂看护着我。

Lastly, I would like to dedicate this dissertation to my late father, Yiuting Oliver Soohoo. It is always surprising how things work out, but I know somehow, someway, you are and will always be here watching over me.

Abstract

Congestive heart failure (HF) is a complex disease that remains one of the leading causes of death in the world today, affecting over 5.5 million people in the United States alone and contributing to 1 in every 9 deaths nationwide. Currently, total heart transplantation is considered the most effective treatment for end stage HF, but there are on average 3000 donor hearts available annually, while there are more than 3500 patients on the transplant waitlist on any given day. For those patients, mechanical circulatory support (MCS), as a bridge-to-transplant (BTT) or more permanent destination therapy (DT), has been employed as an effective alternative for end stage HF patients. However, long-term use of these devices are associated with life-threatening complications, the most common of which are thromboembolic events triggered by artificial blood-contacting surfaces and hemolysis due to high shear stresses generated by blood flow through MCS devices.

The goal of this research is to develop a torsion-based ventricular assist device (tVAD) to support the failing heart as either a BTT or DT while eliminating the risk of thromboembolic complications common to all cardiac assist devices currently on the market by avoiding blood contact with artificial surfaces. This approach to cardiac support is inspired by the contractile mechanics of healthy human hearts, which produce a "wringing" motion during systole that allows the ventricles to empty more completely and reduces transmural stresses acting on the heart walls. This dissertation describes: 1) parametric computational simulations used to evaluate the effects of applied apical torsion (AAT) on global cardiovascular hemodynamics to determine optimal design parameters and their effects on regional cardiac biomechanics and determine the working limitations of such applied torsion therapy; and 2) development of a method for superficial attachment of the tVAD to the epicardium of the heart.

Results from the parametric computational simulations representing the most aggressive level of tVAD assist, where the applied rotation angle was 75 degrees and the device coverage area was 24% up the ventricle (from apex towards the base), yielded increases in left ventricular ejection fraction and stroke work of 49% and 72%, respectively, when compared to a baseline HF model. However, based on the evaluation of regional cardiac biomechanics at the epicardial and endocardial nodes at the base of the device and the ventricle, applied rotation angles of 65 degrees resulted in large increases in maximum principal strains (ΔE), where all nodes had $\Delta E \geq 0.40$, and increases in maximum principal stresses (ΔT), where nearly 75% of the nodes at $\Delta T > 100$ kPa. These results both suggest that supra-physiological levels of AAT could potentially cause damage to the myocardium. Additionally, results of lap-shear tests for the adhesion energies of candidate surgical adhesives suggest that the 316L stainless steel bonded with an octyl/butyl cyanoacrylate bioadhesive has the potential to secure the tVAD to the epicardium as it actuates on the heart.

Table of Contents

Acknowledgements ..... **iii**

Abstract ..... **vii**

Table of Contents ..... **ix**

List of Tables ..... **xiii**

List of Figures and Illustrations ..... **xv**

Chapter 1 Background and Significance **1**

1.1 Mechanical Circulatory Support (MCS) **1**

1.1.1 Clinical Significance 1

1.1.2 History of MCS 3

1.2 Problems Associated with MCS **5**

1.2.1 Contradiction Diagram Analysis 5

1.2.2 Failure Mode and Effect Analysis of VADs 8

1.3 Development of a Torsional Ventricular Assist Device **11**

1.3.1 Research Aim 1: Parametric Computational Simulations 12

1.3.2 Research Aim 2: Development of tVAD Attachment 13

Chapter 2 Preliminary Computational Parametric Studies **14**

2.1 Parametric Simulations **15**

2.1.1 Model Geometries 16

2.1.1.1 Procine Prolate Heart Model 17

2.1.1.2 Patient-Specific Prolate Heart Model 18
2.1.2 Passive Properties of the Prolate Model 21
2.1.3 Cellular Model 22
2.1.4 Circulatory Model 23
2.2 Results 27
2.2.1 Porcine Prolate Heart Model 27
2.2.2 Patient-Specific Prolate Heart Model 27
2.3 Discussion 30
Chapter 3 Parametric Study on Effects of tVAD Support on Cardiovascular Hemodynamics 31
3.1 Materials and Methods 32
3.1.1 Boundary Conditions 37
3.1.2 Passive Properties of Model 37
3.1.3 Dynamic Properties: Cellular Model 37
3.1.4 Circulatory Properties 39
3.1.5 Parametric Simulations 42
3.1.6 Stroke Work Calculations 42
3.2 Results 42
3.2.1 Varying Applied Apical Torsion 45
3.2.2 Varying Device Coverage Area 47
3.2.3 Effects on Pressure and Volume 48
3.3 Discussion 51
3.4 Study Limitations 53

3.5 Potential Advantages of tVAD Support 54

3.6 Future Work 55

Chapter 4 Computational Parametric Studies Investigating the Biomechanical Effects on Applied Apical Torsion for Cardiac Assist 57

4.1 Materials and Methods: An Extension of Parametric Computational Simulations 58

4.2 Biomechanical Results of Parametric Computational Studies 62

4.3 Discussion 76

4.4 Implications for Applied Apical Torsion as a Means for Cardiac Assist 78

4.4.1 Significance of Study Findings 78

4.4.2 Study Limitations 79

Chapter 5 Further Evaluation of the Effects of tVAD for Cardiac Assist 81

5.1 Parametric Timing Studies 82

5.1.1 Materials and Methods 82

5.1.2 Results of Parametric Timing Studies 83

5.2 Development of a New Patient-Specific Model 86

5.2.1 Materials and Methods 86

5.2.2 Results 87

5.3 Discussion 89

Chapter 6 Prototype of a Torsional Ventricular Assist Device 91

6.1 Device Components 92

6.1.1 Device Interface 93

6.1.2 Claw Scaffold 95

6.2 Proposed Implantation and Device Actuation 95

6.2.1 Device Implant and Deployment 95
6.2.2 Device Actuation 96
Chapter 7 Determining an Attachment Method for Epicardial MCS Devices 97
7.1 Qualitative Testing 98
7.1.1 Materials and Methods 98
7.1.2 Results 99
7.2 Quantitative Testing 100
7.2.1 Materials and Methods 100
7.2.1.1 Determining Adhesive Energy Requirements 100
7.2.1.2 Bioadhesive Shear Testing 101
7.2.2 Results 104
7.3 Significance 107
7.3.1 Future Work 109
Chapter 8 Summary and Conclusion 110
Appendix A Parametric Study on Effects of tVAD Support for Cardiovascular Hemodynamics 115
A.1 Example of Python Script Used for Computational Parametric Simulations 115
A.2 Comments on Image J for Stroke Work Calculations 118
Appendix B Determining an Attachment Method for Epicardial MCS Devices 119
B.1 Example of Python Script Used for Computational Parametric Simulations 119
References 121

List of Tables

Table 1: Hazard analysis "Risk Index" and acceptance criteria..... 9

Table 2: Failure mode and effect analysis for LVAD complications 10

Table 3: Parameters of nonlinear, transversely isotropic material law 22

Table 4: Parameters of cellular model used to simulate active state..... 23

Table 5: Parameters of circulatory model – prolate models..... 26

Table 6:Hemodynamic results for coverage area study - 15-element prolate model 28

Table 7: Hemodynamic results for applied rotation study - 18-element prolate model .. 29

Table 8: Cavity volumes as function of applied rotation angle for left ventricle..... 35

Table 9: Cavity volumes as function of applied rotation angle for right ventricle 35

Table 10: Parameters of circulatory models – bi-ventricular model 41

Table 11: Resutling left ventricular hemodynamics - bi-ventricular model 43

Table 12: Resutling right ventricular hemodynamics - bi-ventricular model 44

Table 13: Stress and strain component labels 59

Table 14: Locations of nodes in mesh of bi-ventricular heart model..... 60

Table 15: Resulting absolute maximum prinicpal strains 63

Table 16: Resulting absolute maximum prinicpal stresses 64

Table 17: Resutling hemodynamics for parametric timing studies..... 84

Table 18: Parameters of cellular model – EF 15% bi-ventricular model..... 86

Table 19: Resutling left ventricular hemodynamics - EF 15% bi-ventricular model 87

Table 20: Resutling right ventricular hemodynamics - EF 15% bi-ventricular model ... 88

Table 21: Adhesive energy requirements for tVAD attachement 100

Table 22: Adhesion energies from preliminary lap shear testing..... 106

Table 23: Adhesion energies from lap shear testing – adhesive cure time varied 106

Table 24: Adhesion energies from lap shear testing – hydrated adhesive cure time 107

Table 25: Perfect of lap shear tests that failed due to adhesive failure 107

List of Figures and Illustrations

Figure 1: Contradiction diagram analysis for ventricular assist devices 7

Figure 2: Motion of left ventricular twisting 12

Figure 3: Global rectangular Cartesian coordinate system, global prolate spheroidal coordinate system, and the local fiber coordinate system..... 17

Figure 4: 15-element prolate model of a porcine left ventricle..... 19

Figure 5: 18-element prolate model of a patient-specific left ventricle..... 20

Figure 6: Electrical circuit analog of a "simple closed-loop for left ventricle only" circulatory model 25

Figure 7: PV-loops of a simulation reaching a hemoydnamic steady state 26

Figure 8: Resulting PV-loops for experiments investigating effects of increasing coverage area on a 15-element pig prolate model 28

Figure 9: Resulting PV-loops for experiments investigating effects of increasing angles of applied rotation on an 18-element patient-specific prolate model 29

Figure 10: Computational model a bi-ventricular heart in heart failure in the no load state and nodes representing device coverage area..... 33

Figure 11: Dimensions of the bi-ventricular model..... 36

Figure 12: Fixed boundary conditions for the bi-ventricular model..... 38

Figure13: Electrical circuit analog of a "simple closed-loop for the left and right ventricles" circulatory model..... 40

Figure 14: Resulting ejection fraction as a function of applied rotation angles and device coverage area 45

Figure 15: Resulting peak systolic pressure as a function of applied rotation angles and device coverage area 46

Figure 16: Resulting stroke work as a function of applied rotation angles and device coverage area 46

Figure 17: Resulting end systolic volume as a function of applied rotation angles and device coverage area 47

Figure 18: Left ventricular PV-loops for the rotation study at large coverage area 49

Figure 19: Right ventricular PV-loops for the rotation study at large coverage area 50

Figure 20: Anterior-posterior view of epicardial and endocardial nodes at the base of the ventricles and the base of the tVAD 60

Figure 21: Left lateral view of epicardial and endocardial nodes at the base of the ventricles and the base of the tVAD 61

Figure 22: Maximum principal stresses and strains at nodes 81 and 86 for all rotation simulations at the large device coverage area..... 66

Figure 23: Maximum principal strains and their contributing component strains at nodes 14 and 98 for the 65 degree simulation 67

Figure 24: Strain renders on the deformed surfaces for the NoVAD heart failure model and 65 degree case 68

Figure 25: Maximum principal stresses and their contributing component stresses at nodes 14 and 98 for the 65 degree simulation 69

Figure 26: Stress renders on the deformed surfaces for the 65 degree case 70

Figure 27: Component stresses for the endocardial node at the anterior septal wall of the ventricular base 72

Figure 28: Component strains for the endocardial node at the anterior septal wall of the ventricular base 73

Figure 29: Component stresses for the endocardial node at the right ventricular free wall of the tVAD base 74

Figure 30: Component strains for the endocardial node at the right ventricular free wal of the tVAD base 75

Figure 31: Resulting PV-loops for the timing study where the peaktime was changed .. 84

Figure 32: Resulting PV-loops for the timing study where the simulated device was rotated to the orignial peaktime and then held for a prescribed amount of time 85

Figure 33: Resulting left ventricular PV-loops for a bi-ventricular model with an ejection fraction of 15%..... 88

Figure 34: Resulting right ventricular PV-loops for a bi-ventricular model with an ejection fraction of 15%..... 89

Figure 35: Solidworks rendering of second-generation tVAD attached to the apex of the heart 92

Figure 36: Exploded view of the proposed tVAD prototype..... 93

Figure 37: Glove-like device interface of tVAD 94

Figure 38: Collapsible claw-like mechanical actuator..... 94

Figure 39: Test set up of qualitative tests of bioadhesives for device attachment..... 99

Figure 40: Prepared substrate-adhesive-myocardium systems for lap-shear testing 102

Figure 41: Test set up for ASTM-F2255 lap-shear testing of bioadhesives 103

Chapter 1

Background and Significance

1.1 Mechanical Circulatory Support (MCS)

1.1.1 Clinical Significance

Congestive heart failure (CHF) is a complex disease that remains one of the leading causes of death in the world today, affecting over 5.5 million people in the United States alone and contributing to 1 in every 9 deaths nationwide [1]. The diagnosis, treatment and care of patients with CHF costs the United States nearly $32 billion annually [1]. Patients suffering from CHF have hearts that are unable to pump blood at levels sufficient to meet bodily requirements, which can lead to a variety of symptoms, including fatigue, shortness of breath, chest pain, swelling of the legs and feet, mental confusion/memory loss, and organ failure [2]. Factors contributing to the development of CHF in adults vary widely and can include irregular heartbeat (arrhythmia), cardiomyopathy, valve disease, coronary artery obstruction, and high blood pressure. These conditions damage the cardiac muscle over time, leading to increased stresses in the heart walls, decreased pumping efficiency, and significant reductions in cardiac output (CO).

When faced with choosing a treatment strategy for most severe heart failure conditions, patients currently have three main options: pharmacological management, blood pump therapy,

and total heart replacement (cardiac transplantation) [2,3]. The problem is that none of these interventions can be considered 'curative' and all have serious limitations with regard to long-term effectiveness and overall quality of life. Pharmacological interventions can help restore and manage heart function in the short term and are typically used to relieve the symptoms associated with CHF, but for many patients these therapies are unable to fully restore and support normal heart function over the long term.

Currently, total heart transplantation is considered the most definitive treatment for end stage CHF. However, the high costs of the procedure, the serious side effects associated with long-term use of immunosuppressive drugs, and the extremely limited pool of donor hearts eliminates this as a viable treatment option for most patients. For perspective, according to a 2017 Milliman Report, an estimated average $1.38 million were billed for procedures, hospital stays, and pharmacologic treatments per heart transplantation patient [4]. Furthermore, on any given day in the United States, there are over 3500 Americans listed on UNOS (United Network for Organ Sharing) waiting for a heart transplant [5], while there are approximately 3000 available donor hearts available annually with a general wait time of 191 days for transplant [4,6]. Although the number of available donor hearts annually has increased slightly over the last decade from 2,222 to 3,467 donor hearts , because of the high number of patients on the waitlist, patients sometimes do die before they are matched for a heart transplant [6]. For example in a 2016 study conducted by Trivedi et al. at the University of Louisville, of the 7371 patients listed on UNOS for a heart transplant, 1111 (15%) patients died waiting for a donor heart [7].

To address those treatment limitations, mechanical circulatory support (MCS) with cardiac assist devices have been employed as an effective alternative for end stage CHF patients.

The most common of these devices are ventricular assist devices (VADs), which can provide support via pulsatile or continuous flow pumps (depending on the design), and are typically implanted into the chest cavity to provide ventricular support of either the right or left or both ventricles (bi-ventricular support). These devices work to restore normal blood flow to the body by creating a parallel flow circuit that helps the heart to pump more efficiently by unloading the ventricles of weakened hearts. Furthermore, although VADs are typically indicated as a bridge-to-transplant therapy, there now exist FDA-approved VADs for either destination therapy or as a bridge to destination therapy. These devices traditionally consist of three main parts, a mechanical pump that is implanted in the patient, and an electronic controller and a power source, which are left external to the body and connected to the pump via a percutaneous driveline [8]. They are most often used to bridge very sick CHF patients to transplant, or for a growing population of patient, provide a destination therapy for those that do not qualify for a transplant [9]. Less commonly, VADs can also bridge patients towards recovery, but this only accounts for about 1.3% of VAD patients [10]. Unfortunately, long-term use of these devices are associated with life-threatening complications due to broken drivelines, driveline infections, catastrophic device failure, bleeding, and thromboembolic events.

1.1.2 History of MCS

The development of MCS devices began in the 1930's with the mechanical perfusion work of famed aviator Charles Lindbergh and Nobel laureate Alexis Carrel. Though rudimentary, their early glass extracorporeal perfusion device opened the door for future technologies [11]. With the advent of cardiopulmonary bypass in the 1950's, which allowed for more risky and complicated open-heart surgeries to be completed, the foundation was set for researchers to investigate how MCS devices could potentially support failing hearts for longer

periods of time [12]. The increased interest in MCS research led to the establishment of the Artificial Heart Program by the National Heart, Lung and Blood Institute (NHLBI) at the National Institutes of Health in 1964 and by 1966, the first LVAD was implanted in a patient by Dr. Michael Debakey, which provided paranormal support that lasted 10 days [12]. Since then, a number of MCS devices have come to clinical trial and some are now widely used clinically. Of these devices, the most common are the traditional VADs, such as the pulsatile machines like the Thoratec PVAD and Berlin Heart pediatric pump, or the continuous flow devices like the Heartmate II, Heartmate III, Heartware HVAD, Tandem Heart, Thoratec Centrimag and Pediamag, and Abiomed Impella's. However, parallel to the development of traditional VADs, there also exist a number of alternative cardiac assist devices such as the intra-aortic balloon pump, the Sunshine Heart C-Pulse extra-aortic pump, and the Acorn Heart – a passive cardiac device that sits on the ventricular epicardium.

Although the progress of mechanical devices for cardiac support has greatly improved over the last 60 years, the majority of clinically available MCS devices fit within one of two paradigms – pulsatile or continuous flow devices. The majority of these devices have seen their designs become more similar with many design features conserved regardless of the generation of the device or manufacturer, such as magnetically levitated bearings and centrifugal pump design for reduced hemolysis, and flow detection algorithms to monitor device flow outputs and abnormal device events such as device suck-down [13-15]. Furthermore, virtually all of the clinical devices currently available have two longstanding problems that persist – 1) complications arising from thrombolic events due to hemolysis and blood activation, and 2) risk of infection stemming from the need for a percutaneous drive line to power and control the pumps [16]. Indeed, these complications often result in compounded comorbidities that the

patients and clinicians must manage over time, which further proves the need for the development of new and better cardiac assist technologies.

1.2 Problems Associated with MCS

As previously mentioned, MCS can be an effective solution for end stage CHF patients, whether it be for immediate rescue of cardiogenic shock or longer-term solutions for patients needing bridge to transplant or a destination therapy. However, long-term use of these devices are associated with a whole host of life- threatening complications. In this section, a step-wise analysis of the problems associated with traditional MCS will be presented and evaluated in order to identify a potential novel solution.

1.2.1 Contradiction Diagram Analysis

A contradiction diagram can be very helpful in laying out the system of components of the VAD within the circulatory system, and the potential effects of the VADs on the body and vice versa in order to identify potential problems in the system. Inspired by the TRIZ inventive problem solving method, this analysis examines the contradictions between useful and harmful functions [17]. The relationships between positively (blue) and negatively (red) acting components are connected by arrows originating from the effector and pointing to the affected components. These arrows are also colored blue or red to indicate whether the relationships are positive or negative, respectively. In this contradiction diagram, data from the most recent Interagency Registry for Mechanically Assisted Circulatory Support (INTERMACS) report was analyzed [16]. By drawing out the relationships between the system components, we can identify positive components of the system that lead to negative effects as defined, in Triz, as “contradictions” (Figure 1). For example, INTERMACS data indicates that there were 9797 bleeding and thromboembolic related events in the first three months post-op [16]. In the contradiction

diagram, thromboembolic related events can be caused by a number of components of the implanted VAD system, which reinforces that it is a problematic issue that needs a better solution. And indeed, as mentioned previously, thromboembolism due to blood activation is a longstanding problem area for all MCS devices. Similarly, there were 7604 adverse events as a result of surgical complications (such as infection or pleural effusion) in the first three months post-op [16]. Based on this, the contradiction diagram also identified the implant as an area of potential interest, as the implant surgery can lead to a number of potential complications. For example, if after surgery, an infection necessitated a pump exchange (negative causation), although it would be a revision surgery (negative event), it would results in the removal of infected tissue and the implant of a new working device (positive event). For the scope of this dissertation, we aim to address the problems and complications associated with thromboembolism and aim to design a device that could potentially be implanted via a less or minimally invasive procedure.

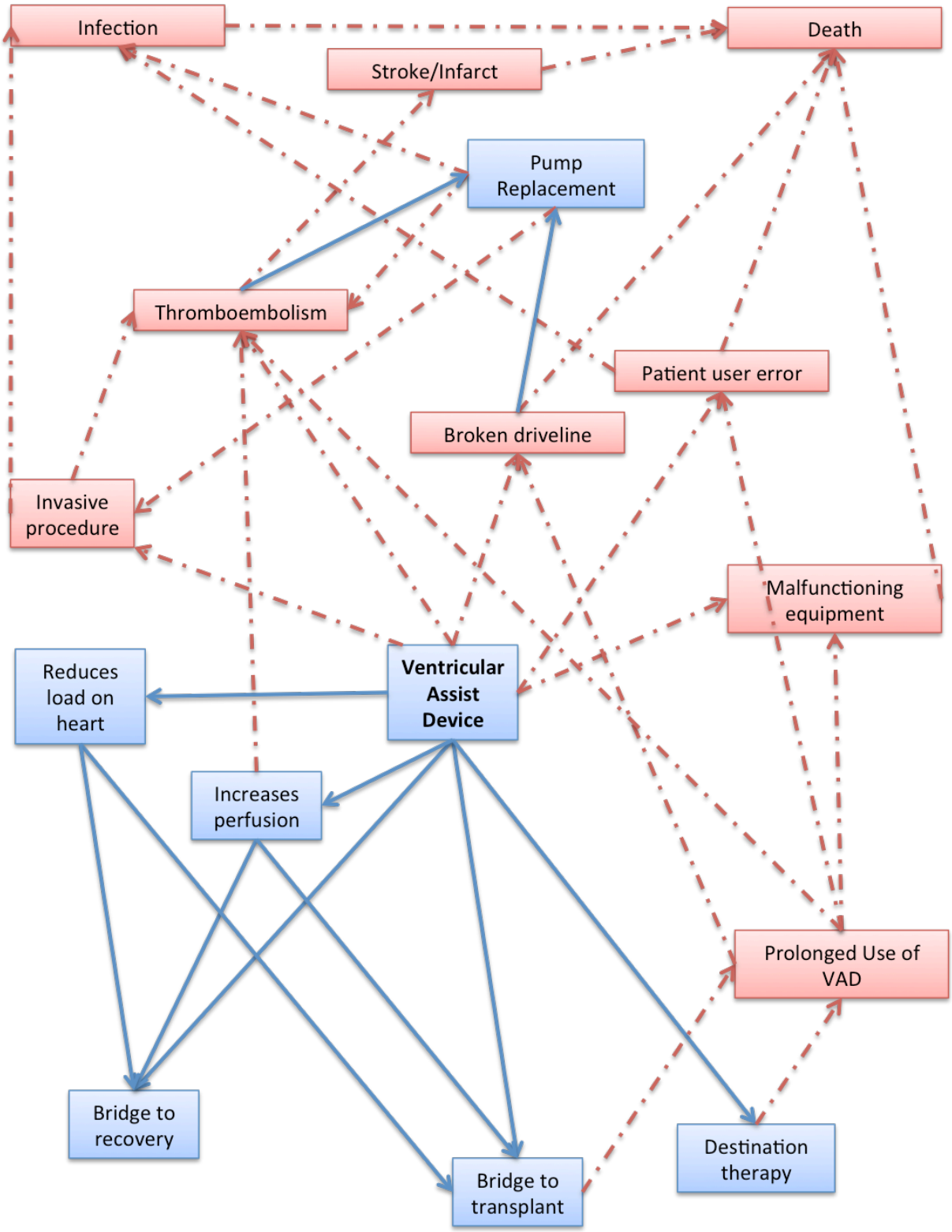

Figure 1: Contradiction diagram analysis for a VAD as a means for mechanical circulatory support. The blue and red boxes represent a positive and negative component/function, respectively. The solid blue and dotted red lines indicate positive and negative causes and effects, respectively.

1.2.2 Failure Modes and Effects Analysis of VADs

Based on the problem statement determined by the contradiction diagram analysis, it can be very helpful to conduct a failure modes and effects analysis (FMEA) of the device and its system as well [18]. Based on the level of potential harm for a component or function of the device, a Risk Index is assigned (Table 1) [19]. For the case of VADs for circulatory support in the context of thromboembolism and complications related to surgical implant, the following risk considerations, at minimum, should be considered for the design of a new device. The FMEA was evaluated based on risks associated with two clinically available VADs, Heartmate III (Abbott) and Heartware HVAD (Medtronic) [20,21]. Based on the FMEA, the unacceptable components and/or functions that have the most potential for serious patient injury or death have a common denominator, bleeding and thrombus formation, which is also supported by the INTERMACS data and contradiction diagram analysis. However, the main controls for the prevention or treatment of thrombus formation in VAD patients lie in the management of pharmacologic interventions and pump parameters for optimized hemodynamics. However, in reality, VAD patients' anticoagulation requirements are often dynamically changing and can be at odds with their required level of circulatory support. In summary, the findings of the contradiction diagram analysis and the FMEA analysis reinforce what is already well known – that the next generation of VADs should be designed such that the reliance on systemic anticoagulation is significantly minimized or completely eliminated.

Table 1: Hazard analysis "Risk Index" and their acceptance criteria [19]

Probability of Occurrence	Severity I - Catastrophic (Death, serious injury)	Severity II - Significant (Reversible serious injury)	Severity III - Marginal (Inconvenience)	Severity IV – (Negligible)
Frequent	1	3	7	13
Probable	2	5	9	16
Occasional	4	6	11	18
Remote	8	10	14	19
Improbable	12	15	17	20
Hazard Risk Index	1-5	6-9	10-16	17-20
Acceptance Criteria	Unacceptable	Undesirable, written and reviewed decision required to proceed	Acceptable with QA review	Acceptable without review

Table 2: A failure mode and effect analysis (FMEA) of LVAD implant and thromboembolic complications.
* *Desmopressin is a common medication for the treatment of blood clotting disorders* [22]
** *Most common affected organ systems are neural, pulmonary, renal, hepatic, and gastrointestinal* [23]

Function or Component	Failure Mode	Effect on System	Possible Hazards	Risk Index	User Detection Means	Applicable Controls
Bleeding	Patient injury, surgical complication, improper anticoagulation	Blood loss, swelling of affected area	Decreased perfusion, stroke, death	3	Visual, pain, swelling or inflammation in affected region	Proper management of anticoagulation and clotting factors,
Device Malfunction	Failure of any component of device	Device stops working, patient no longer supported, blood stagnation in pump, thrombosis of pump	Pump fails, decreased perfusion, dizziness, chest pain, sudden cardiac arrest, death	8	Visual and audible alarms for device faults, patient dizziness, chest pain	Alarms to alert patient, controller exchange, pump exchange
Device Thrombosis	Blood activation, hemolysis	Reduced pump efficiency, potential for clot to shear off and travel through circulatory system	Can lead to stroke, thromboembolism, device failure, etc.	6	Sudden or trended increase or decrease in device flow and power output	Proper systemic anticoagulation, decrease pump speeds to prevent hemolysis
Driveline Infection	Improper driveline dressing management, injury to driveline exit site	Local infection of driveline exit site	Potential for spread of infection, pump exchange, sepsis	6	Local inflammation, driveline site discharge	Sterile dressing regularly changed
Hemolysis	Red blood cell destruction due to mechanical trauma and high shear forces of pump rotors	Leads to thromboembolism, reduced perfusion	Blood clots, stroke, death	3	Sudden or trended increase or decrease in device flow and power output, labs	Proper systemic anticoagulation, decrease pump speeds to reduce hemolysis
Platelet Dysfunction	Increased systemic inflammation, high shear rate through pump head	Potential for platelet micro-aggregation or spontaneous bleeding	Blood clots, bleeding, stroke	5	Labs	Proper systemic anticoagulation, *desmopressin**
Stroke	Thromboembolism, uncontrolled bleeding	Reduced perfusion to affected area	Severe patient physical and cognitive impairment, death	4	Facial droop, arm weakness, dizziness, slurred speech	Proper systemic anticoagulation, decrease pump speeds to reduce hemolysis
Organ Damage During Driveline Tunneling	Trauma to tissues during surgical implant	Inflammation, scarring, potential for permanent organ damage	Failure of injured organs, could lead to multi-organ failure**	6	Pain, bleeding or inflammation in affected region	Surgical prevention by taking time and care
Peripheral Thromboembolism	Improper patient anticoagulation, blood activation, hemolysis	Reduced perfusion to affected area	Loss of function in affected area, potential amputation, death	4	Pain or inflammation in affected region	Proper systemic anticoagulation

1.3 Development of a Torsional Ventricular Assist Device

The goal of this work was to develop a mechanical means to support the failing heart over the long term while eliminating the risk of thromboembolic complications common to all cardiac assist devices currently on the market. ***Specifically, our aim is to address the longstanding problem of blood activation due to artificial blood-contacting surfaces by developing a torsion-based ventricular assist device (tVAD) that avoids blood contact altogether.*** This approach to cardiac support was originally inspired by the contractile mechanics of healthy human hearts, which produce a "wringing" motion during systole (Figure 2) that allows the ventricles to empty more completely and reduces transmural stresses acting on the heart walls [24]. During each cardiac cycle, the heart twists counter-clockwise at the ventricular apex and clockwise at the ventricular base, near the valves. This natural torsional component can be attributed to the muscle fiber orientation within the myocardium, which upon contraction produces a net ventricular twisting of about 10-15 degrees. This torsional motion reduces the wall stresses and further promotes the emptying of the ventricles during systole [24]. This characteristic twisting motion is frequently altered (or missing altogether) in diseased hearts, which is thought to result in accelerated disease progression, lowered cardiac efficiency and decreased global function. Therefore, it is reasonable to hypothesize that restoring this wringing motion to the beating heart may help return the heart to healthy hemodynamic function. Previous studies, done separately by Trumble et al., Criscione et al., and Roche et al. [25-27] have demonstrated through computational, in vitro, and in vivo experiments that this applied wringing motion has the potential to return cardiac hemodynamics towards a healthier state. To further test this hypothesis, this thesis presents a series of experimental methods and results with the end goal of optimizing the design parameters for a tVAD prototype.

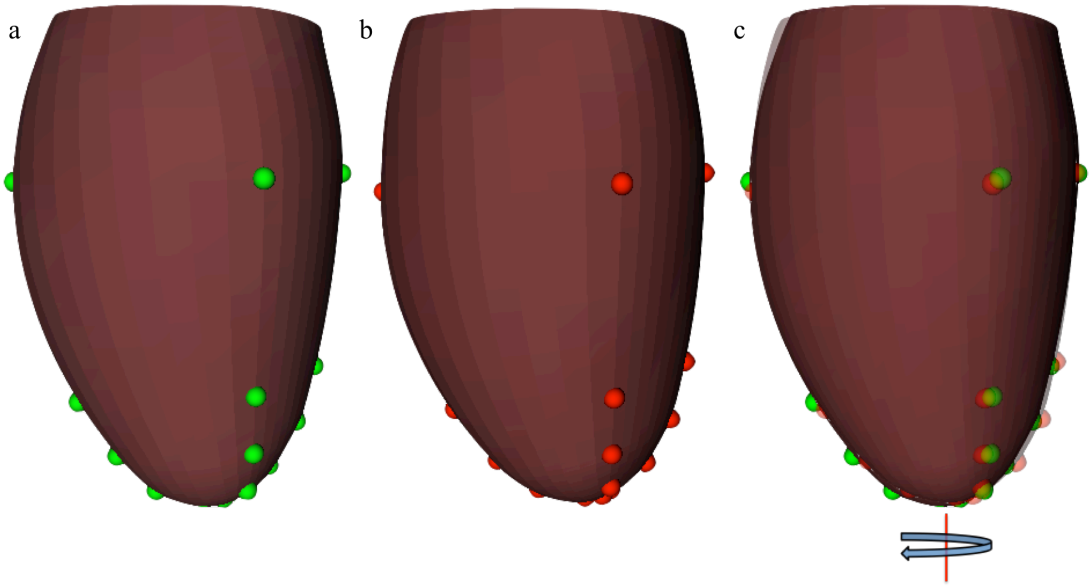

Figure 2: Renders of a computational model of the LV endocardium of a patient with end stage heart failure demonstrating its native twist - a) LV endocardium with element nodes at the start of the cardiac cycle, b) at peak systole, and c) superimposed image of LV endocardium at start of cardiac cycle and peak systole demonstrating the motion of left ventricular motion due to the myocardial fiber orientation

1.3.1 Research Aim 1: Parametric Computational Simulations

Specific aim #1 extends preliminary parametric computational simulations to include a wider range of parameters in order to finalize the initial design of a torsion-based ventricular assist device (tVAD) prototype. The results of these parametric computational simulations were evaluated for their effects on cardiovascular hemodynamics and regional cardiac biomechanics [25]. Specifically, I aimed to determine the effects of this torsional load on global cardiovascular hemodynamics in order to determine optimal device design parameters, and the effects on regional cardiac biomechanics to determine the working limitations of such applied torsion therapy. Beyond that, the goal was to understand how the AAT loads at the valvular plane may potentially affect the function of the heart valves, which can lead to damage to the heart valves or valvular regurgitation. Toward that end, the computational simulations extended the range of applied angles of rotation and coverage areas and examine other parameters (e.g., timing of

rotations with respect to the cardiac cycle) that might affect tVAD performance and effects on the myocardium. These studies were designed to determine the best combination of applied rotation angle and coverage area to be used in follow-on parametric studies examining the effects of rotation speed and timing on global ventricular function. Ultimately, findings from these computational parametric studies will be used as a whole to establish design specifications for a fully functional tVAD prototype suitable for in vivo testing. These analyses were also expanded to include quantification of myocardial stresses and strains to better understand the physical limitations of this approach. Beyond determining optimized device design parameters, an effort was also made to create additional pathologies of patient-specific heart failure models.

1.3.2 Research Aim 2: Development of tVAD Attachment

The goal of specific aim #2 was to develop a method for superficial attachment of the tVAD to the epicardium of the heart. One major challenge of the tVAD approach is that it requires a secure attachment between the device and the exterior surface of the heart. Both the epicardial and the pericardial surfaces where the device is intended to be implanted are notoriously slick and there are few known materials that interface and stick securely to such surfaces. Typical methods of attachment, such as adhesives, active suction, banding, and sutures are potential problematic due to weak adhesive interactions with the tissue or the physical damage that the method of securement can potentially inflict [28]. Thus, there is a need to develop a new method or combination of methods to be used in tandem to provide a stable, safe and effective method of securing the device upon implantation. This aim was intended to be exploratory in nature with the goal of generating ideas and investigating the feasibility of those ideas with the hopes of finding a suitable bioadhesive or some other mechanical means to secure the tVAD to the epicardium for short-term applications.

Chapter 2

Preliminary Computational Parametric Studies

Based on the work done previously in the Trumble lab, it was established that applied apical torsion could potentially improve global cardiovascular hemodynamics in an induced heart failure porcine model. In these studies, computational simulations of a simplified left ventricle were rotated and analyzed for resulting cardiovascular hemodynamics and biomechanics and subsequently validated with in vivo pig experiments with a first generation tVAD prototype [25].

In this first proof of concept work, an idealized, high-order, 18-element left ventricular prolate spheroidal model with both normal (54% EF) and reduced (31% EF) contractile function was subjected to varying degrees of AAT during the systolic portion of the cardiac cycle. In these simulations, the virtual torsion apparatus was designed to cover 22% of the distance from the apex to the base. Results from the reduced function model showed improvements in LV stroke volume and peak pressure generation of 9.9% and 11.7% respectively at rotation angles of 90 degrees. These results were found to be in agreement with values recorded in experiments using a porcine model of acute HF wherein LV stroke volume increased by 17.1% and peak pressures rose by 10.9% under similar support conditions [25]. These results showed increases in ventricular stroke work, a reduction in wall stresses, and demonstrated that applied apical

torsion indeed has the potential as a CHF therapy. Based on these proof of concept studies, it was demonstrated that AAT has the potential to provide adequate assist for an acutely failing heart. In order to better determine design parameters for a second-generation device, a series of parametric simulations that expands on the previous tVAD modeling work would be especially useful. This chapter presents parametric computational simulations completed on simplified prolate models of the left ventricle where device coverage area (CA) and applied rotation angles (ARA) were varied. Furthermore, the ability to create more physiologically relevant model geometries for parametric computational simulations was also demonstrated.

2.1 Parametric Simulations

All of the computational simulations for this and subsequent chapters of this dissertation were built upon the studies of Trumble et al. by using ContinuityPro 7.0 (Insilicomed, Inc.), an advanced finite element (FE) software package for solving multi-scale problems. At its heart, ContinuityPro 7.0 (CPro) is a partial differential equation (PDE) solver that implements FE methods applicable to non-linear mechanics, reaction-diffusion, and monodomain problems. In the context of a cardiac biomechanics problem, each cardiac model includes the four following spatial scales: the cardiomyocyte, myocardium, the ventricle at the organ level, and the systemic circulation. In such multi-scale problems, their network of biophysical and/or biochemical relationships are represented by a set of ordinary differential equations (ODEs), a constitutive that represents physical properties of the system that spatially connects these point-wise networks, a system of PDEs that represent the laws of conservation governing the anatomical physics of the system, and boundary conditions that specify the interaction of the whole system with other structures [29]. Specifically, for these simulations of the effects of applied torsion on the heart, ODEs represent the dynamic Markov models of myofilament activation and

interactions within the cardiac myocyte. The constitutive equations describe the three-dimensional anisotropic mechanical properties of the cardiac tissue with respect to the local coordinate system, while also describing how the myofilament interactions modify the tissue dynamically. Finally, the governing PDEs for force and momentum balance are solved for the models as they are subjected to the boundary conditions imposed by the tVAD and the lumped parameter model of the cardiovascular circulation.

2.1.1 Model Geometries

For all of the computational simulations presented in this dissertation (Chapters 2-5), the models were simulated in global prolate spheroidal coordinates (λ, μ, Θ), where θ is the axis upon which the model was rotated, λ is the axis up and down along the ventricular wall, and μ is the axis radiating from the origin out through the ventricular wall (Figure 3). The rectangular Cartesian coordinates (x, y, z) for any given point in space can be defined in terms of its prolate spheroidal coordinates (λ, μ, Θ) as follows:

$$(1)\ x = d \cosh\lambda \cos\mu$$

$$(2)\ y = d \sinh\lambda \sin\mu \cos\Theta$$

$$(3)\ z = d \sinh\lambda \sin\mu \sin\Theta$$

$$(4)\ d = a^2 - b^2$$

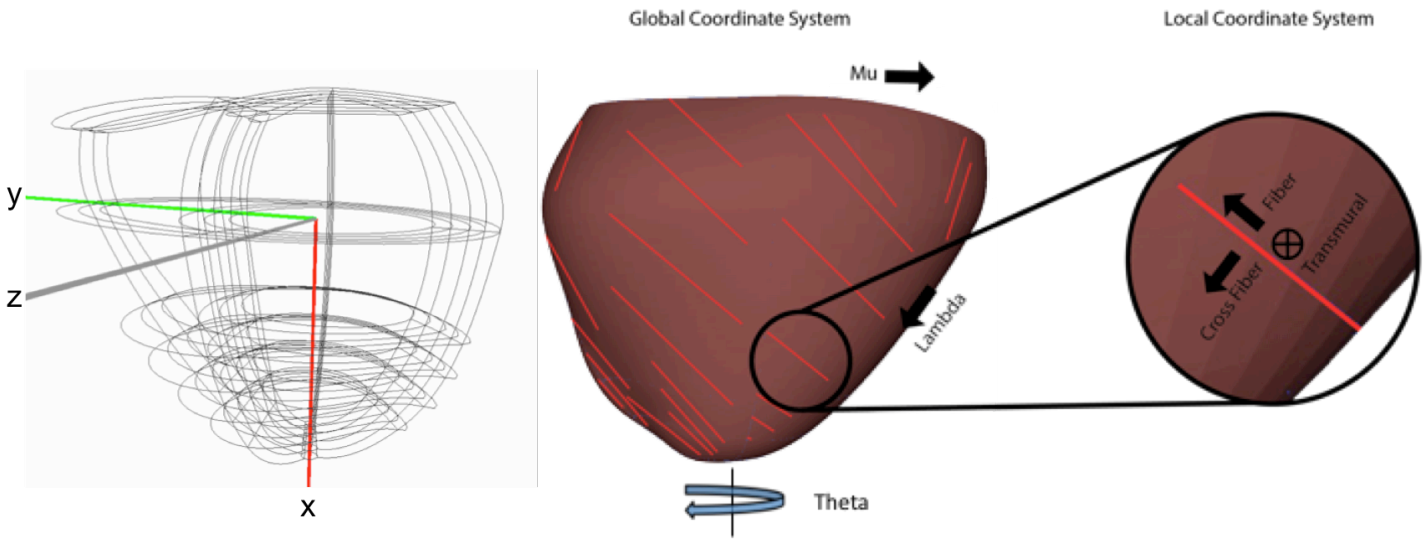

Figure 3: The Rectangular Cartesian global (left) and the prolate spheroidal global and local (right) coordinate systems

2.1.1.1 Porcine Prolate Heart Model

The first model was a simplified 15-element, high-order prolate model of the beating left ventricle based on measurements of swine hearts (Figure 4) and uses the model as described in the proof-of-concept applied torsion simulation [25]. The model was computed in global prolate spheroidal coordinates (Θ, λ, μ) with a focus of 4.35 cm, where the local coordinate system of fiber, cross-fiber and transmural are identical with that of the global. This set of simulations investigated how varying the parameter of effective CA of the device as it rotated the ventricle at 90 degrees would affect global hemodynamics, namely ejection fraction (EF) and stroke work (SW). To do this, the model was rotated around 3, 4, or 5 nodes located at the epicardium of the ventricle to represent low (30%), medium (40%), high coverage (50%), respectively, which would simulate varying sizes of a heart-device interface. The rotation was applied counterclockwise (view from the apex) during early systole and then rotated back.

2.1.1.2 Patient-Specific Prolate Heart Model

The second set of parametric applied torsion studies used an 18-element, high-order computational model of the beating left ventricle based on clinical measurements of a severe HF patient (Figure 5). The shape of the model was determined by averaging the thicknesses of the septal and free walls of the patient's left ventricle; this average wall thickness was then applied to the model, resulting in a more realistically shaped ventricular prolate. This patient-specific model had a focus of 4.96 cm and was also computed in global prolate spheroidal coordinates (Θ, λ, μ). This model was used to study the effects of varying the degree of applied apical torsion on global hemodynamics. To do this, the model was rotated around four nodes (medium coverage) at 0 degrees (NoVAD), 60 degrees, 75 degrees, and 90 degrees, and was applied during early systole and returned back.

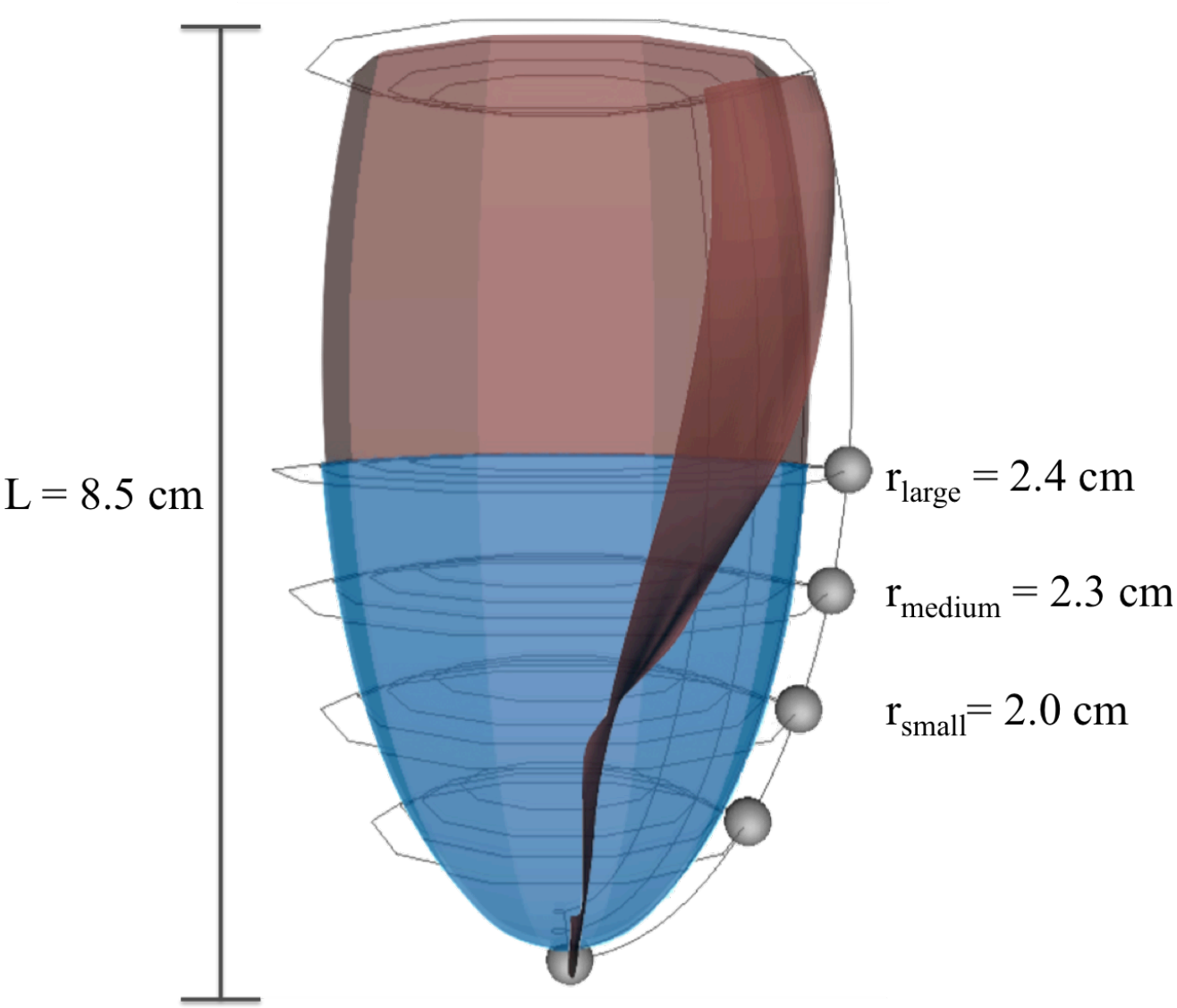

Figure 4: 15 element prolate model of a porcine left ventricle with a length of 8.5 cm from base to apex. The effecting device coverage area is highlighted in blue, where the varying levels of device coverage are determined by the epicardial nodes. The cross-section of the myocardium is rendered for visualization of the applied torsion at the smallest coverage area.

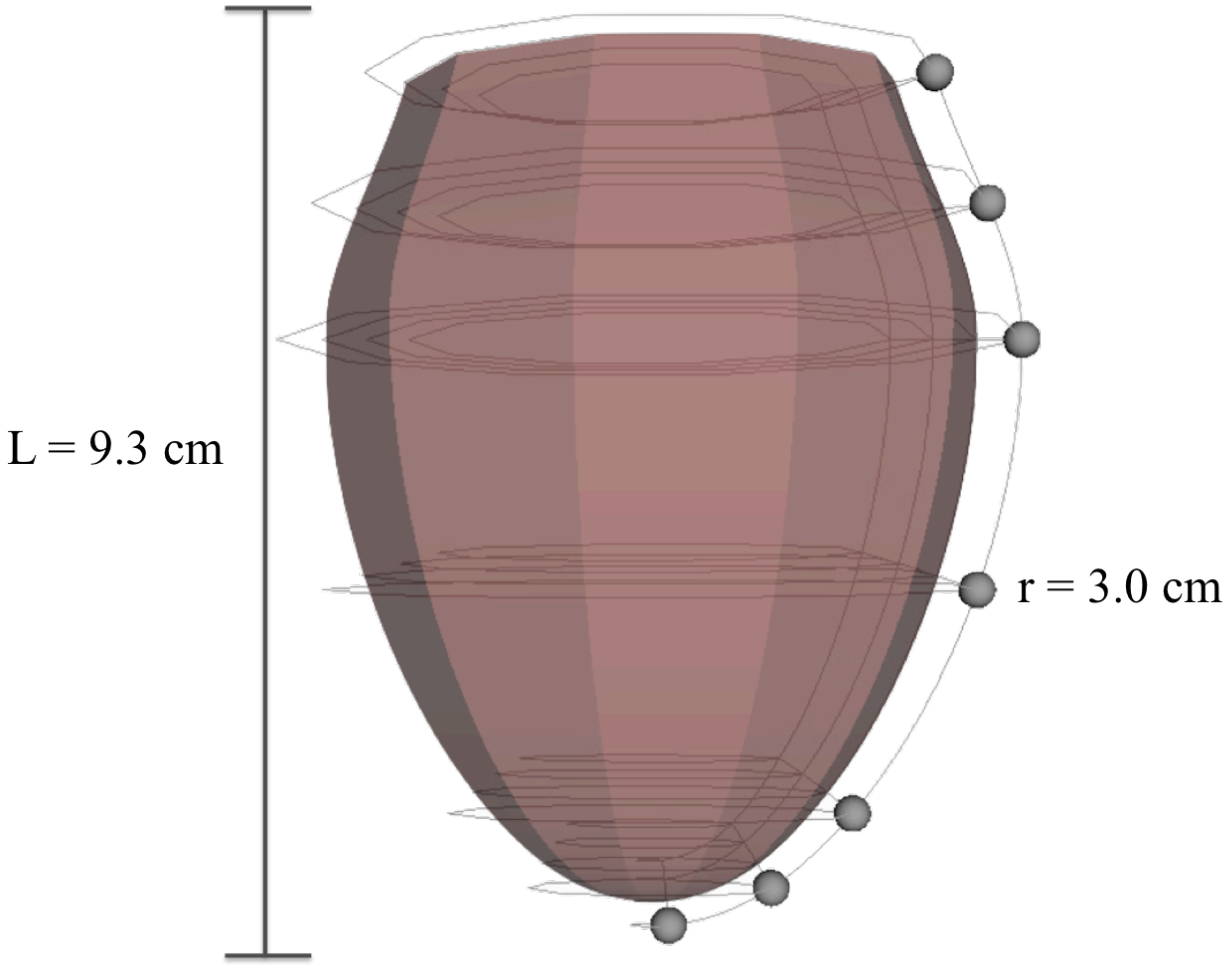

Figure 5: 18 element prolate model based on patient specific measurements with the cross-section of the myocardium is rendered for visualization of the applied torsion of 75 degrees.

2.1.2 Passive Properties of the Prolate Model

A nonlinear, transversely isotropic material law was used to simulate the passive properties of the ventricles, as described in Table 3. It is a modified version of the law described by Guccione et al. [30] that is defined in terms of a hyperelastic, exponential strain energy function as follows:

$$(5)\ W = \frac{C_{Scale}}{2}(e^{Q} - 1)$$

$$(6)\ Q = 2b_1(\overline{E_{RR}} + \overline{E_{FF}} + \overline{E_{CC}}) + b_2\overline{E_{FF}}^2 + b_3\left(\overline{E_{CC}}^2 + \overline{E_{RR}}^2 + \overline{E_{CR}}^2 + \overline{E_{RC}}^2\right) + b_4\left(\overline{E_{RF}}^2 + \overline{E_{FR}}^2 + \overline{E_{FC}}^2 + \overline{E_{CF}}^2\right)$$

Where the strain energy function W, is described by a stress scaling value (C_{Scale}), a quadratic function of the three principal strain components in the local fiber coordinate system (Q), and scaling coefficients to describe the material stiffness of the fiber, cross-fiber and transmural directions (b_1, b_2, b_3, b_4). Because this constitutive law allows for increases in the bulk modulus to ensure that determinant J remains close to unity, a slightly compressible version was developed that provides better convergence characteristics than an incompressible version using standard Lagrange multiplier/penalty function techniques. This version was improved further with a more advanced version of the compressible term [31], as defined by the following:

$$(7)\ W = W(b) = W(I_b, II_b, III_b) = W(\lambda_1, \lambda_2, \lambda_3)$$

$$(8)\ J = \sqrt{III_b} = \lambda_1\lambda_2\lambda_3\,, \quad 0 < J < \infty$$

where the Cauchy-Green strain tensor, W(b), is dependent on only the invariants I_b, II_b, III_b or the principal stretches $\lambda_1, \lambda_2, \lambda_3$. For typical heart simulations, this material law provides accurate results with a bulk modulus of 350, including normal and pathophysiologic function. However, for the current studies, it was necessary to raise the bulk modulus to 500 in order to

maintain isochoric elements (i.e. $\lambda_1\lambda_2\lambda_3 = 1$) throughout the cardiac cycles due to very large myocardial deformations induced by the applied rotations, particularly at the largest angles during systole.

Table 3: Parameters of nonlinear, transversely isotropic material law

Passive Constitutive Law	**Parameters**
Stress Scaling Coefficient (kPa) (C_{Scale})	0.80
Fiber Strain Coefficient (b_2)	18.50
Transverse Strain Coefficient (b_3)	3.58
Fiber-Transverse Shear Coefficient (b_1)	1.63
Bulk Modulus (b_4)	500.00

2.1.3 Cellular Model

In order to accurately determine the force generated by the beating heart, the force generated by myofiber contraction must be calculated through the computational model, but to do so individually can be very computational taxing. Instead, CPro utilizes constitutive cellular model developed by Hunter et al. where the force development associated with myofiber activation and crossbridge kinetics is approximated by combining an active time-dependent component with a static nonlinear component [32-33]. The cellular model used to simulate active state is a modified Hill-type model with length-dependent activation that was used in the previous research on single ventricle tVAD simulation [34]. The parameters used in these studies are listed in Table 4. These values reduce contractility and are used in conjunction with abnormal circulatory parameters to simulate baseline heart failure. The passive and dynamic properties listed here are constant throughout these studies.

Table 4: Parameters of Cellular Model used to Simulate Active State

Dynamic Cellular Model	Parameters
Unloaded Sarcomere Length (microns)	1.95
Active Stress Scaling Parameter (kPa)	0.95
Intracellular Calcium Concentration (micromole/l)	4.35
Maximum Isometric Tension (kPa) at Longest Sarcomere Length	82.5
Length-Dependent Calcium Sensitivity Constant (kPa)	1.80
Sarcomere Length at which Active Force is Zero (micron)	1.58
Maximum Peak Intracellular Calcium Concentration (micromole/ml)	4.35
Hill Coefficient in Calcium Sensitivity	2.00
Slope of Relation between Time-to-Peak Tension and Sarcomere Length (ms/micron)	52.49
Intercept of Relation between Time-to-Peak Tension and Sarcomere Length (ms)	55.26
Slope of Relation between Relaxation Duration and Sarcomere Length (ms/micron)	131.20
Intercept of Relation between Relaxation Duration and Sarcomere Length (ms)	-94.34
Twitch Duration Scaling Factor	1.4625
Cardiac Cycle Duration (ms)	750.00

2.1.4 Circulatory Model

For the following set of experiments, the model was attached to a simple closed loop for the LV (Figure 6), where initial condition parameters for the circulatory model were consistent with previous prolate experiments (Table 5) [25]. In these simulations, each segment of the circulatory system was defined by a resistance (R) and compliance (C) parameter. Given the change in pressure over the circulatory segment, the forward flow (Q) of blood is determined by the R in that particular circulatory segment. During this flow evaluation, so long as the forward flow of blood was positive, the valves were modeled as open. When the calculated flow value because negative, the valve was simulated as closed. The parameter of C was used to determine the pressure-volume loop relationship as described by the hydraulic equivalent of the capacitance law.

The left ventricle was modeled with a time-varying elastance model as described by Kerckhoffs et al. to simplify the initial condition calculations for the FE coupling [35], where the relationship is as follows:

$$(9)\ p_{LV} = E(t)(V_{LV} - V_{LV,rest})$$

where p is pressure, where V the volume through E(t), the time-varying elastance. Similarly, the left atrium was modeled by the following time-varying elastance relationship [35]:

$$(10)\ y_a = \begin{cases} -12\cos\left(\frac{2\pi t_{atrium}}{t_{twitch}}\right) + 0.5 & t_{atrium} < t_{twitch} \\ 0 & t_{atrium} > t_{twitch} \end{cases}$$

$$(11)\ P_{LA} = E_{LA} \times \left(V_{LA} - V_{LA,rest}\right)$$

$$(12)\ E_{LA} = (E_{LA,max} - E_{LA,min}) \times y_a + E_{LA,min}$$

$$(13)\ V_{LA,rest} = (1 - y_a)\left(V_{LA,rd} - V_{LA,rs}\right) + V_{LA,rs}$$

In order to couple the FE LV with the circulatory model at each time step, LV pressures are estimated and updated until convergence is achieved, as described by Bovendeerd et al. [36]. These pressures then were applied as the hemodynamic boundary conditions for the FE model and circulatory models such that if the difference between V_{circ} and V_{FE} were small enough, a time step was taken. If not, LV pressure perturbations were performed in the subsequent two updates to determine LV compliance ($\Delta V_{LV}/\Delta p_{LV}$ [ml/kPa]) from FE and circulatory models and the difference between V_{circ} and V_{FE} are then minimized over the course of the remaining updates using modified Newton iterations [35]. To prepare a starting point for the simulation, the model was first inflated to an end diastolic pressure, 1 kPa (or 7.5 mmHg). The simulation was run for four cardiac cycles, where each cycle was 750 msec long, with concurrent heartbeats until a hemodynamic steady-state solution was achieved, and the results of the last cardiac cycle

were collated and evaluated (Figure 7). For each simulation, time steps of 0.5 or 1.0 msec were selected to optimize computation time.

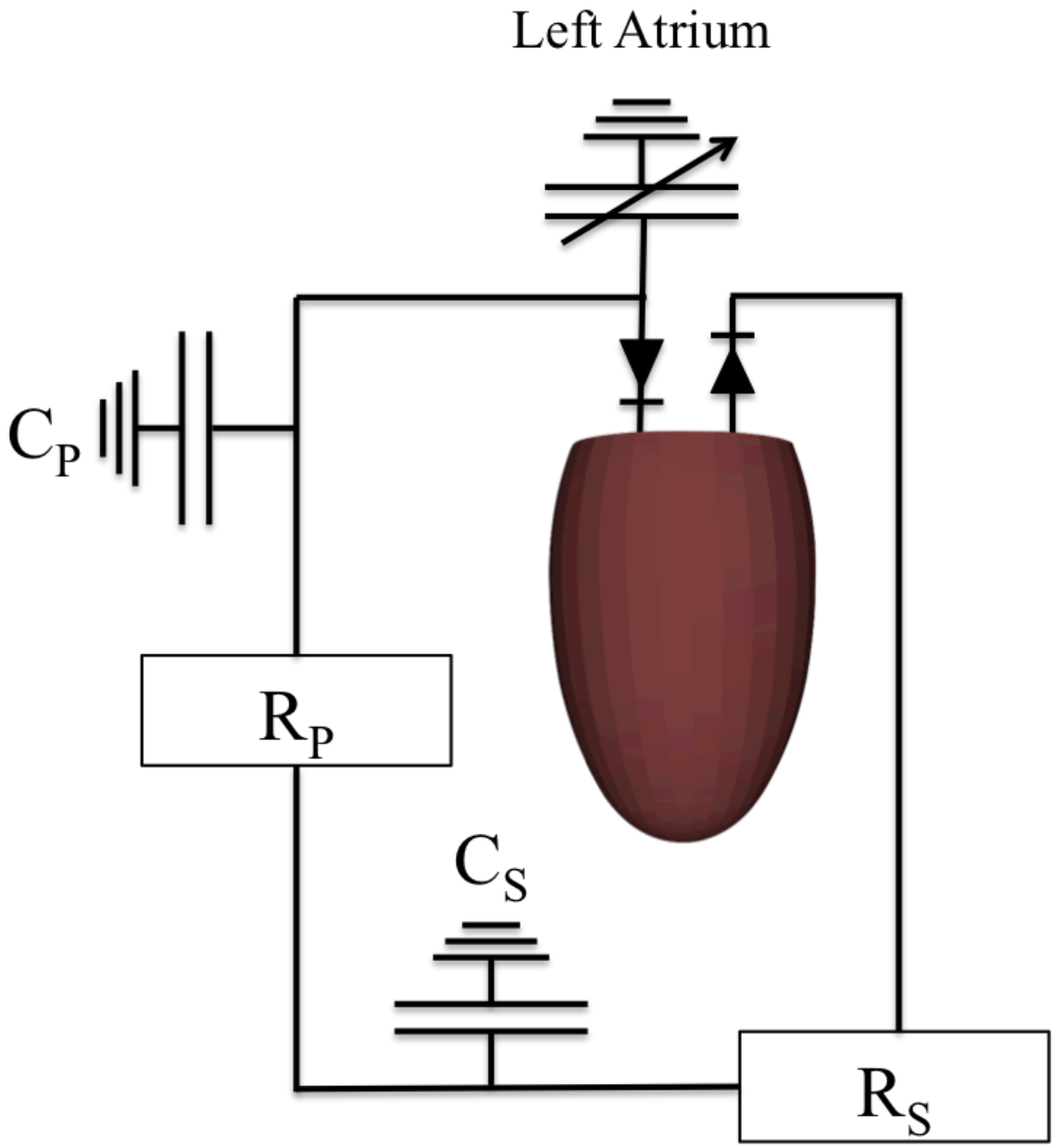

Figure 6: An electrical circuit analog of simple closed loop for LV only circulation model where C_s is the systemic vascular compliance [ml/mmHg], R_s is the system vascular resistance [mmHg · s/ml], C_p is the pulmonary vascular compliance [ml/mmHg], R_p is the pulmonary vascular resistance[mmHg · s/ml]

Table 5: Parameters and Initial Conditions of Circulatory Models

Closed Loop with Atria for LV: Systemic and Pulmonic Circulations	**Parameters**
Exponential Scaling Factor	6.76
Atrial Wall Volume (ml)	5.94
Pericardial Fluid Volume (ml)	10
Epicardial Volume Scaling Factor	1
Left Ventricular Pressure (kPa)	1
Volume of Pulmonary Circuit (ml)	49
Volume of Systemic Circuit (ml)	1020
Basic Cycle Length-Left (ms)	750.00
Arterial Impedance-Left (kPa-ms/ml)	7.00
Compliance of Pulmonary Circuit (ml/kPa)	4.3
Resistance of Pulmonary Circuit (kPa-ms/ml)	480
Compliance of Systemic Circuit (ml/kPa)	920
Resistance of Systemic Circuit (kPa-ms/ml)	4
Number of Pressure Estimations (settings)	10.00
Total Number of Time Steps (settings)	20000.00
Relative Volume Accuracy (settings)	0.0001
Duration of ventricular twitch (t_{twitch})	0.3
Start time of first active ventricular contraction (t_{active})	0.2

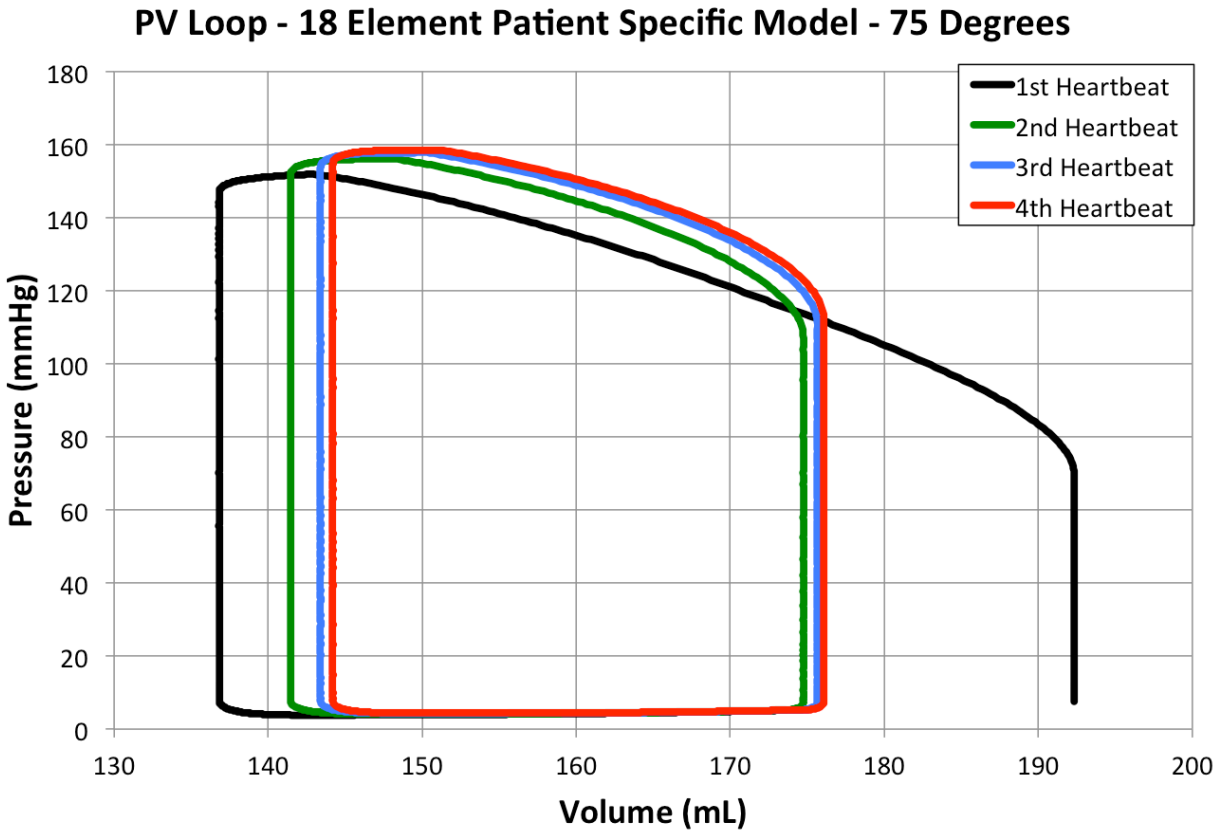

Figure 7: Resulting LV PV-loops for each cardiac cycle from the simulation where with each subsequent cycle, the system comes closer to reaching a steady-state solution.

2.2 Results

2.2.1 Porcine Prolate Heart Model

In the first model we investigated the effects of varying the coverage area of the tVAD on the ventricles. Results from this initial parametric study demonstrated that as we increased the coverage area of the device over the epicardium, there was an increase in both ejection fraction and stroke work, which was promising as we moved on to the next iteration of our model (Table 6). We also saw a proportional leftward shift in the resulting PV loops for the isovolumic relaxation segment, which demonstrated that the ventricle was emptying more completely during systole (Figure 8). These initial results were promising as it supported the notion that the applied torsion can effectively assist the emptying of the heart.

2.2.2 Patient-Specific Prolate Heart Model

In our subsequent parametric study, we investigated the effects of increasing the applied angle of rotation on the ventricle. We increased the complexity of the model by increasing the number of mesh elements, and by creating a more realistic ventricular wall shape by varying myocardial thickness along λ based on clinical measurements from a heart failure patient. Results from this study indicated that increases in the angle of apical torsion increased ejection fraction and stroke work (Table 7) and resulted in a greater leftward shift for the isovolumic relaxation portion of the PV loops (Figure 9). This mirrors the results from our previous study of effects of tVAD coverage area, demonstrating that with increasing amount of applied torsion angle on the heart, the tVAD can be expected to yield greater improvements in cardiovascular hemodynamics and biomechanics. Although the simulations were done in simplified prolate models, the results are encouraging as we move into our more complex and realistic biventricular model.

Table 6: Resulting hemodynamics for coverage area study on a 15-element pig prolate model

Device Coverage Area	Ejection Fraction (%)	Stroke Work (mmHg*mL)
30%	37.0	1469
40%	29.8	1700
50%	49.4	2543

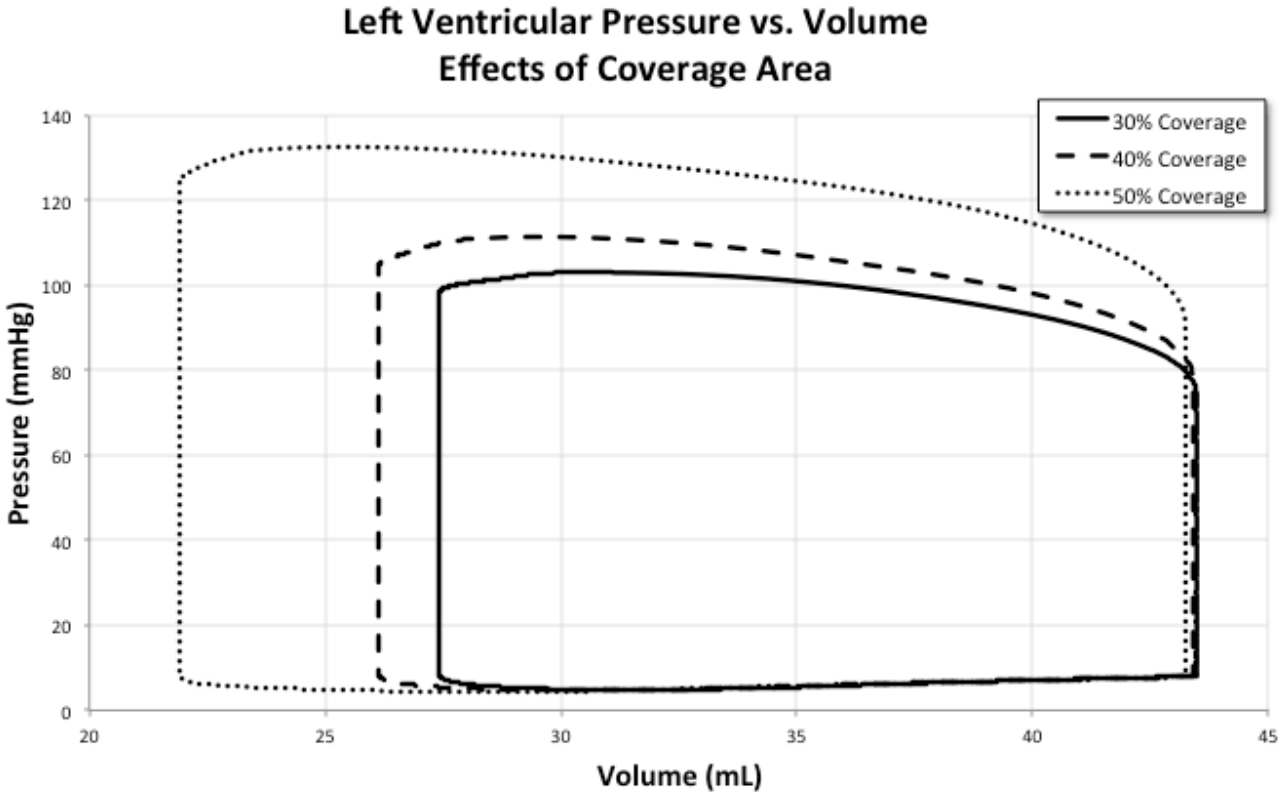

Figure 8: Resulting PV-loops for experiments investigating effects of increasing coverage area

Table 7: Resulting hemodynamics for applied rotation angle study on an 18 element patient-specific prolate model

Applied Rotation Angle	Ejection Fraction (%)	Stroke Work (mmHg*mL)
No VAD	14.8	3870
60 Degrees	15.6	5658
75 Degrees	18.1	6602
90 Degrees	22.3	7363

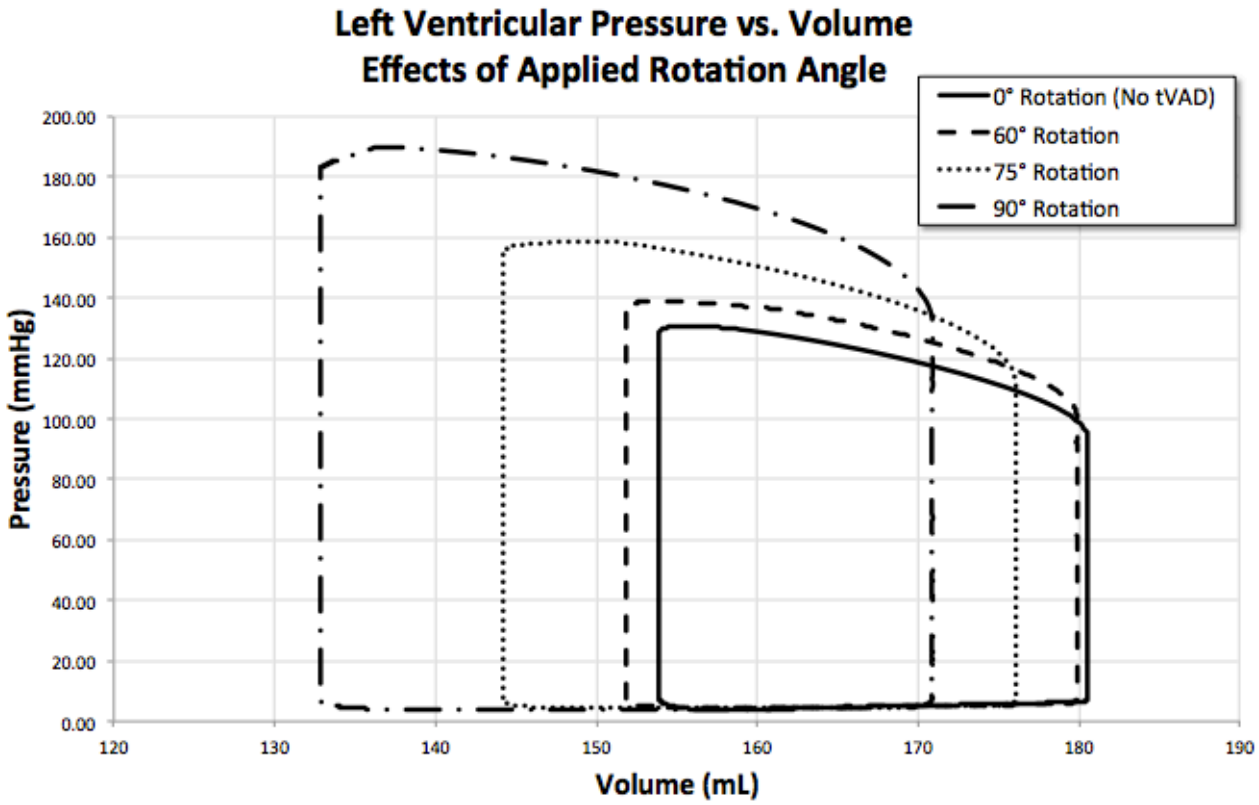

Figure 9: Resulting PV-loops for experiments on effects of various applied rotation angles.

2.3 Discussion

Since the initial experiments in 2011, the simulations of the prolate models were extended to include a series of parametric studies in order to understand how various parameters affect tVAD performance. In the first study, it was determined that increasing device coverage areas positively affect the resulting cardiac hemodynamics. In the subsequent study, we determined that increasing angles of applied apical rotation also substantially increased the resulting hemodynamics. Both of these finding supported the initial proof of concept experiments for the first generation tVAD. Beyond understanding the potential effects of different design parameters for the tVAD, it was demonstrated that the simulations can be scaled to a more complex and physiologically realistic geometry. These initial computational parametric studies were limited by their simplified model geometries of the left ventricle. However, the workflow established with these single ventricle computational simulations were used as the framework for subsequent computational studies in more complex studies on a patient specific bi-ventricular computational model.

Chapter 3

Parametric Study on Effects of tVAD Support on Cardiovascular Hemodynamics

Cardiac assist devices have come a long way since their introduction 50 years ago [27]. In that time, the number of blood pumps available to clinicians has been greatly expanded and systematically refined to meet the cardiac support needs of more HF patients than ever before. In this sense VAD therapy can be—and should be—considered an enormous success, especially to the thousands of patients who have directly benefitted from this life-saving technology. Still, despite the many technological triumphs that have marked the developmental history of the 'artificial heart,' longstanding problems of blood activation and driveline infections remain largely unresolved in the setting of long-term cardiac support. Consequently, most blood pumps today are used either to treat patients in cardiogenic shock (rescue) or as a bridge to cardiac transplantation rather than as permanent replacements for the human heart.

While driveline management has been a persistent problem for VAD patients over the years, the foremost impediment to long term cardiac support has been hematologic complications caused by two main factors: the inherent thrombogenic properties of synthetic blood contacting surfaces and the systemic bleeding complications associated with impeller-driven pumps. Because blood clots are a serious concern with any blood-contacting device—heart valves and

coronary stents included—systemic anticoagulation is required for all VADs currently approved for clinical use. Unfortunately, rotary blood pumps, which comprise the vast majority of devices on the market today, make the use of these 'blood thinners' especially problematic since shear-induced proteolysis of von Willebrand factor can lead to serious bleeding problems elsewhere in the body. Pulsatile VADs tend to be gentler on the blood and cause fewer bleeding problems, but this advantage is largely mitigated by their having much larger blood contacting surfaces to manage. Consequently, thrombotic and bleeding complications remain a major source of morbidity and mortality among VAD patients to this day [37]. For these reasons we believe that non-blood-contacting assist schemes like the apical torsion approach described here may be especially well suited for patients requiring chronic circulatory support.

In the previous chapter, a workflow for testing different tVAD device parameters was developed for a prolate LV model. Findings from these preliminary studies were encouraging, but not conclusive owing to the simplified and idealized nature of the heart models used and the limited number of torsion modes examined. This chapter reports the results from computational experiments wherein varying degrees of rotation and apical CAs were imposed on a more accurate and complete representation of the failing human heart. These studies were designed to determine the best combination of ARA and CA to be used in follow-on parametric studies examining the effects of rotation speed and timing on global ventricular function. Ultimately, findings from these computational parametric studies will be used to establish design specifications for a fully functional tVAD prototype suitable for in vivo testing.

3.1 Material and Methods

By building upon the existing workflow as described previously in Chapter 2, a more complex computational model was created. This model more accurately portrays the effects of

applied apical torsion on the heart by modeling both cardiac ventricles based on real-life anatomic measurements. In all studies, a high-order, biventricular model of the beating heart (Figure 10) was employed using Continuity Pro computational modeling software (Insilicomed, Inc., La Jolla, CA). The software, simulation techniques and workflows are based on the research of the Cardiac Mechanics Research Group in the Bioengineering Department at University of California, San Diego [29]. The heart model was selected from a cohort of 13 patient-specific computational models of HF in our database. Because of the wide variation of cardiac geometries of these dilated cardiomyopathy patients, a model was chosen in the mid-range of the enlarged hearts as representative for the purpose of determining device design parameters. Since these are follow-on studies to simplified single ventricle modeling, a biventricular model in the mid-range of dilated HF models was designed to be generic in nature.

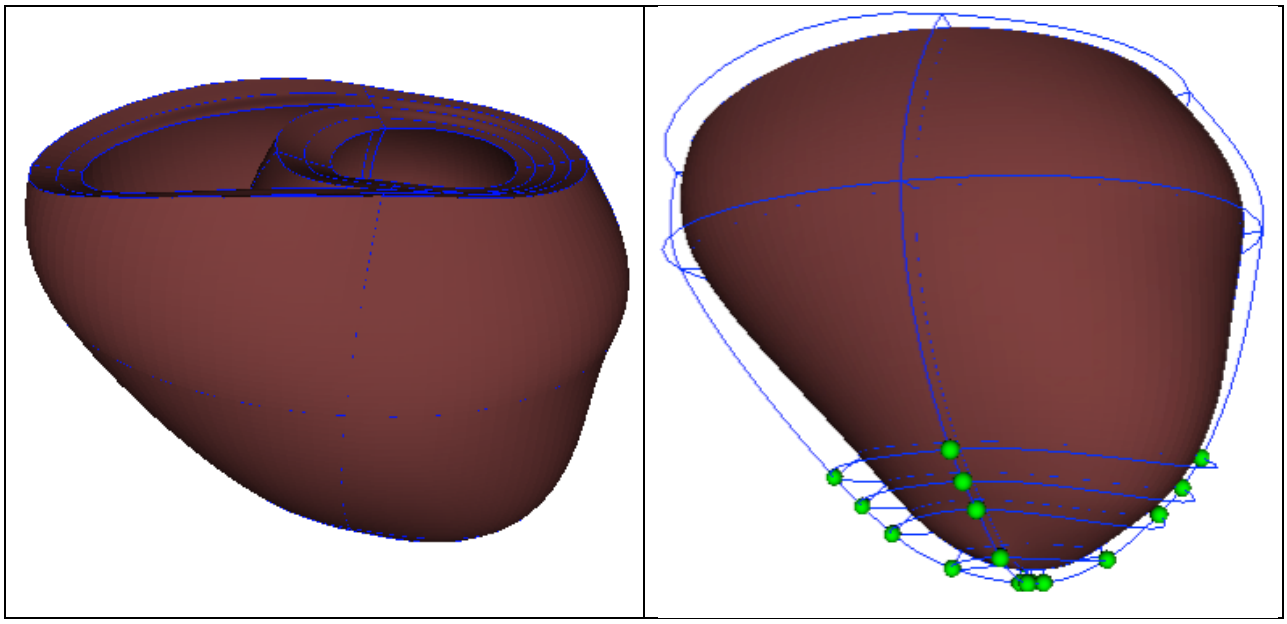

Figure 10: Biventricular heart failure model in the no load state; (left) model with epicardial and basal surfaces rendered; (right) model with endocardial surface of outer layer rendered along with all nodes that undergo applied rotation along with corresponding circumferences (posterior set of 5 nodes not visible).

The biventricular models in the database were developed using medical imaging and other clinical measurements obtained from patients with dyssynchronous HF, who were indicated for cardiac resynchronization therapy (CRT). Individual models were correlated with the available clinical data [38-39] to match the geometry, passive, nonlinear material properties, active state and circulatory properties of their respective patients. Details regarding general workflow and correlation methods have been discussed previously by Krishnamurthy et al. [39]. However, it was necessary to make modifications to the original baseline model to make it useful for the parametric studies described here. 3 of the 13 patients in the database had left bundle branch block (LBBB) and typical baseline EFs averaging about 27-28% [40]. However, patients indicated for ventricular assist are likely to have even lower EFs and may not be dyssynchronous in more than half of the cases [41]. Therefore, a number of additional modifications to the original baseline model were made. In brief, a baseline EF of about 20% was selected, and the baseline model was modified to achieve it. An extensive review of the literature on circulatory properties was performed to understand the range of circulatory impedance, resistance and compliance associated with HF in the systemic and pulmonic circulations [30, 38, 42-55].

Moreover, a variation in activation times was not included. The direction and locations of myofibers varied throughout the ventricles and were determined by the methods outlined by Krishnamurthy et al. and Villongco et al. where first, DT-MRI scans of a cadaver heart were obtained [39-40]. The diffusion tensors of the image were then fitted as a field of log-transformed components in a corresponding anatomical mesh and the fiber orientations in the resulting model were mapped to individual patients through large-deformation diffeomorophic mapping, as described by Cao et al., and reoriented by on the deformation gradients between the template and target patient anatomical geometries as described by Alexander et al. [56-57]. The

main correlation with clinical data for this patient involved the dilated geometry of the heart, which was fitted using B-mode echocardiographic views. In the CRT studies, baseline biventricular models were fitted to the echo views in prolate spheroidal coordinates. Then, they were transformed to rectangular Cartesian coordinates. However, the shape and dimensions of a given model remain independent of the coordinate system due to the tri-cubic, Hermite interpolation scheme. The dimensions of the model in the no load state are 12.1 cm from the epicardium of one free wall to that of the opposite free wall at the equator, 9.3 cm orthogonal to the first dimension, 8.1 cm from the left free wall epicardium to the RV septum (endocardium) and 9.3 cm in the longitudinal direction from base to apex (Figure 11). Selected left- and right-ventricular cavity volumes are provided in Tables 8 and 9. Cavity volumes for the large coverage case undergoing applied rotations at 65, 68.33, 71.67 and 75 degrees are shown. Pressure-volume loops for all cases are given in the results section

Table 8: Cavity Volumes as a function of applied rotation angle in the LV

Cavity Volumes in Selected Angles-LV				
State Angles	**65.00^o**	**68.33^o**	**71.67^o**	**75.00^o**
No load (ml)	134.8	134.8	134.8	134.8
End-diastole-large coverage (ml)	221.1	215.3	209.0	207.8
Peak pressure-large coverage (ml)	194.1	185.0	179.4	176.3
End-systole-large coverage (ml)	162.6	155.7	147.6	144.8

Table 9: Cavity Volumes as a function of applied rotation angle in the RV

Cavity Volumes in Selected Angles-RV				
State	**65.00^o**	**68.33^o**	**71.67^o**	**75.00^o**
No load (ml)	70.4	70.4	70.4	70.4
End-diastole-large coverage (ml)	104.6	97.5	90.2	86.3
Peak pressure-large coverage (ml)	72.7	64.9	59.0	55.2
End-systole-large coverage (ml)	49.1	40.2	31.0	26.6

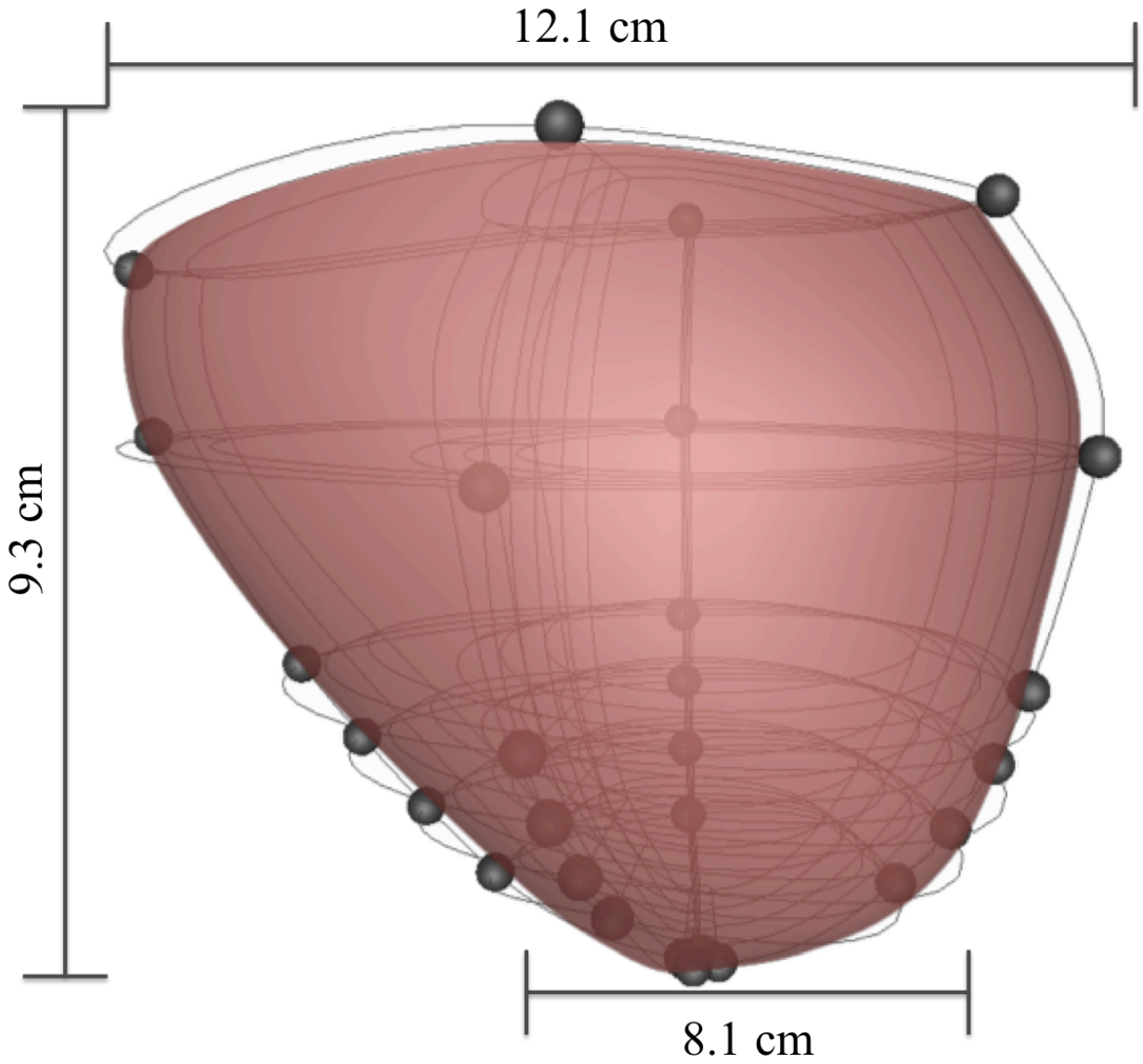

Figure 11: Dimensions of biventricular model, where the length of the ventricle from base to apex is 9.3 cm, width of the ventricle is 12.1 cm, and the endocardium of the left ventricle measures 8.1 cm wide

3.1.1 Boundary Conditions

In order to simulate the tVAD, the biventricular model was fixed at the epicardial nodes of the ventricular apex relative to one another (Figure 12). This allowed for the manipulation of the apical nodes to simulate different levels of device coverage area, where 20 nodes are rotated for the large coverage runs; 16 nodes are rotated for the intermediate coverage runs, i.e., the most basal set of nodes shown on the upper circumference of the coverage region is excluded; 12 nodes are rotated for the small coverage runs, i.e., the two most basal sets of nodes are excluded. The model was also fixed at the ventricular base as described in the following and allowed to freely deform. The two epicardial nodes of the basal ventricular free wall were fixed in λ, all basal ventricular nodes were fixed in μ, and the four epicardial nodes of the basal ventricle were fixed in θ.

3.1.2 Passive Properties of Model

This model uses the same nonlinear, transversely isotropic material law from Chapter 2 to simulate the passive properties of the ventricles, which can be found in Table 3.

3.1.3 Dynamic Properties: Cellular Modeling

The cellular model is the same Hill-type model with length dependent activation as presented in Chapter 2 for those previous studies (Table 4).

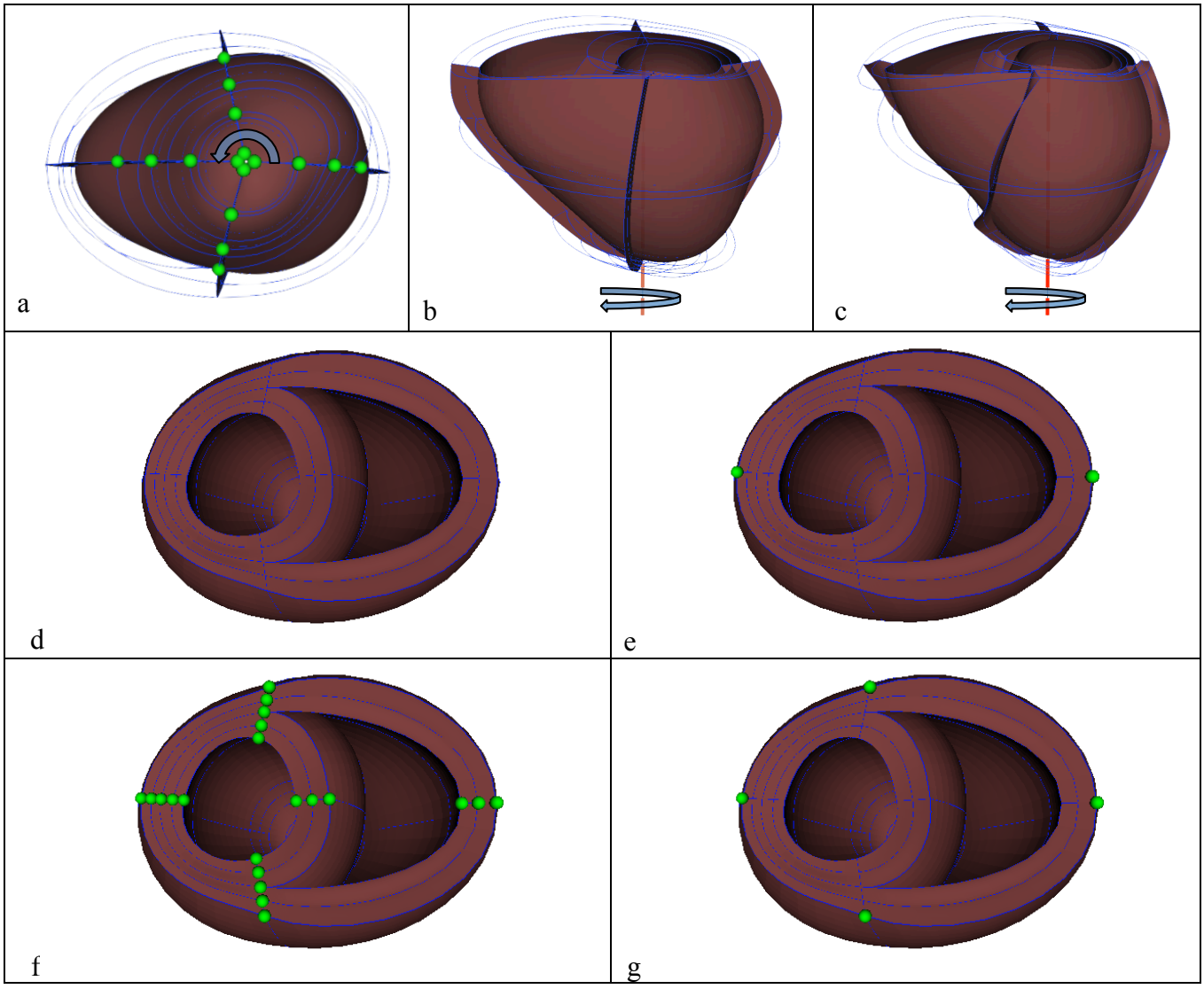

Figure 12: Fixed boundary conditions of the biventricular heart model; a) epicardial nodes at the ventricular base that allow for the simulated tVAD rotation, b) model before and c) after applied rotation; d) base of the model, e) two epicardial nodes fixed in λ, f) all basal nodes fixed in μ, g) four epicardial nodes fixed in θ.

3.1.4 Circulatory Properties

Based on the work of Kerckhoffs et al., the dual circulatory models with atria in which stable closed-loop systems for the LV and RV were used for this set of simulations [35]. The initial conditions and parameters of the pulmonic and systemic circulatory systems are shown in Table 10. The parameters were based on an extensive review of the heart failure literature and reflected expected increases in arterial impedances and resistances and decreased arterial compliances [25, 30, 38, 42-49, 51-52, 58-60]. Final adjustment of these parameters in test runs yielded an LVEF of about 20% in the pretreatment state.

In addition to the previous time-varying elastance models for the LV and LA presented in chapter 2, this dual ventricle circulatory model also uses the same time-varying elastance models for the RV and LA, where their relationships to pressure are as follows:

$$(14)\ p_{RV} = E(t)\left(V_{RV} - V_{RV,rest}\right)$$

$$(15)\ P_{RA} = E_{RA}\times\left(V_{RA} - V_{RA,rest}\right)$$

$$(16)\ E_{RA} = (E_{RA,max} - E_{RA,min})\times y_a + E_{RA,min}$$

$$(17)\ V_{RA,rest} = (1 - y_a)\left(V_{RA,rd} - V_{RA,rs}\right) + V_{RA,rs}$$

Furthermore, coupling of the FE model to the circulation was updated to include the RV, such that if the difference between V_{circ} and V_{FE} were small enough, a time step was still taken. If not, LV and RV pressure perturbations were performed in the subsequent two updates to determine LV compliance ($\Delta V_{LV}/\Delta p_{LV}$ [ml/kPa]), RV compliance ($\Delta V_{RV}/\Delta p_{RV}$ [ml/kPa]), and co-compliances ($\Delta V_{LV}/\Delta p_{RV}$, $\Delta V_{RV}/\Delta p_{LV}$ [ml/kPa]) from FE and circulatory models. Then as before, the difference between V_{circ} and V_{FE} are then minimized over the course of the remaining updates using modified Newton iterations [35].

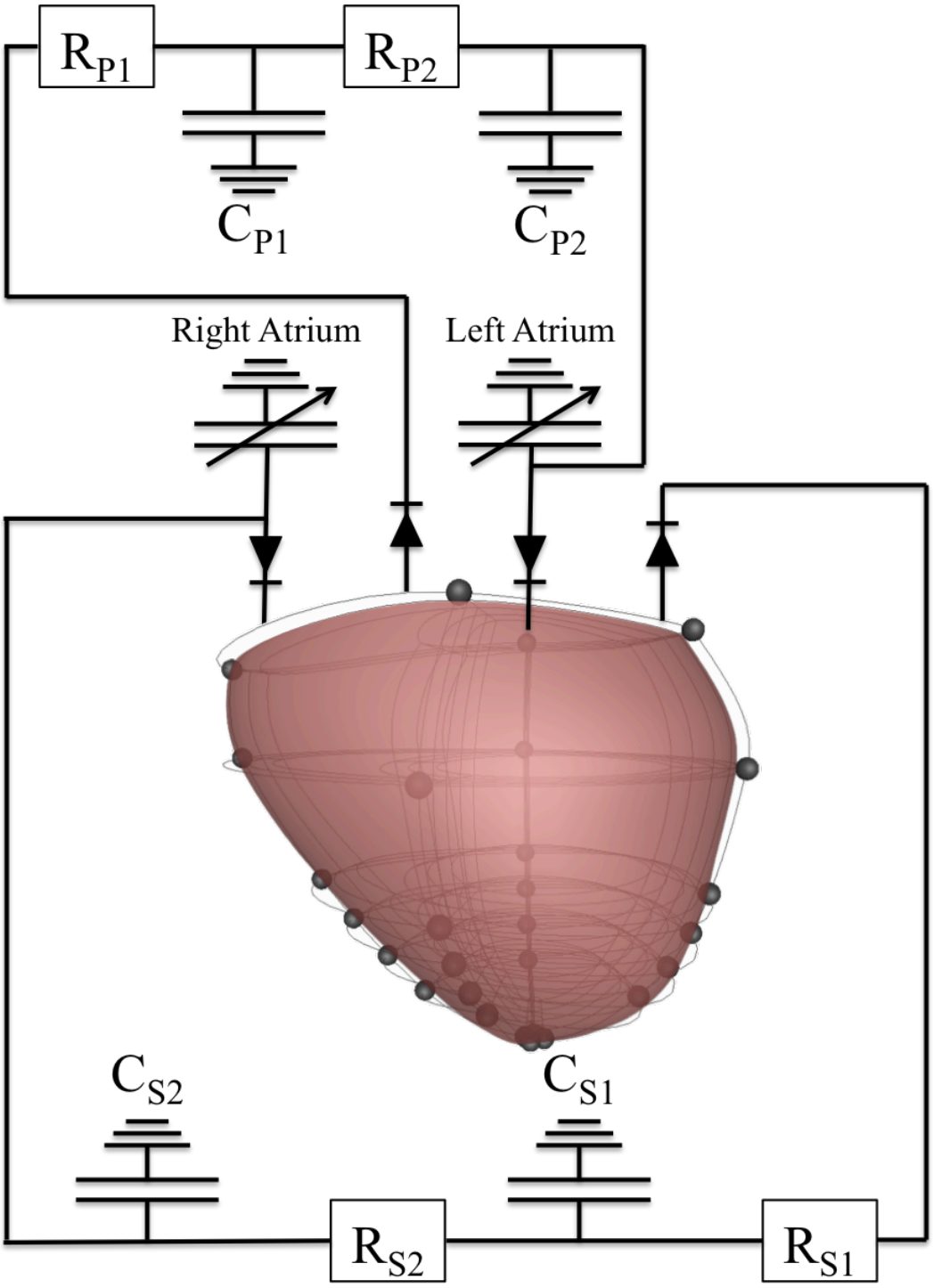

Figure 13: An electrical circuit analog of simple closed loop for LV only circulation model where C_{s1} is the systemic arterial compliance [ml/mmHg], R_{s1} is the systemic arterial resistance [mmHg · s/ml], C_{s2} is the systemic venous compliance [ml/mmHg], R_{s2} is the systemic venous resistance [mmHg · s/ml], C_{p1} is the pulmonary arterial compliance [ml/mmHg], R_{p1} is the pulmonary arterial resistance[mmHg · s/ml], C_{p2} is the pulmonary venous compliance [ml/mmHg], and R_{p2} is the pulmonary venous resistance[mmHg · s/ml]

Table 10: Parameters and Initial Conditions of Circulatory Models

Closed Loop with Atria for LV and RV: Systemic and Pulmonic Circulations	**Parameters**
Left Ventricular Pressure-Initial Condition (kPa)	1.50
Right Ventricular Pressure-Initial Condition (kPa)	1.00
Volume of Left Atrium-Initial Condition (ml)	37.33
Volume of Systemic Arterial Circuit (ml)	440.00
Volume of Systemic Venous Circuit (ml)	1800.00
Volume of Right Atrium (ml)	35.00
Volume of Pulmonic Arterial Circuit (ml)	225.00
Volume of Pulmonic Venous Circuit (ml)	120.00
Right Atrium Maximum Elastance (kPa/ml)	0.03
Right Atrium Minimum Elastance (kPa/ml)	0.0273
Right Atrium Unloaded Diastolic Volume (ml)	14.00
Right Atrium Unloaded Systolic Volume (ml)	13.00
Tricuspid Valve Resistance (kPa-ms/ml)	0.50
Arterial Impedance (right) (kPa-ms/ml)	4.00
Compliance of Pulmonic Arterial Circuit (ml/kPa)	60.00
Resistance of Pulmonic Arterial Circuit (kPa-ms/ml)	21.00
Compliance of Pulmonic Venous Circuit (ml/kPa)	65.00
Resistance of Pulmonic Venous Circuit (kPa-ms/ml)	4.00
Basic Cycle Length-Left (ms)	750.00
Time of Atrial Activation-Left (ms)	100.00
Atrial Twitch Duration-Left (ms)	375.00
Left Atrium Maximum Elastance (kPa/ml)	0.7823
Left Atrium Minimum Elastance (kPa/ml)	0.0711
Left Atrium Unloaded Diastolic Volume (ml)	14.00
Left Atrium Unloaded Systolic Volume (ml)	13.00
Mitral Valve Resistance (kPa-ms/ml)	0.50
Arterial Impedance-Left (kPa-ms/ml)	7.00
Compliance of Systemic Arterial Circuit (ml/kPa)	32.60
Resistance of Systemic Arterial Circuit (kPa-ms/ml)	126.00
Compliance of Systemic Venous Circuit (ml/kPa)	433.00
Resistance of Systemic Venous Circuit (kPa-ms/ml)	51.40
Number of Pressure Estimations (settings)	10.00
Total Number of Time Steps (settings)	20000.00
Relative Volume Accuracy (settings)	0.0001

3.1.5 Parametric Simulations

In these studies, the original prolate coordinates are kept due to the ease with which moving boundary problems can be performed utilizing the theta coordinates of rotated nodes alone in this coordinate system (λ, μ, θ). Node rotations are handled using a Python script that interacts with the boundary conditions embedded in the computational model to perform the moving boundary problem concurrently with inherent cardiac function (Appendix A.1). In these studies, as in the simplified analysis performed previously, a sinusoidal upswing is applied to create the rotation during isovolumic contraction and most of ejection. Then, a slow, linear return rotation is applied for the remainder of the cardiac cycle, as detailed subsequently.

3.1.6 Stroke Work Calculations

To calculate SW, Image J (U.S. National Institutes of Health, Bethesda, Maryland, USA) was used to measure the area circumscribed by the PV-loop of that cardiac cycle. It is important to calibrate the results to obtain SW in units of mmHg-ml. Accurate calibrations are performed using the largest rectangle available on the plot (Appendix A.2).

3.2 Results

Here, results obtained by varying both the ARA and device CA in simulated beating hearts are used to quantify their potential effects on global cardiac hemodynamics. Based on these simulations we found that the more aggressive rotations and higher CAs resulted in significant positive changes in key functional parameters, which suggest that torsion therapy may be a viable means to support the failing heart (Tables 11-12).

Table 11: Resulting left ventricular hemodynamics from rotation studies for the baseline heart failure case (No VAD), 12.5%, 18.2%, 24% device coverage areas.

	Angle (°)	*EF (%)*	*PSP (mmHg)*	*ESV (mL)*	*SW (mmHg*mL)*
No VAD		20.33	122.60	200.30	5321
12.5% Coverage	***0°***	20.67	124.19	197.68	5503
	45°	21.37	124.39	191.12	5624
	55°	21.86	124.73	186.04	5800
	65°	22.57	126.71	180.14	6010
	75°	23.67	130.81	172.69	6236
18.2% Coverage	***0°***	20.70	124.34	197.70	5615
	45°	21.61	124.63	188.52	5844
	55°	22.31	127.36	183.02	5913
	65°	23.18	130.02	176.41	6124
	75°	24.53	136.74	169.04	6805
24% Coverage	***0°***	20.73	124.40	197.30	5495
	45°	22.29	125.79	180.99	5694
	55°	23.89	133.01	173.51	6283
	65°	26.43	146.56	162.65	7456
	68°	27.68	152.46	155.72	7935
	72°	29.39	158.86	147.58	8599
	75°	30.35	164.00	144.77	9145

Table 12: Resulting right ventricular hemodynamics from rotation studies for the baseline heart failure case (No VAD), 12.5%, 18.2%, 24% device coverage areas.

	Angle (°)	*EF (%)*	*PSP (mmHg)*	*ESV (mL)*	*SW (mmHg*mL)*
No VAD		43.91	44.32	63.50	1793
12.5% Coverage	***0°***	44.91	43.60	60.82	1765
	45°	42.53	43.71	66.93	1744
	55°	42.12	43.95	68.71	1745
	65°	41.82	44.49	70.35	1794
	75°	42.69	45.10	69.38	1864
18.2% Coverage	***0°***	44.99	43.65	60.74	1781
	45°	41.86	43.86	68.94	1762
	55°	41.58	44.48	70.47	1786
	65°	42.22	45.26	69.92	1878
	75°	45.09	46.17	64.27	2007
24% Coverage	***0°***	44.94	43.59	60.86	1757
	45°	42.45	44.32	68.97	1745
	55°	45.12	46.02	63.81	1900
	65°	53.09	49.14	49.07	2193
	68°	58.78	51.02	40.21	2357
	72°	65.60	53.24	31.02	2561
	75°	69.18	54.56	26.62	2673

3.2.1 Varying Applied Apical Torsion

Overall, changes in rotation angle proved to be the more dominant factor in determining the effectiveness of this approach. Specifically, as the angle of apical rotation was increased beyond 45 degrees in the computer model, clinically significant changes were observed in ventricular EF, peak systolic pressure (PSP), end systolic volume (ESV) and SW when compared to the baseline HF model. EF improved proportionally with torsion applied in the 45 to 75 degree range, suggesting that CO can be augmented to a significant degree with torsion therapy (Figure 14).

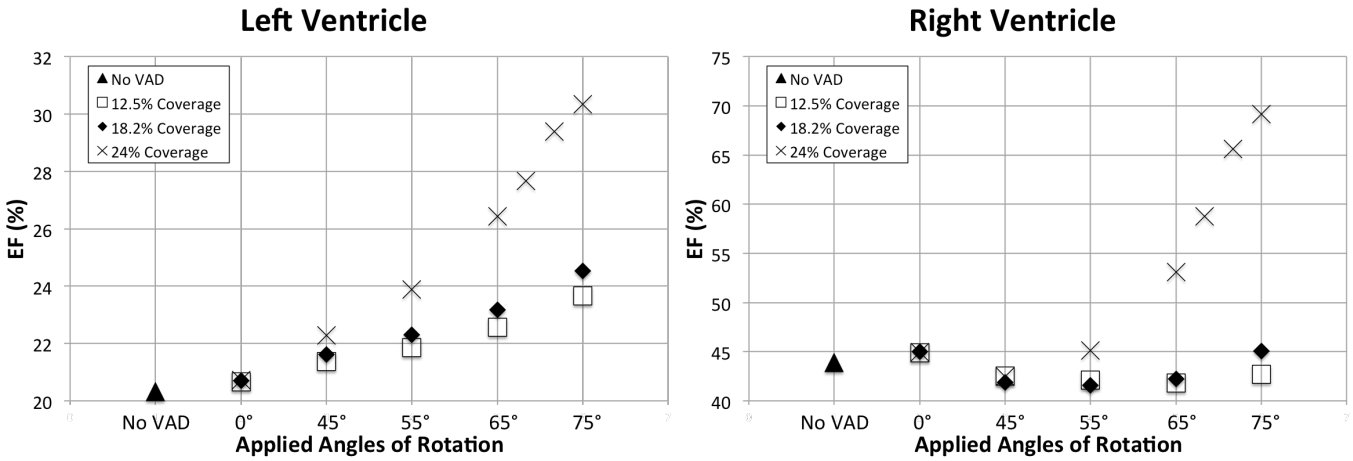

Figure 14: EF as a function of the applied angle of rotation and tVAD coverage in both left and right ventricles.

PSP also increased proportionally with torsion angle demonstrating that the rotation applied by the tVAD is helping the heart to empty more completely by mechanically displacing more blood (Figure 15).

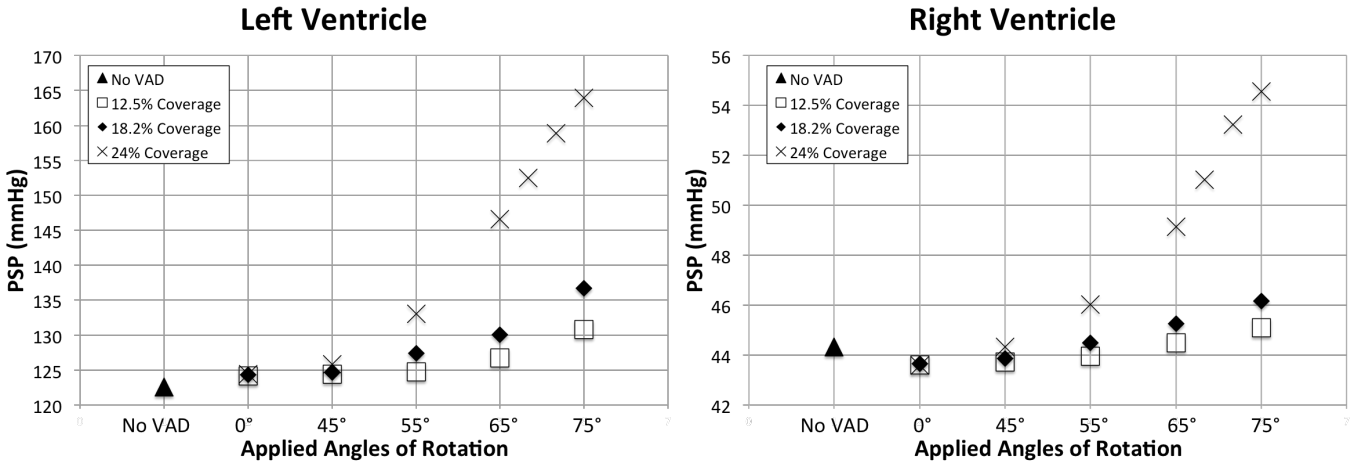

Figure 15: PSP as a function of the applied angle of rotation and tVAD coverage in both left and right ventricles.

Likewise, SW was found to increase dramatically with AAT, demonstrating that tVAD assisted ventricles are able to eject larger volumes of blood under higher afterload pressures (Figure 16).

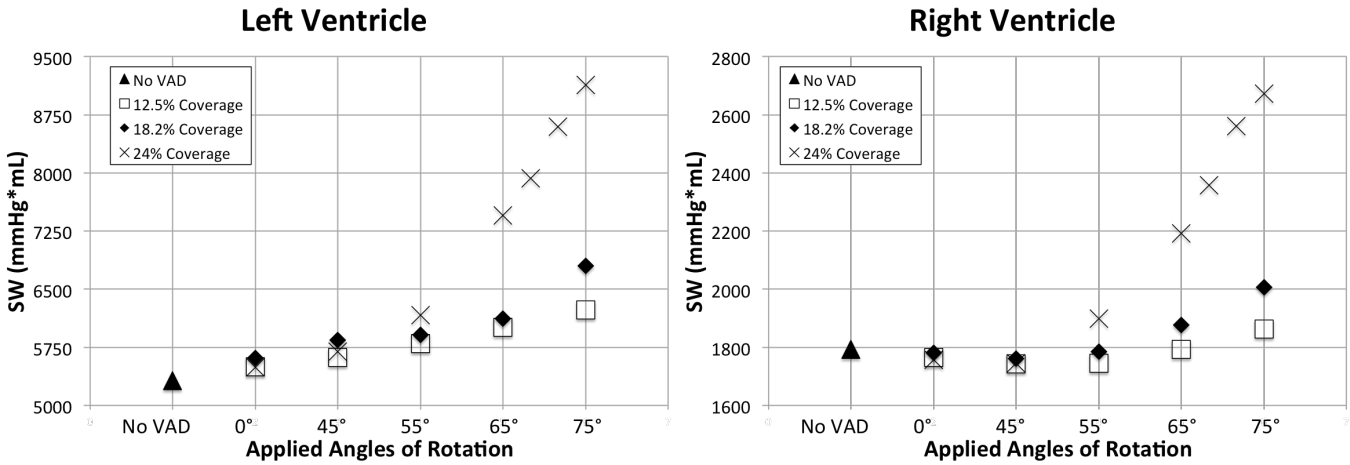

Figure 16: SW as a function of the applied angle of rotation and tVAD coverage in both left and right ventricles.

Indeed, the highest angle of rotation tested here (75 degrees) produced a 72% improvement in LV SW when compared to baseline. Interestingly, we also observed a stepwise decrease in ESV with increasing torsion angle in the LV, suggesting that AAT helps the ventricle to empty more completely during each cardiac cycle while also helping to unload the heart during the filling phase of the cardiac cycle (Figure 17).

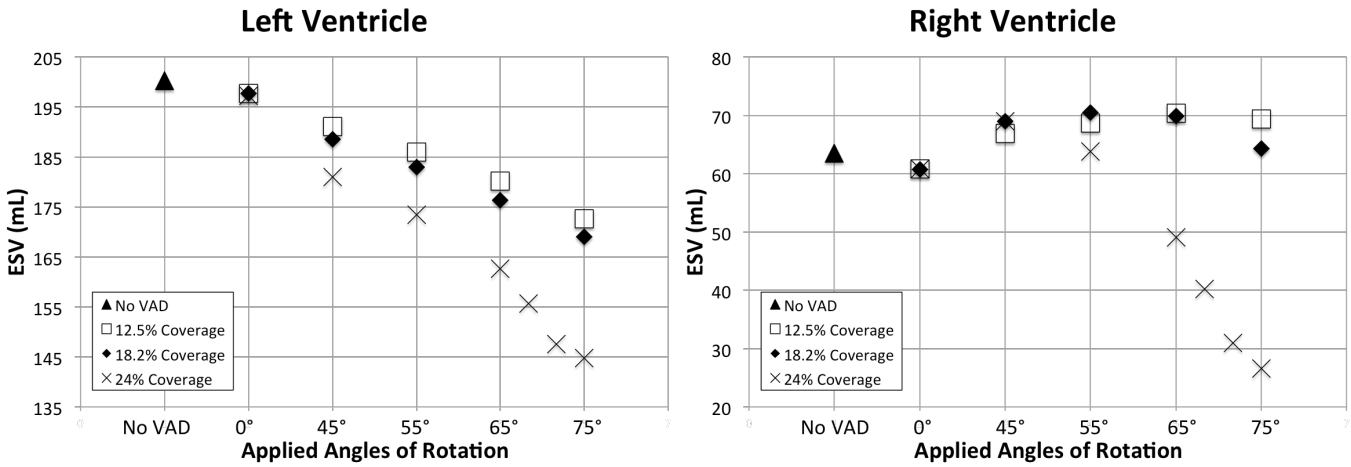

Figure 17: ESV as a function of the applied angle of rotation and tVAD coverage in both left and right ventricles.

3.2.2 Varying Device Coverage Area

Apical CA also proved to be a key factor in optimizing tVAD performance in these simulations, albeit to a lesser degree than rotation angle. Nevertheless, as device coverage was increased from 12.5 to 24%, there was a consistent trend toward healthier cardiac hemodynamics. Though the effects of CA on cardiac function were relatively subtle, EF, PSP and SW all increased and ESV decreased with greater device coverage (Tables 1-2). This general pattern was maintained across all three CAs tested, with the most marked improvements found in simulations with the highest device coverage.

3.2.3 Effects on Pressure and Volume

LV and RV pressures were plotted as a function of their respective volumes at varying rotation angles as a means to visualize the effects of AAT on global cardiac mechanics (Figures 18-19). As rotation angles were increased, the LV PV-loops became proportionally larger both in terms of pressure generation (vertical axis) and volume displacement (horizontal axis) when compared to the baseline clinical HF model. The widening of the PV-loops with increasing torsion angles suggests that tVAD actuation is effectively helping the ventricle to eject a greater volume of blood with every cardiac cycle, increasing CO proportionally. The lengthening of the PV-loops in the vertical direction with increasing torsion angles indicates that the tVAD is able to help generate higher arterial pressures by mechanically deforming the ventricular volume. And finally, the leftward shift of these loops indicates that AAT causes significant ventricular unloading, which may be beneficial as the heart remodels over time. These effects are subtler for the RV (Figure 19). The largest changes in the PV-loops occur for the two largest rotation angles (65 and 75 degrees).

Furthermore, we noted a large increase in EF, PSP and SW in the numerical experiments with largest apical CA. However, a potential plateau in the hemodynamic parameters occurs between 65 and 75 degrees. Two additional simulations at 68.33 and 71.67 degrees were completed to investigate this phenomenon. The results were consistent with the previous simulations where an upward trend in EF, PSP, and SW and a downward trend in the ESV were noted.

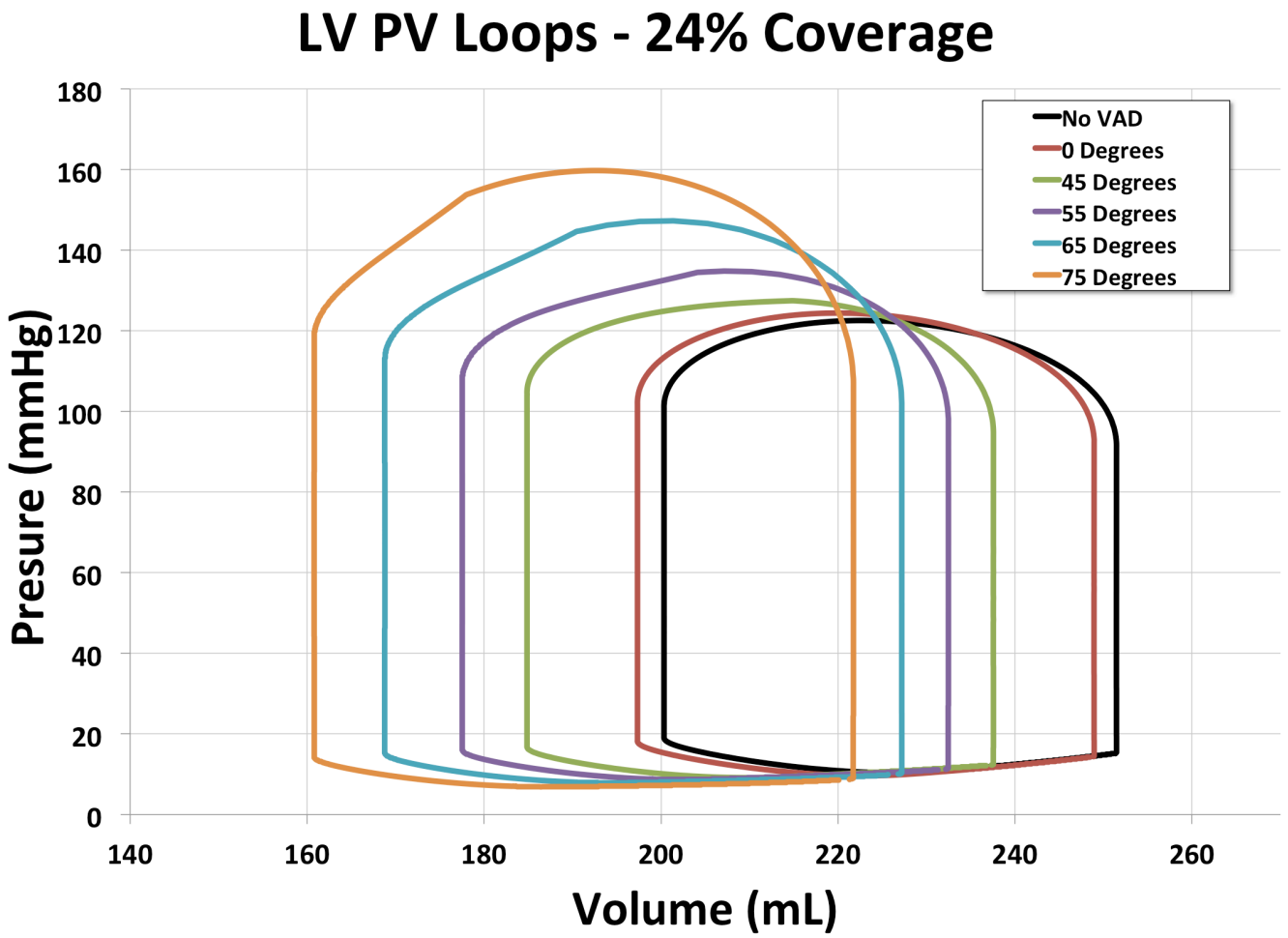

Figure 18: Left ventricular PV-Loops for a rotation study at the high (24%) coverage area.

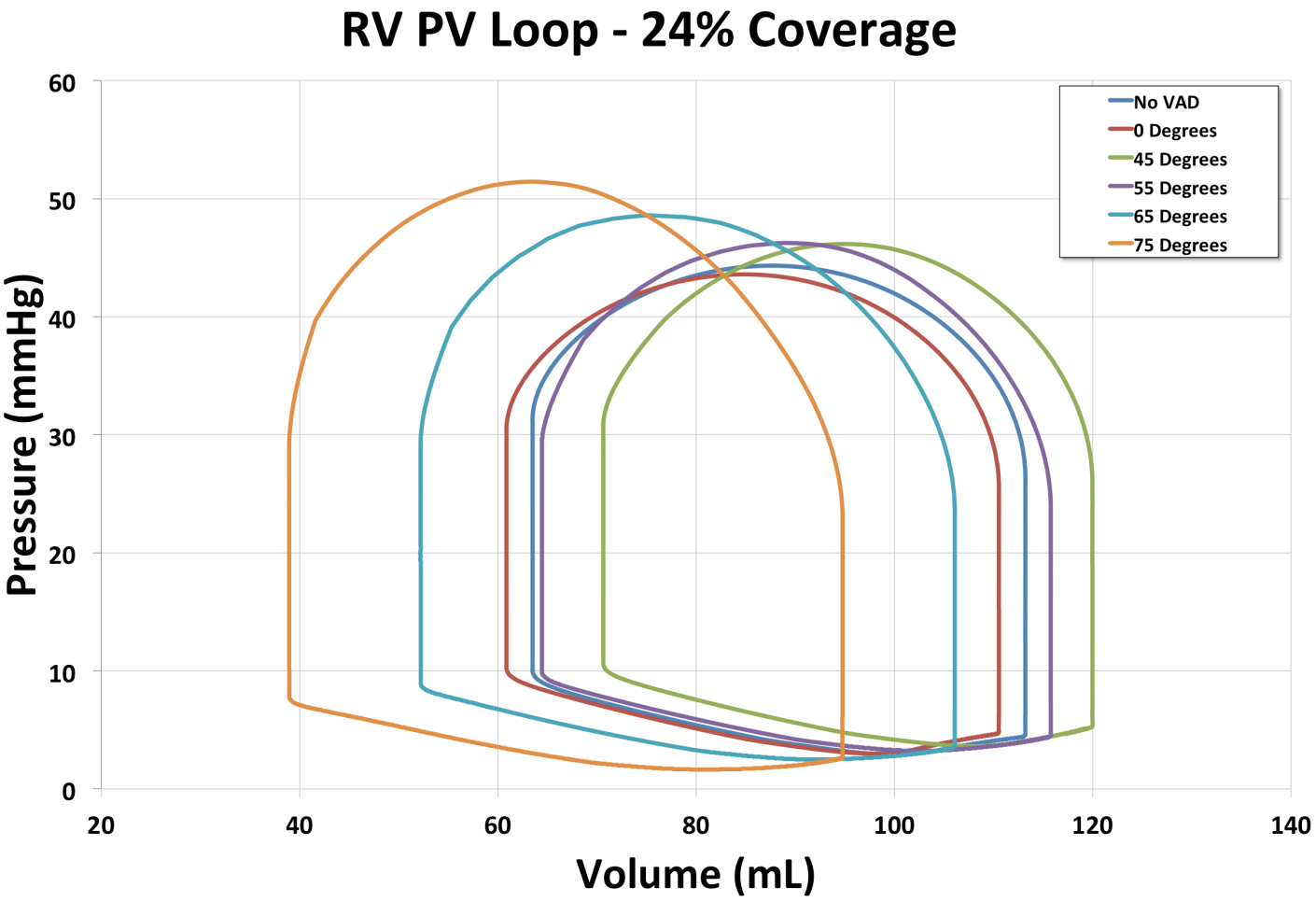

Figure 19: Right ventricular PV-Loops for a rotation study at the high (24%) coverage area.

3.3 Discussion

In this study, the effects of AAT on the failing heart were investigated in greater detail by conducting a series of parametric numerical experiments examining the effects of rotation angle and device CA using an advanced, biventricular model of a failing human heart. Results from these computational studies suggest that global hemodynamics of the failing heart can be significantly improved with AAT and that these improvements are a strong function of both ARA and device CA. Specifically, we found that EF, PSP and SW trended sharply upward with increasing ARA and CA while ESV values were significantly reduced.

When compared to the baseline pretreatment HF condition, the most aggressive tVAD assist approach tested—i.e., 24% CA and 75 degree rotation—increased LV EF and SW production by 49% and 72%, respectively. These same torsion parameters also yielded significant gains in EF (58%) and SW (49%) on the right side, which bodes well for the prospect of using AAT for biventricular support. Increases in LV EF for the small and intermediate coverage cases were modest. But when combined with moderate increases in peak LV pressures, a moderate increase in SW occurs for small coverage and a substantial increase occurs for intermediate coverage (Table 11). Simultaneously, ESV diminishes substantially in both cases. For the large coverage case, the increases in EF and SW are dramatic, along with large reductions in ESV. Some other potential important findings are the large increases in SW for both ventricles between the 65 and 75-degree cases, particularly for the largest coverage (Tables 11 and 12). The hemodynamic improvements between 65 and 75 degrees also seemed to plateau, especially with larger CAs. Extra simulations at 68.33 and 71.67 degrees for the large CA were completed, which confirmed that hemodynamics increased and decreased with a similar trend to the rest of the results. However, hemodynamic returns lessened as the rotation

angle neared 75 degrees. ***Based on these findings, assist for the large CA with ARA between 72 and 75 degrees may be the optimal tVAD working parameters.***

Overall, results from the first realistic biventricular simulations of AAT are encouraging, and raise some other issues and questions that can be addressed with additional simulations using versions of the existing computational model, including the following. The timing and duration of the applied rotation for all of our studies has been a sinusoidal systolic rotation that takes one-quarter of the cardiac cycle and a linear return rotation taking up the remainder of each cardiac cycle. However, reviewing the PV-loops (Figures 18-19) shows that this timing may not be optimal, especially with regard to the LV loops with ARAs of 55 through 75 degrees. It appears that ejection diminishes substantially at times considerably before isovolumic relaxation starts. Therefore, it may be possible to increase ejection with longer systolic rotations for these cases.

An effort to increase the coverage region to 36% failed, even for ARAs as low as 45 degrees. One hypothesis that may explain these diverging solutions is described under the limitations section below. However, it may be worthwhile to attempt 30% coverage with a modification of one of the existing models. Even if solutions can be obtained only for lower maximum ARAs, they may provide an upper limit on coverage (above 24%) that still yields substantial improvement in function without the more severe rotations. Finally, all of these studies were performed with models that produced baseline LV EFs of about 20%. But, EFs in HF are highly variable from patient to patient. Therefore, a parametric study in which the baseline EF is varied should also be performed, and will also be further discussed in Chapter 5. This requires careful tuning of the dynamic model and/or the parameters of the circulatory model. In particular, it will be important to determine whether or not considerably greater

improvements in function can be achieved with applied rotation in HF cases that are even worse, with EFs at 15% or even 10%, as have been reported in the clinical literature [2].

The ultimate goal of these follow-on experiments would be to guide the design of a clinically relevant tVAD interface and actuation mechanism that can be used to test and validate this approach on the bench top, in porcine HF models and, ultimately, in clinical CHF patients. For these simulations of a CHF heart model with a baseline EF of 20%, we have narrowed down an optimal set of working parameters, especially at the large CA. It is foreseeable to improve hemodynamic returns at lower CAs by further investigating the other methods mentioned, e.g., adjusting the timing or varying the functions of the applied rotation.

3.4 Study Limitations

Although there are numerous advantages to using a computational model to quantify the effects of AAT on the beating heart, the limitations of this study fall mainly on the assumptions of the model itself. In these computational experiments we have addressed the fundamental limitations of our first computational study by replacing the 18-element simplified pig prolate spheroidal model with a more realistic biventricular model based on measurements from a clinical patient with dilated cardiomyopathy. By adopting this advanced beating heart computer model, results from these simulations are far more realistic than those reported earlier. At the same time however, the computational complexity of this model and its realistic replication of a failing human heart result in much longer simulation run times. This makes comprehensive parametric studies of the sort needed to thoroughly characterize tVAD performance under a wide range of clinical conditions difficult, expensive and time consuming. The simulations with increasing values of maximum ARA take considerably longer to converge than our typical baseline simulations of HF. One hypothesis that may explain this phenomenon is an interaction

between active state and the applied rotation. Fortunately, the finding that the use of the final conditions for a run involving a smaller angle as the starting point for a subsequent run with a larger angle obviates this difficulty somewhat. Also, it is important to note that while simulations of this sort provide important information regarding the biomechanics of AAT that would be difficult or impossible to obtain experimentally, they cannot determine the biological effects of tissue/device interactions or predict damage that might occur at the cellular level with the cyclic application of torsional stress across the ventricular walls.

Indeed, though the improvements in global cardiac hemodynamics reported here are very promising, the extent to which this artificial wringing of the heart is likely to injure the myocardium, damage the epicardial surface, compromise valve function, or interfere with normal sinus rhythm remains an open question. In prior experimental work performed in pigs, acute application of the tVAD did not generate any visible damage to the beating heart or induce any noticeable adverse cardiac events [28]. However, the long-term effects of applied torsion on the overall health of the heart can only be inferred from forthcoming computational analyses in which myocardial finite strains, accompanying stresses and force resultants, particularly in the neighborhood of the mitral annulus, are estimated. And, they must be confirmed via chronic implant trials.

3.5 Potential Advantages of tVAD Support

These multi-scale simulation studies strongly suggest that, from a purely biomechanical standpoint, AAT has the potential to be an effective means to support the failing heart without the problems of thrombolysis and blood activation common to all blood contacting cardiac assist devices. As such, this approach would effectively eliminate the need for anticoagulation and avoid long-standing blood handling complications that have largely limited VAD use to rescue

and bridge-to-transplant applications. Also, because of its positioning at the apex of the heart with contact surfaces extending up the walls of both ventricles, the tVAD has the potential to provide true biventricular support, whereas most clinical devices currently on the market address left HF alone. This is an important distinction because, while some patients who present with biventricular failure can show improvement in right heart function with left heart support, there are far fewer options available for patients with true biventricular HF. The tVAD could be used, in principle, to treat this underserved patient population.

Another potential benefit of this approach stems from the fact that the tVAD works by extending the natural twisting motion of the heart to improve ventricular ejection. This singular mechanism may provide a means to unload the ventricles while allowing the myocardium to continue to contract, which could conceivably promote cardiac recovery over time. Should the heart respond to chronic tVAD therapy by gradually regaining contractile function, the patient could be weaned easily from the device by systematically lowering the level of rotational assist to provide the minimum level of support needed. If myocardial reverse remodeling were to advance to the point where normal cardiac function was fully restored, the device could either be removed entirely or deactivated in situ to retain the option of further support should the need arise.

3.6 Future Work

Beyond this, further studies will be needed to understand the resulting stresses and strains that the heart experiences as these torsional deformations are imposed on the myocardium, which will be discussed in Chapter 4. Similarly, because it may be possible to increase ejection with longer periods of systolic applied torsion, further parametric studies investigating the timing of ATT will be evaluated in Chapter 5. Furthermore, studies are needed to examine the effects of

varying modes of HF and cardiac disease states, e.g., varying levels of ventricular dilation, right ventricular failure, cardiac hypertension and myocardial infarction. In this vein, there should be an effort to create new computational cardiac models (this will be discussed in Chapter 5). The final task to be accomplished prior to in vivo device testing will be to develop a method to securely attach the tVAD to the epicardial surface of the heart. The challenge here will be to design an attachment scheme that will provide secure fixation of the device to the smooth, slick surface of the heart while causing minimal damage to the epicardium.

Chapter 4

Computational parametric studies investigating the biomechanical effects of applied apical torsion for cardiac assist

The hemodynamic analysis of the parametric simulations completed in Chapter 3 demonstrated that AAT has the potential to significantly improve the hemodynamic function of a failing heart with increasing levels of rotation and CA. It was observed that an increase in the levels of AAT resulted in an increase in ejection fraction and stroke work and a return towards healthier cardiac hemodynamics [61]. Similarly, although the effects were relatively subtle compared to varying the amount of AAT, an increase in device CA also resulted in increases in hemodynamic returns. The potential hemodynamic improvements were also explored and substantiated by the experiments of Roche et al. [27, 58] where it was demonstrated that AAT could increase the volumetric output of the ventricles.

Although these initial hemodynamic results were encouraging, questions still remain about the effects of AAT on the cardiac tissue. Specifically, because the AAT is at levels above what is normally observed physiologically, it is unclear how such applied torsion affects the myocardium. However, there is to be expected an increase in the stresses and strains experienced by the myocardium. Therefore, the resulting cardiac biomechanics of these

parametric studies should also be evaluated to determine how AAT affects the heart tissue and the realistic working limits of the tVAD.

Especially of interest are the stresses and strains experienced by the myocardium at the ventricular base and base of the device. This chapter reports resulting effects of Chapter 3's parametric computational simulations evaluating the effects of using a torsional ventricular assist device (tVAD) on a patient-specific bi-ventricular failing heart model on regional cardiac biomechanics. The goal of this study was to examine the effects on cardiac biomechanics produced by varying ARA in order to determine the practical working limits of AAT. Results indicate that with increasing levels of AAT, there are increasing magnitudes of stress and strain in the myocardium at the ventricular and tVAD base. This suggests that, although AAT provides meaningful returns to hemodynamic function in a failing heart, the large deformations resulting from AAT could potentially damage the heart. However, lower AAT angles – closer to that of the native left-ventricular torsion – coupled with another means of external cardiac compression may prove to be a viable method of cardiac assist.

4.1 Materials and Methods: An Extension of Parametric Computational Simulations

This chapter evaluates the resulting regional cardiac biomechanics from the parametric computational simulations described in Chapter 3. In that previous study, three distinct device CAs were simulated where moving boundary conditions were applied on select finite element nodes at and basal to the apex, simulating tVAD CAs of 12.5, 18.2 and 24% of the longitudinal distance from the apex towards the base of the ventricles. This simulated device was rotated counterclockwise, as viewed from the apex, at the apical region of the ventricles for 187.5 ms (peak time, PT) during isovolumic contraction and most of ejection and rotated back for the

remainder of each 750 msec cardiac cycle, which is equivalent to 80 beats per minute (Figure 12b-c). Because it was previously found in Chapter 3 that increasing ARA and device CA resulted in greater hemodynamic returns, regional cardiac mechanics were evaluated only for the largest CA, as this CA produced the largest improvement in hemodynamics, and at all levels of AAT support. These results were then compared with the regional mechanics estimated from the baseline HF model (NoVAD). To quantify the effects of increases in peak rotation angles, the symmetric Lagrangian strain and Cauchy stress tensors in fiber coordinates were calculated for every node at each time step of the cardiac cycle and were plotted against time throughout that cycle. A subset of results at specific finite element nodes is presented here. Specifically, the principal strains and stresses were estimated to identify regions of large net changes in the maximum and minimum strain and stress values. Their contributing normal and shear components in fiber coordinates (Figure 3, Table 13) were also computed. In Table 1, the notation for strain and stress components in fiber coordinates is defined. Of particular interest were the maximum principal strains and stresses at the nodes of the base of the ventricles and the basal edge of the apical torsion region where the tVAD cup is placed (Figures 20-21). The locations of the nodes of interest within the biventricular model are listed in Table 14.

Table 13: Stress and strain component labels.

	Component	***Component Type***
Principal	P1	Minimum Principal Stress or Strain
	P2	Intermediate Principal Stress or Strain
	P3	Maximum Principal Stress or Strain
Normal	T11/E11	Fiber-Fiber Stress/Strain
	T22/E22	Crossfiber-Crossfiber Stress/Strain
	T33/E33	Transmural/Transmural Stress/Strain
Shear	T12/E12	Fiber-Crossfiber Stress/Strain
	T13/E13	Fiber-Transmural Stress/Strain
	T23/E23	Crossfiber-Transmural Stress/Strain

Table 14: Locations of nodes in mesh of heart model.

Ventricular Basal Nodes	*Location*	*tVAD Basal Nodes*
	Epicardial Nodes	
81	RV free wall	***98***
82	Posterior septal wall	***99***
86	LV free wall	***103***
90	Anterior septal wall	***107***
	Endocardial Nodes	
3	Septal wall of LV	***27***
4	Posterior septal wall	***28***
14	LV free wall	***38***
20	Anterior septal wall	***44***
74	RV free wall	***91***

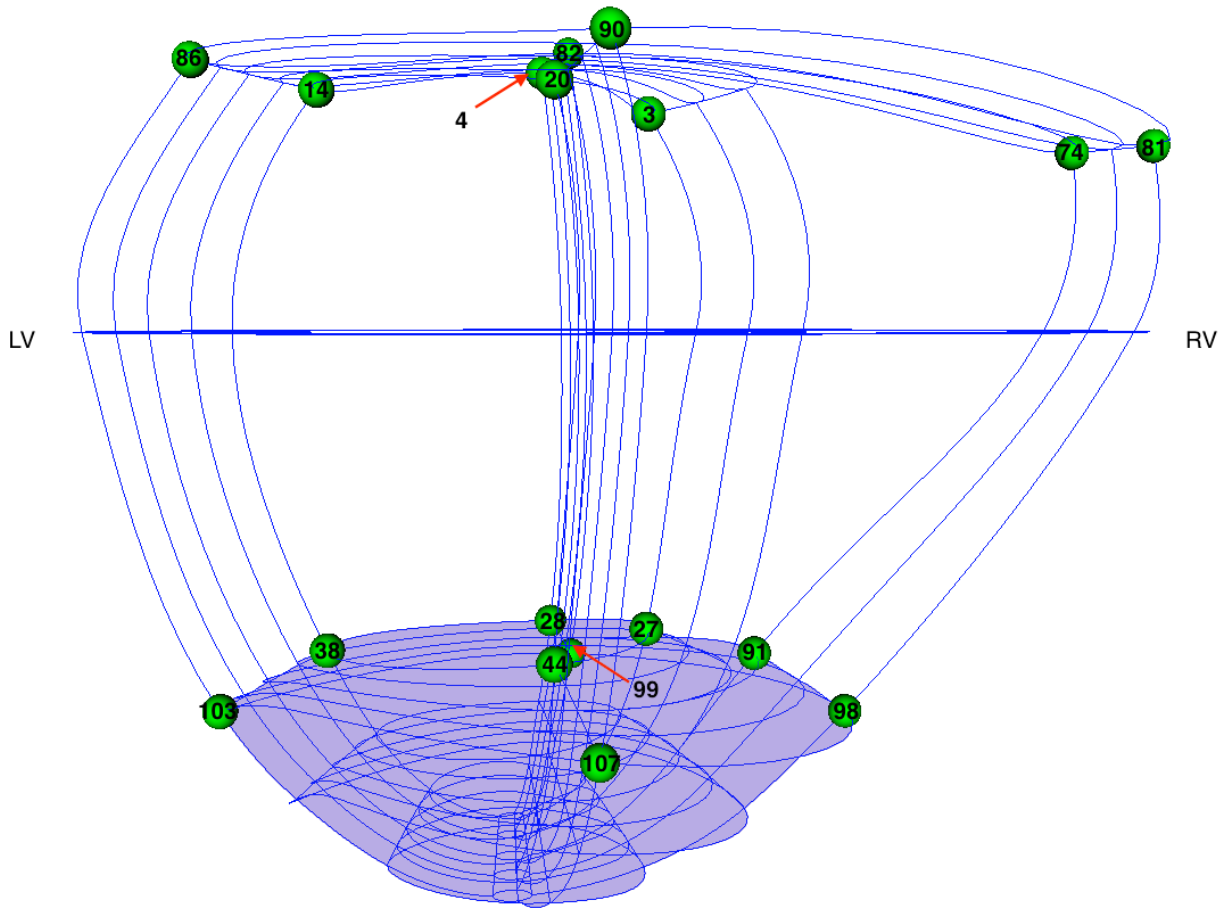

Figure 20: Anterior-posterior view of the epicardial and endocardial nodes at the base of the ventricle and base of the tVAD, which is highlighted at the apex of ventricle.

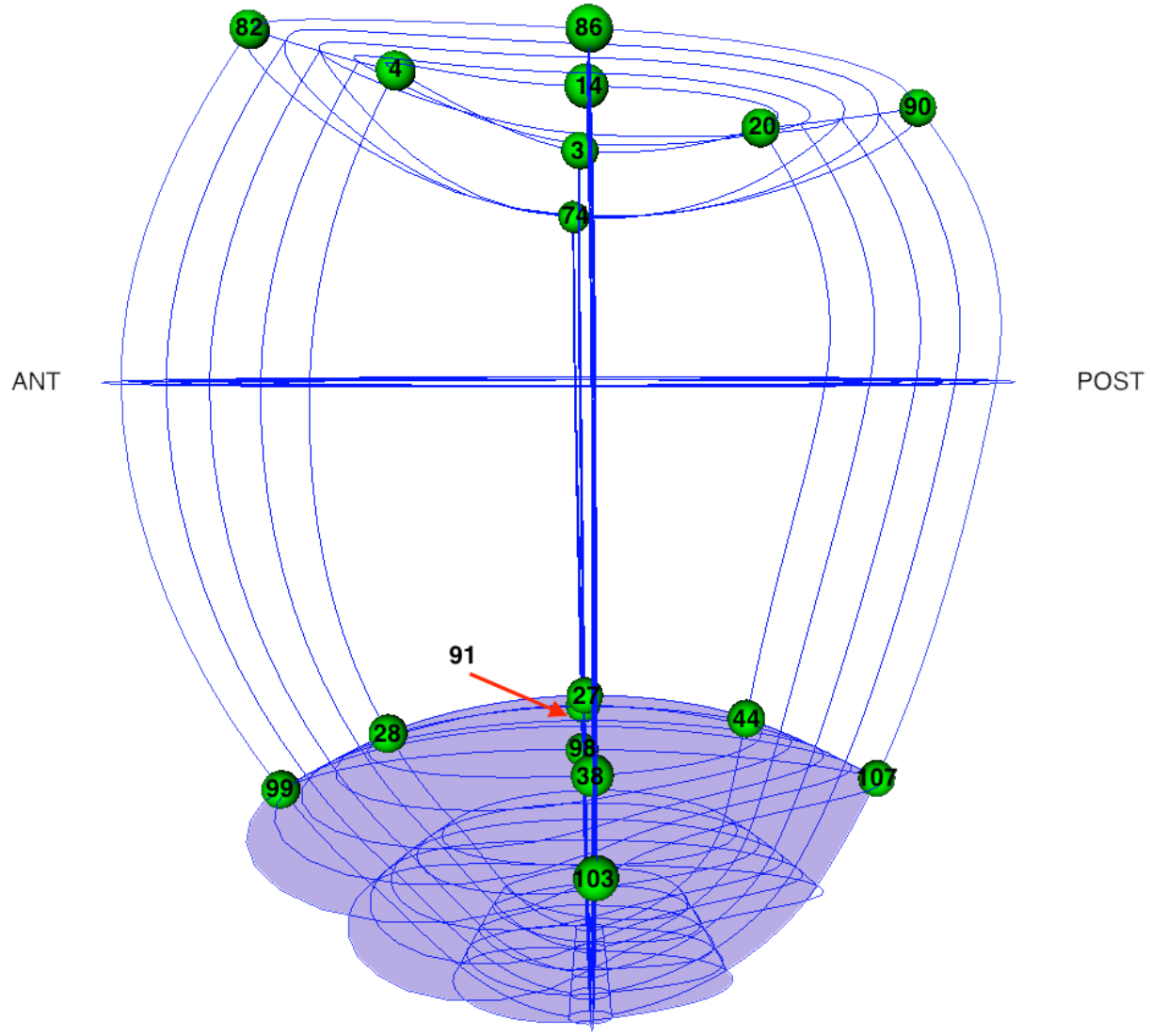

Figure 21: Left lateral view of the epicardial and endocardial nodes at the base of the ventricle and base of the tVAD, which is highlighted at the apex of ventricle.

4.2 Biomechanical Results of Parametric Computational Studies

Although previous results describing improvements in global hemodynamics were well-converged up to peak apical rotations of 75 degrees, regional wall mechanics at rotations above 65 degrees yielded excessive levels of strain and accompanying stress. Increases in the maximum principal stress at the epicardium of the left ventricular base showed a nonlinear trend with angle as would be expected with the nonlinear constitutive law employed. However, a large jump in this principal stress occurred at a rotation of 75 degrees. Moreover, the product of the principal stretch ratios (J = det F) started to deviate from unity at a number of finite element nodes. Therefore, we determined that AAT above the level of 65 degrees is not accurate under the assumptions of the numerical methods used. Perhaps this could be overcome with a considerably larger model (more nodes, elements and degrees-of-freedom) and a higher bulk modulus, but such an exercise would not be useful since strain and stress estimates are already quite high for the 65-degree case. Therefore, we believe that results from the 75-degree case are not reliable, and they have either been discarded or red-flagged in certain time series plots in which they are still following the patterns shown at lower rotation angles.

Based on these simulations, we determined that increasing levels of AAT yielded significant net increases in the magnitudes of myocardial stresses and strains (Tables 15-16). With increasing levels of AAT, very large P3 stresses were observed at multiple nodes along the epicardium and endocardium of the ventricular base and the endocardium at the device base. . Maximum principal strains greater than 0.60 were observed in multiple nodes along the epicardial and endocardium of the ventricular base. Maximum principal stresses greater than 100 kPa were observed in multiple nodes along the epicardium and endocardium of the ventricular base and in the endocardium at the device base. The largest P3 stress observed with 65 degrees

Table 15: Absolute maximum principal nodal strains for the basal epicardial (EPI) and endocardial (ENDO) of the ventricle and tVAD.

Nodes	***Maximum Strain***					***Change in Strain***
	No VAD	***45 Degrees***	***55 Degrees***	***65 Degrees***	***75 Degrees***	
EPI Basal Ventricle						
81	0.0825	0.4831	0.5497	0.5805	0.6449	0.5624
82	0.2682	0.5544	0.6111	0.6524	0.6652	0.3970
86	0.4583	0.8073	0.8737	0.8917	0.9054	0.4471
90	0.2319	0.6907	0.7431	0.8064	0.8638	0.6319
EPI Basal tVAD						
98	0.2087	0.5501	0.5881	0.6446	0.7560	0.5474
99	0.1545	0.7094	0.7522	0.7641	0.7546	0.6001
103	0.2210	0.4185	0.5368	0.6303	0.6909	0.4699
107	0.0960	0.6917	0.7266	0.7646	0.7848	0.6888
ENDO Basal Ventricle						
74	0.1826	0.1506	0.1341	0.0953	0.0565	0.1261
4	0.3850	0.3979	0.4133	0.4250	0.4422	0.0572
14	0.5618	0.3725	0.3708	0.4085	0.4689	0.0929
20	0.5117	0.3602	0.3397	0.3162	0.2702	0.2415
3	0.5307	0.4078	0.3883	0.3492	0.2960	0.2347
ENDO Basal tVAD						
91	0.1418	0.1739	0.1638	0.1286	0.1532	0.0114
28	0.4364	0.3265	0.3235	0.3358	0.3541	0.0824
38	0.3924	0.3014	0.2811	0.2798	0.3270	0.0654
44	0.3360	0.3372	0.3190	0.3080	0.3258	0.0101
27	0.2832	0.2382	0.2680	0.3144	0.3640	0.0808

Table 16: Absolute maximum principal stresses (kPA) for the basal epicardial (EPI) and endocardial (ENDO) nodes of the ventricle and tVAD.

Nodes	***Maximum Stress (kPa)***					***Change in Stress***
	No VAD	***45 Degrees***	***55 Degrees***	***65 Degrees***	***75 Degrees***	
EPI Basal Ventricle						
81	17.65	43.68	79.06	162.2	305.1	287.45
82	44.59	5.468	5.542	5.619	34.55	10.04
86	80.21	157.0	212.5	287.8	436.2	355.99
90	30.92	45.96	75.25	105.2	126.4	95.48
EPI Basal tVAD						
98	20.48	64.45	90.53	116.7	142.1	121.62
99	31.07	49.83	92.42	148.5	197.4	166.33
103	54.16	38.50	53.29	67.65	84.28	30.12
107	25.65	68.80	117.7	180.5	253.2	227.55
ENDO Basal Ventricle						
74	9.229	32.31	60.05	86.97	124.0	114.771
4	44.25	65.98	74.34	86.80	96.73	52.48
14	60.41	59.24	67.88	75.83	75.56	15.15
20	56.09	24.97	22.90	23.03	43.30	12.79
3	28.08	3.775	6.078	14.06	22.36	5.72
ENDO Basal tVAD						
91	9.794	6.469	20.64	29.13	31.82	22.026
28	47.63	55.16	59.90	65.19	69.59	21.96
38	49.99	52.38	58.73	65.77	72.13	22.14
44	76.56	114.7	134.8	162.0	186.6	110.04
27	47.64	46.17	48.47	52.21	69.19	21.55

of AAT at the base of the ventricle were of 287.8 kPa at the basal node of the left ventricular epicardium (N86) and at the base of the device was 162.0 kPa at the node of the device base at the endocardial anterior septal wall (N81) (Table 16). Similarly, very large P3 strains were observed in multiple nodes along the epicardium and endocardium of the ventricular base with increasing levels of AAT. The largest P3 strains observed were 0.89 at the basal epicardial node of the LV free wall (N86) and 0.81 at the basal epicardial node of the ventricular anterior septal wall (N90). The largest increase in P3 strain (ΔE) was also at these epicardial nodes along the ventricular and tVAD base, where all nodes had $\Delta E \geq 0.40$ (Table 15). Not surprisingly, the greatest increase in P3 stress (ΔT) was observed at the epicardial nodes for both the ventricular and device base, where nearly 75% of the nodes at $\Delta T>100$ kPa (Table 16).

Although AAT results in very large increases in myocardial stress and strain, as the simulated device was rotated, the patterns of maximum principal (P3) strains and stresses at the epicardial nodes over the course of a cardiac cycle were generally similar to one another, differing only with the increasing magnitudes of the observed strains and stresses or when compared to the HF model. This is demonstrated in the top panels of Figure 22 where nodes 81 and 86, which despite having the largest P3 stresses, had a stress over time pattern similar to that of the HF model. P3 strains also generally had similar patterns of strain over time plots, differing only in the magnitude of the strains, as demonstrated by nodes 81 and 86 in the bottom panels of Figure 22. This could also be said for the majority of the endocardial nodes at both the ventricular and tVAD base.

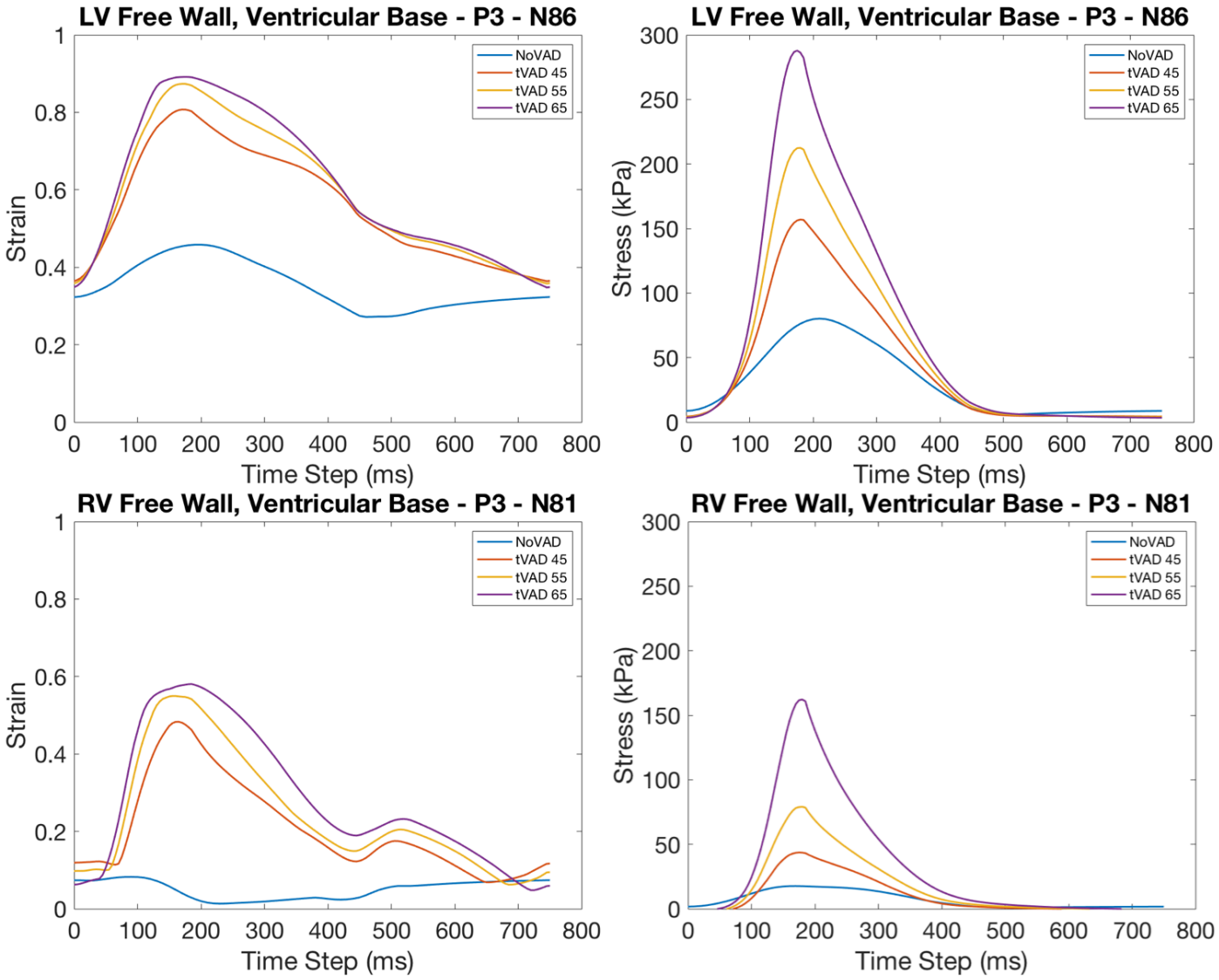

Figure 22: Maximum principal strains and stresses (kPa) for each simulation test case over the cardiac cycle for the epicardial node at the RV free wall of the ventricular base (Node 81, top left and right) and the endocardial node at the posterior septal wall the ventricular base (Node 4, bottom left and right).

In order to better visualize the regions of patterns of myocardial stress and strains and what was happening at those locations, P3 stresses and strains were rendered and selected nodes were evaluated to determine the major contributing component of the P3 stresses or strains. At the ventricular basal node of the LV free wall (N98) the P3 strain is dominated by the crossfiber-crossfiber normal strain component (E22) for the HF case and by the fiber-transmural shear

strain component (E13) for the 65 degree case. However, at the endocardial basal node of the RV free wall at the device base (N98), the P3 strains are dominated by the E22 strain for both the HF and 65 degree case (Figure 23). This was consistent with the strain renders, which showed that the endocardium had intermediate levels of strain, while the epicardium was more uniformly under high strain (Figure 24).

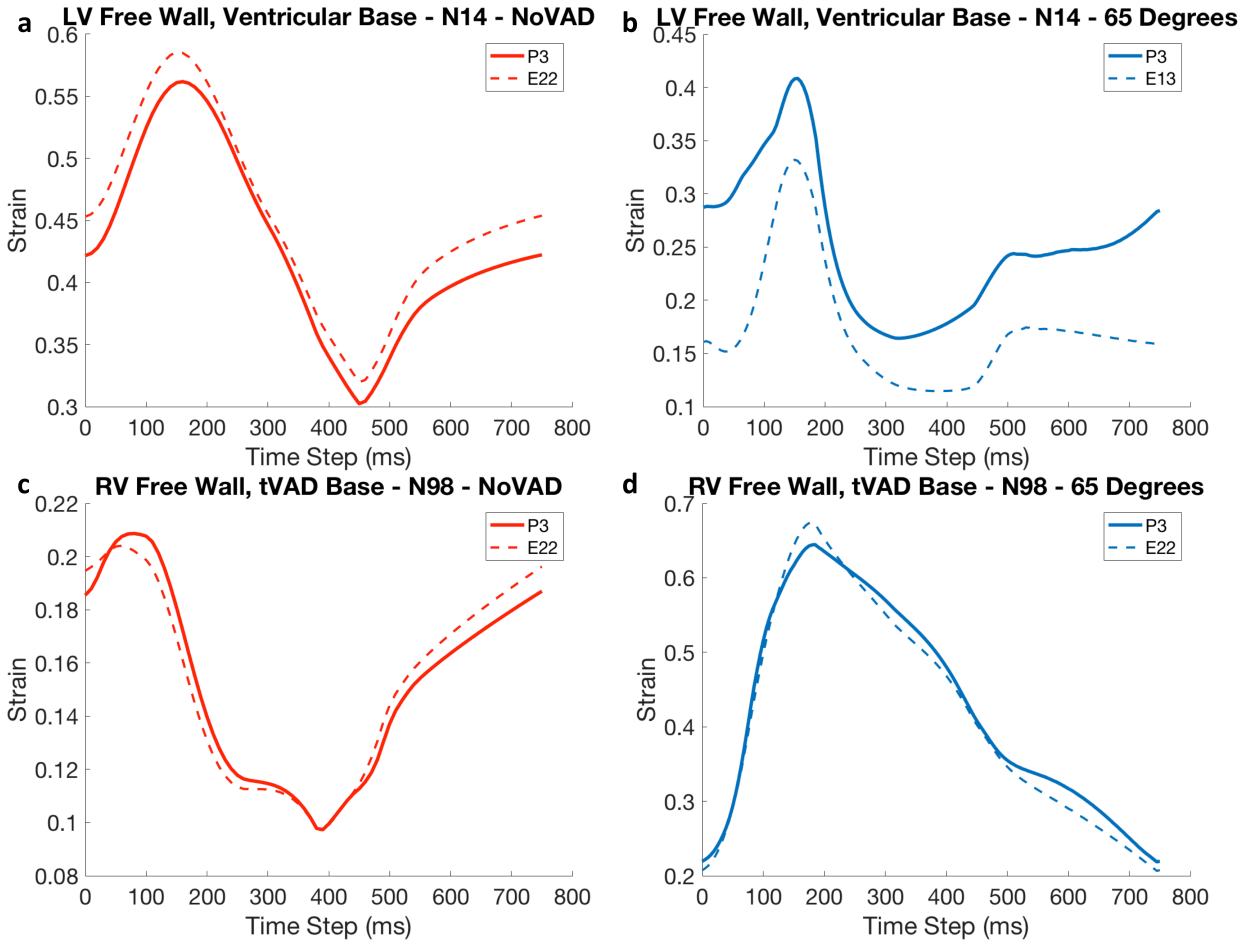

Figure 23: The P3 strains over the course of the cardiac cycle is also compared to their major component strains for node 14 – a) NoVAD HF case, and h) 65 degree AAT – and node 98 – i) NoVAD HF case and j) 65 degree AAT case

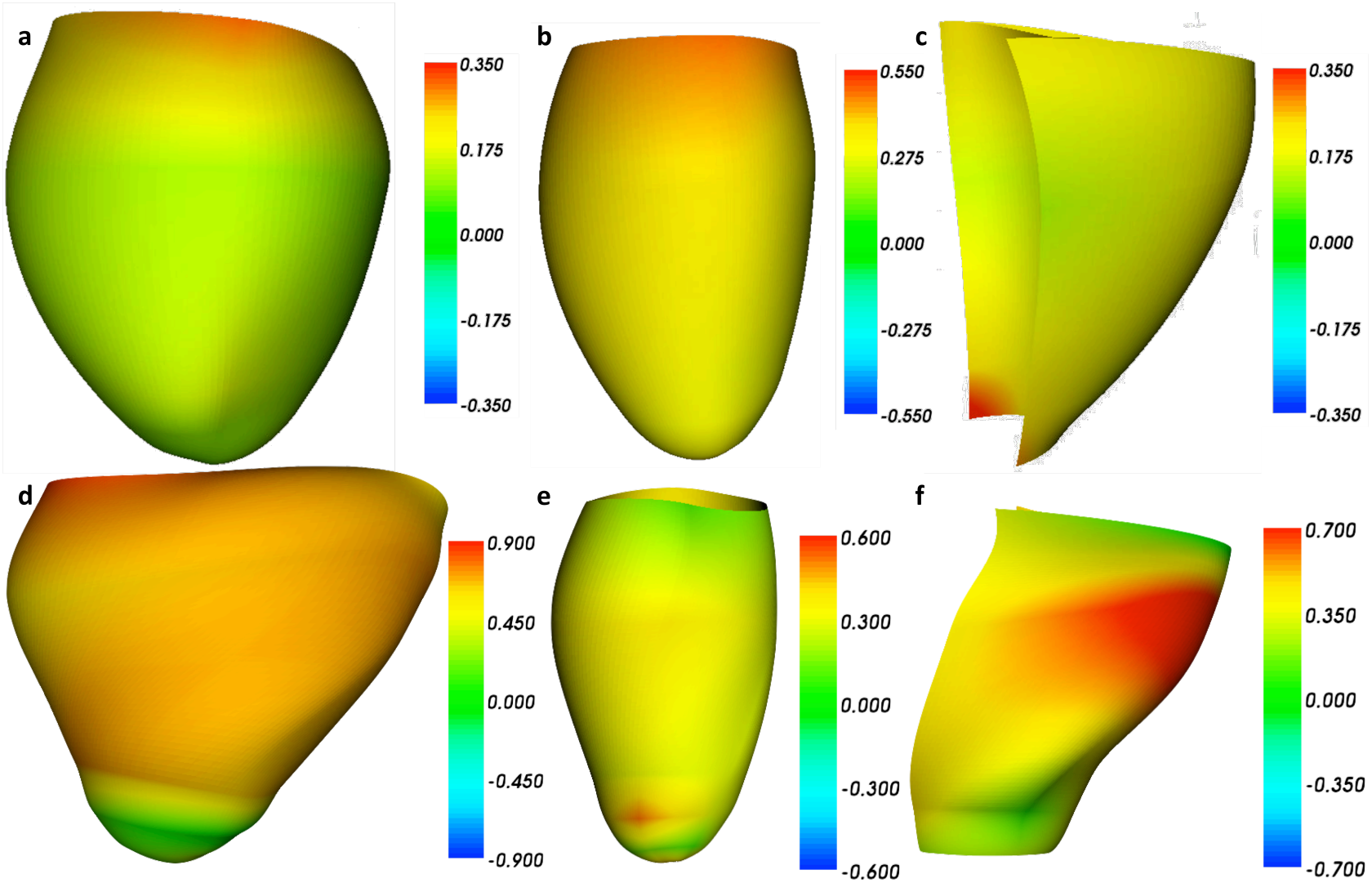

Figure 24: Maximum principal strains (P3) at peak time (187.5 ms) rendered on the deformed surfaces for the NoVAD case – a) biventricular epicardial surface in the left lateral view b) left ventricular endocardium in the anterior-posterior view, and c) right ventricular endocardium in the anterior-posterior view – and the 65 degree case – d) biventricular epicardial surface in the anterior-posterior view e) left ventricular endocardium in the left lateral view, and f) right ventricular endocardium in the anterior-posterior view.

The P3 stress for N14 was dominated by crossfiber-crossfiber normal stress component (T22) for the HF case and the fiber-fiber normal stress component (T11) for the 65 degree case. For N98, the P3 stress was dominated by T11 stress for the HF case and by a combination of T22 normal strain and crossfiber-transmural shear stress (T23) for the 65 degree case (Figure 25). Through the stress renders, we observed smaller regions of high significant high P3 stress for multiple locations in the myocardium (Figure 26).

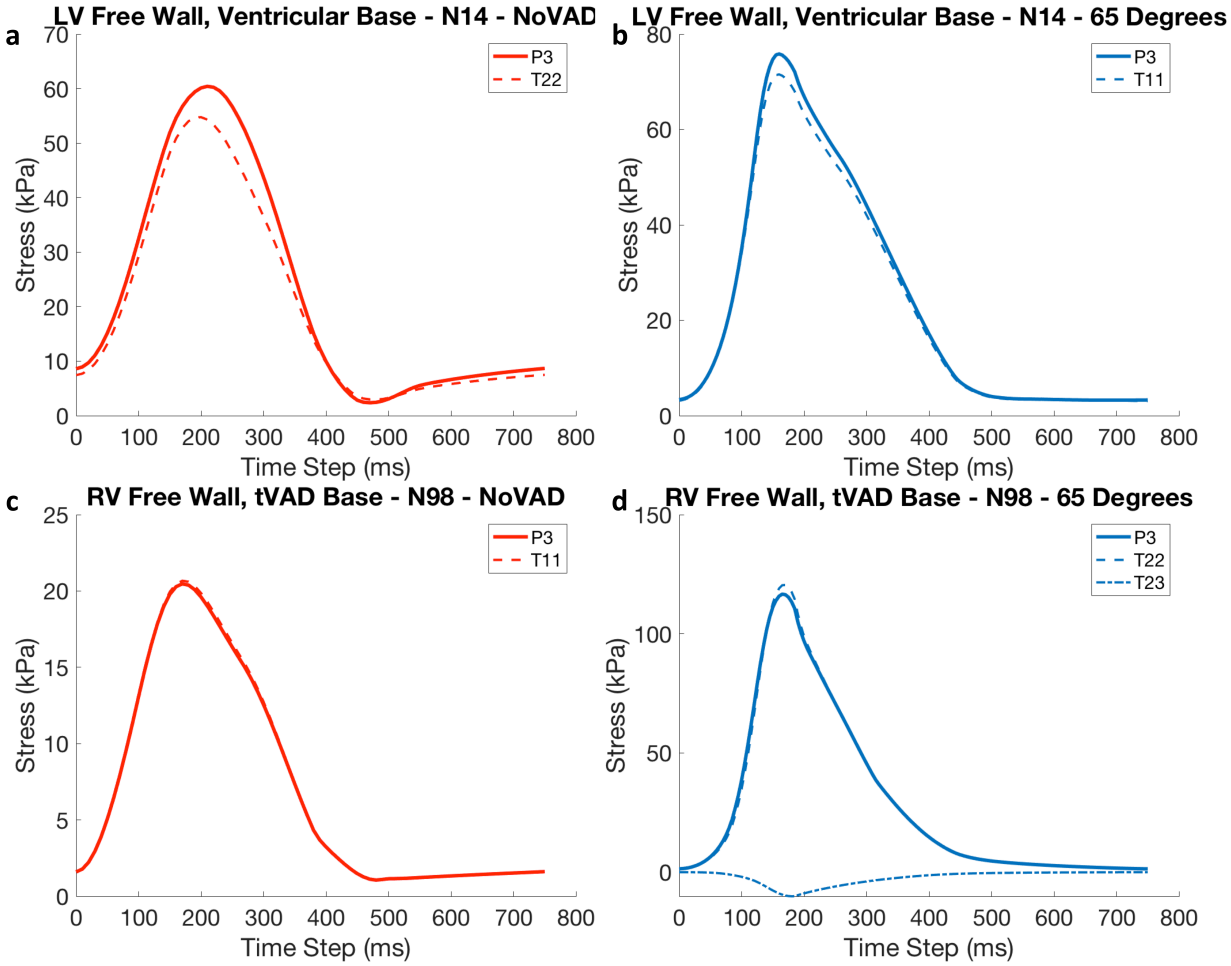

Figure 25: The P3 stresses over the course of the cardiac cycle is also compared to their major component strains for node 14 – a) NoVAD HF case, and h) 65 degree AAT – and node 98 – i) NoVAD HF case and j) 65 degree AAT case

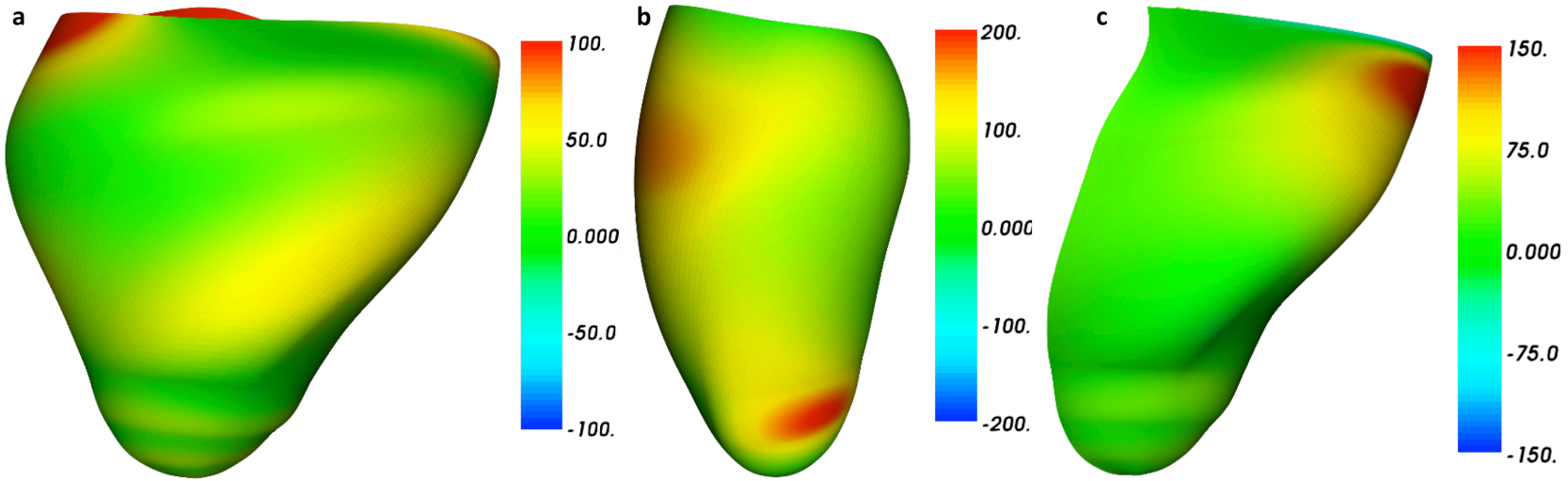

Figure 26: Maximum principal stresses (P3) at peak time (187.5 ms) rendered on the deformed surfaces for the 65 degree AAT case – a) biventricular epicardial surface in the anterior-posterior view, b) left ventricular endocardium in the left lateral view, and c) right ventricular endocardium in the anterior-posterior view.

When compared with the NoVAD HF model's baseline P3 stress and strain, some AAT nodal stresses and strains countered the native deformation of the cardiac tissue over the course of a cardiac cycle. This variation depended on the location of the stresses and strains in the myocardium (as determined by the nodes). Generally though, when comparing the NoVAD HF model with AAT, P3 strains were amplified at the epicardial nodes and reduced at the endocardial nodes, while P3 stresses were amplified in both the epicardium and endocardium with the application of torsion. Also of note is the observation that the P3 stresses and strains at the node of the endocardial anterior septal wall at the ventricular base (N20) and at the endocardial node of the RV free wall at the device base (N91) had differing patterns of deformation when compared to the NoVAD HF model, however, neither endocardial node had P3 stresses and strains as large as those observed in the epicardial nodes (Tables 15 and 16). Although endocardial nodes generally demonstrated a decrease in absolute P3 strains and increase in absolute P3 stresses with increasing levels of torsion, N20 saw a decrease in both P3 strains and stresses. At N91, P3 strains decreased with increasing levels of torsion, but of note is the large change in stress between the 45 degree and the 55, when compared to other endocardial nodes. In order to better understand what contributed the most to the P3 stresses and strains, all components of stresses and strains in fiber coordinates (see Table 13) were analyzed and compared for the nodes of interest (Figures 27-30). Based on this analysis, it appeared that the P3 stresses for both the HF model and AAT cases were dominated by the T11 normal stresses. The components that contributed to the P3 strains for the HF model was the E22 normal strain, while the E13 shear strain appears to contributed the most for the tVAD simulations.

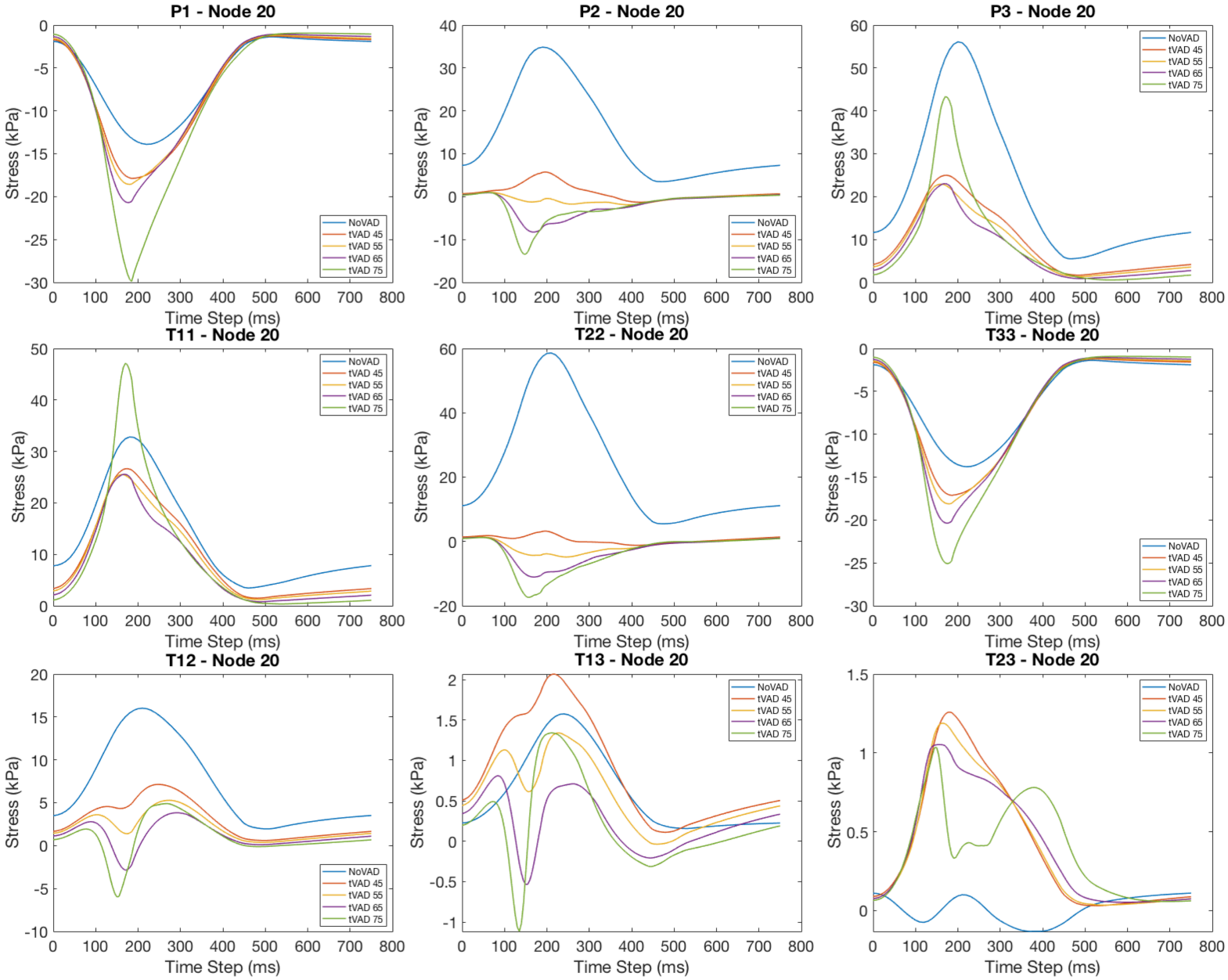

Figure 27: Component stresses for the endocardial node at the anterior septal wall of the ventricular base (Node 20).

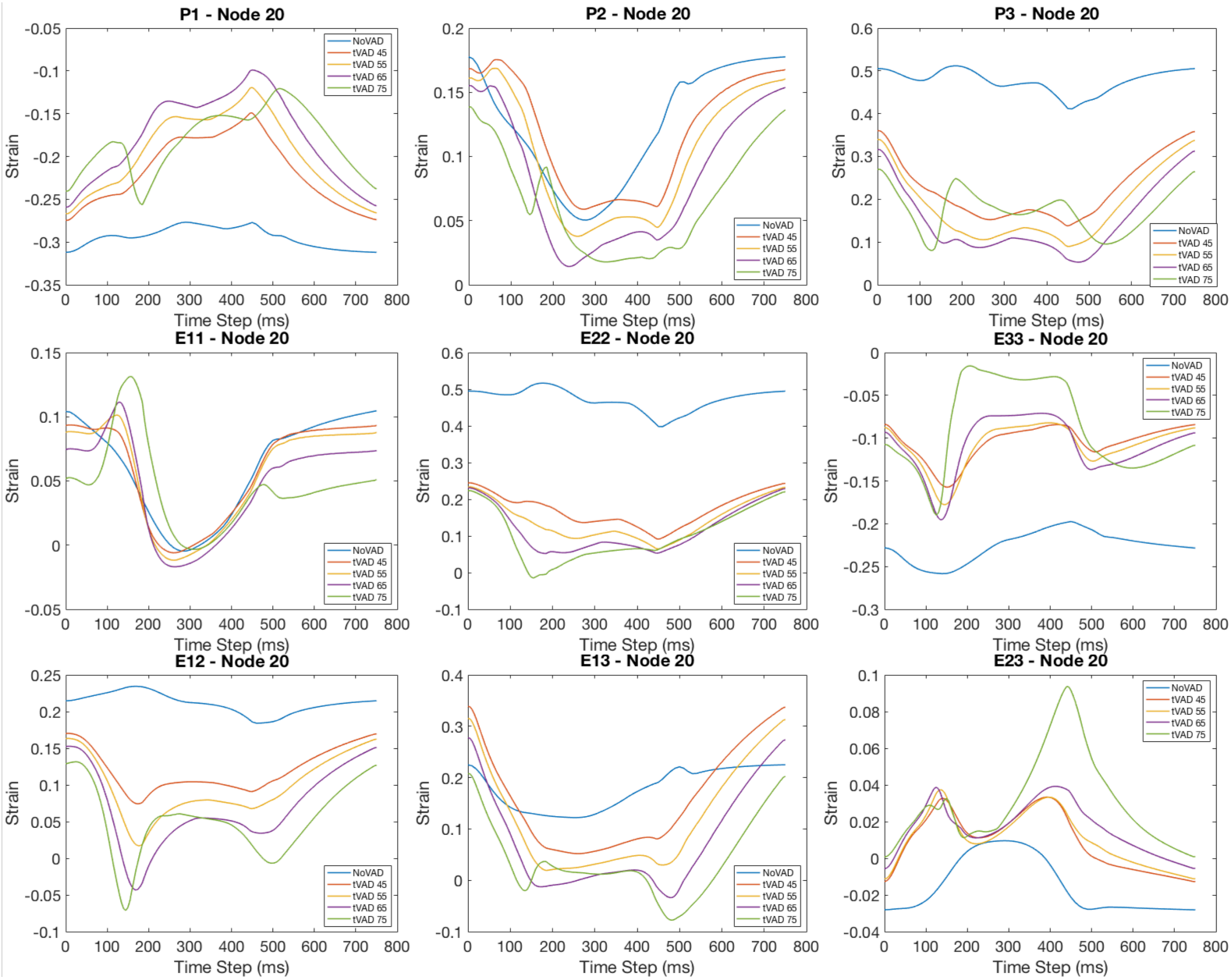

Figure 28: Component strains for the endocardial node at the anterior septal wall of the ventricular base (Node 20).

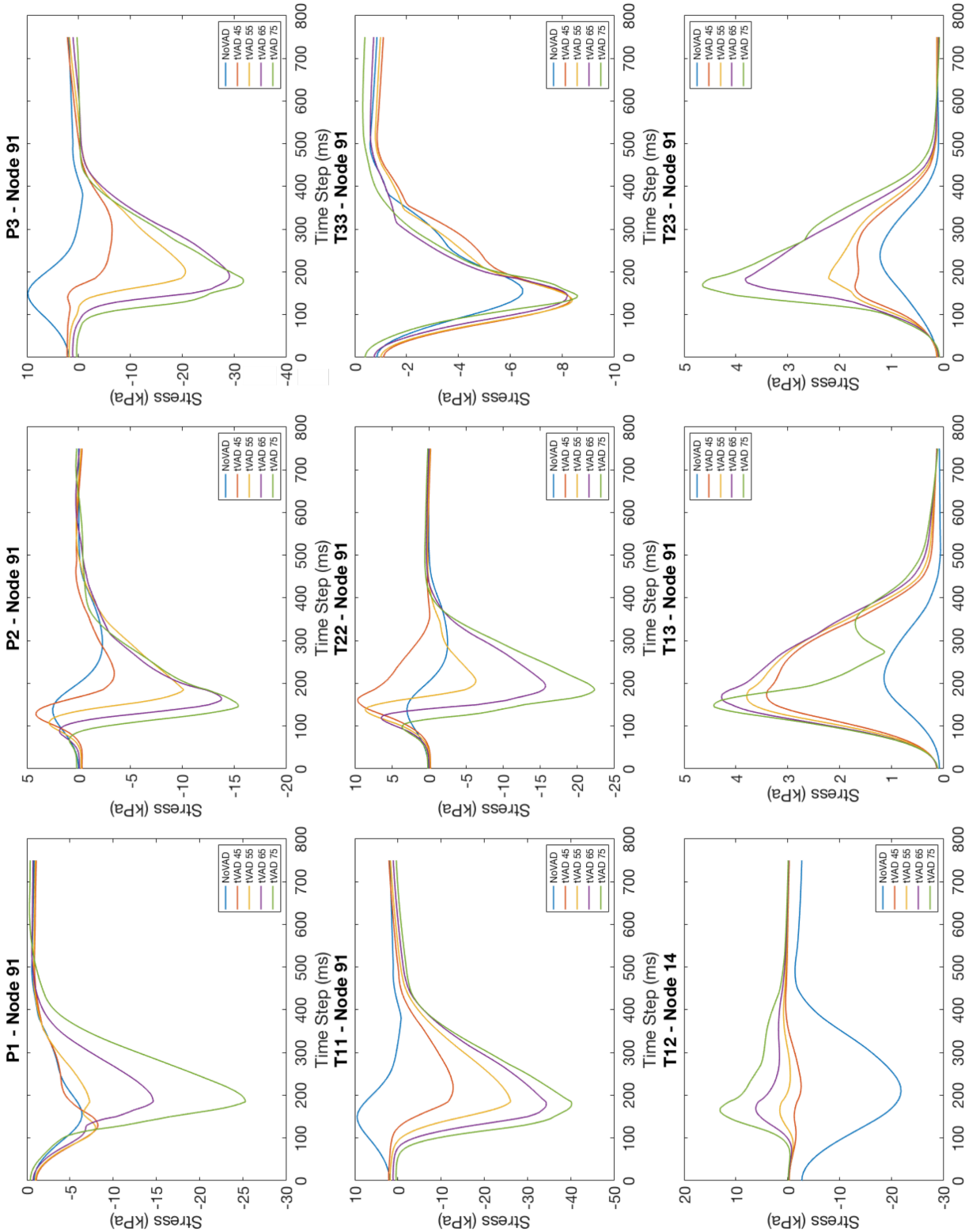

Figure 29: Component stresses (kPa) for the endocardial node at the RV free wall of the tVAD base (Node 91).

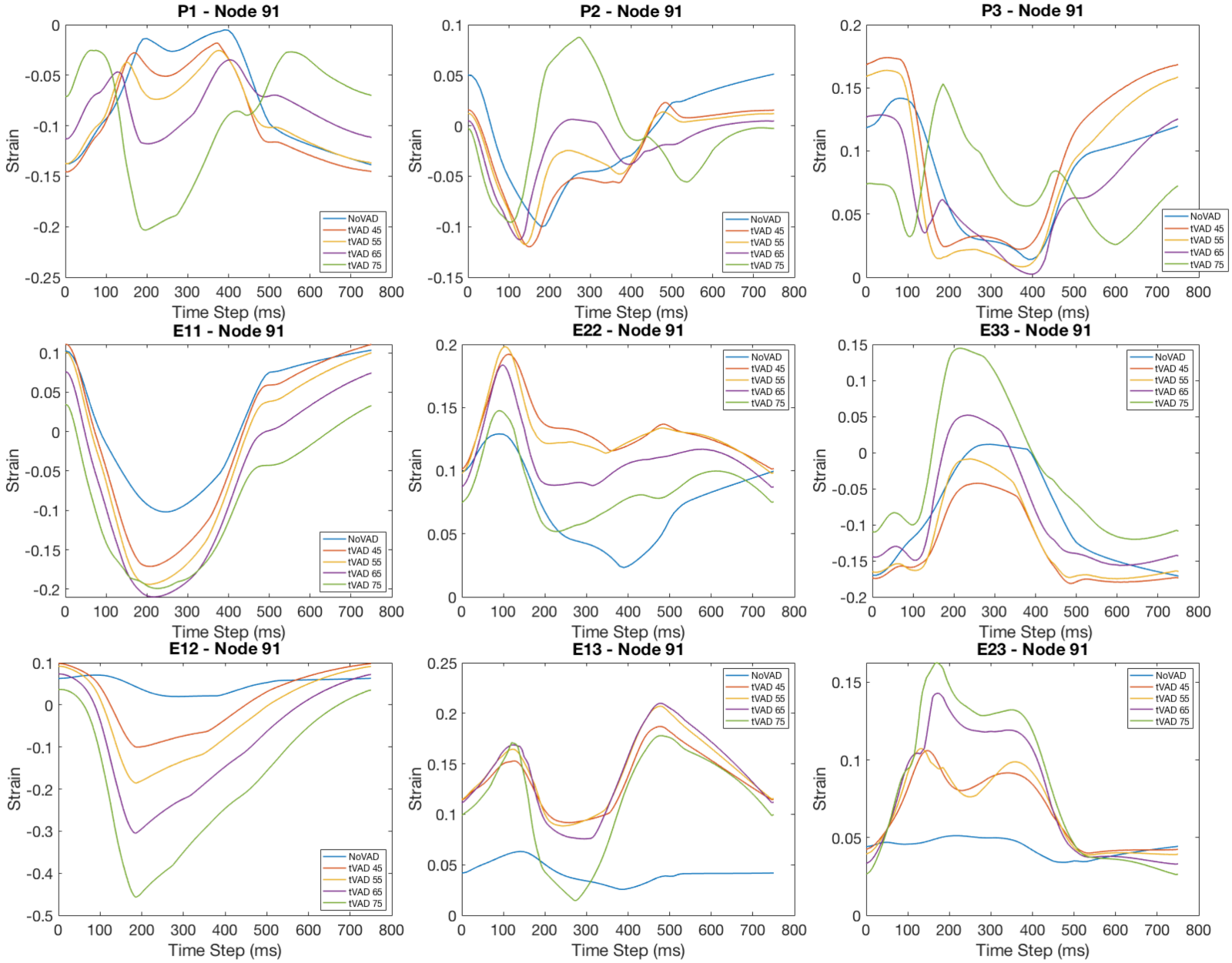

Figure 30: Component strains for the endocardial node at the RV free wall of the tVAD base (Node 91).

4.3 Discussion

Here we report results obtained by varying peak apical rotation angles in simulated beating hearts in order to understand how regional cardiac biomechanics are likely to be affected by mechanical torsion imposed by a device attached to the surface of the heart. Based on these simulations, we determined that with increasing levels of rotation we are applying very large deformations to the myocardium. In general, the epicardial nodes, regardless of their location around the base of the ventricles or along the upper border of the tVAD, tended to have similar trends in estimated strains and stresses within the myocardium that are consistent with the application of rotation during systole and subsequent return to the original, end-diastolic state (Figure 22, top). Furthermore, the epicardial nodes typically demonstrated an increase in absolute maximum P3 strains and stresses with increasing levels of AAT (Tables 15 and 16). The endocardial regions also generally had strains and stresses that follow similar trends as the epicardium, where the maximum P3 strains and stresses due to the applied torsion over time are similar to one another but do not necessarily follow the behavior of the baseline HF model (Figure 22, bottom). However, the endocardium also had nodes where the resulting maximum P3 strains decreased while P3 stresses increased with increasing levels of AAT (Tables 15 and 16). As described at the beginning of the results, the case of a peak rotation of 75 degrees was omitted due to a lack of convergence, i.e., although the convergence criterion was met for global hemodynamics for this case and all others, the finite elements did not always remain isochoric for the 75-degree case.

The node of the endocardial anterior septal wall at the ventricular base (N20) saw decreasing levels of the maximum principal stresses as increasing levels of torsion were applied when compared to the baseline HF model (Figure 27). Upon evaluating the components of the

principal strains and stresses, it was determined that the components contributing the most to the principal strains and stresses of the baseline HF model differ from those of the applied torsion therapy. The maximum P3 stresses of the baseline HF model are determined by the T22 normal stresses. However, for the cases of applied torsion, it seems that the peak stresses are mostly determined by the T11 stresses at the node. Similarly when evaluating the strains at node 20, the maximum P3 strains decreased with increasing levels of torsion and were overall lower than the P3 strains in the HF model. The P3 strains in the HF model were dominated by the E22 normal strains, while the AAT case were dominated by the fiber-transmural shear strain (E13) component (Figure 28). Though the P3 strains trended similar to other endocardial nodes, the large decrease in P3 stresses with increasing torsion did not. This combined with the fact that the P3 stresses and strains are much lower than that of the HF case, suggests that there maybe some sort of warping of the tissue, which could lead to valve regurgitation due to the location of this node at the anterior septal wall of the base of the ventricular endocardium.

The P3 stresses at the endocardial node of the RV free wall at the device base (N91) trend similar to one another for the tVAD simulations, and differ only from the HF case (Figure 29). Despite this, the P3 stresses for both the HF model and tVAD simulations were dominated by the T11 normal stress. The P3 strain for the HF model is dominated by the E22 normal strain (Figure 30). However, it was much harder to determine the dominating component for the P3 strains of the AAT cases, especially at 65 degrees. Based on comparisons between the component waveform magnitudes and trajectories over the cardiac cycle, the best estimation would be that P3 strains for the AAT cases are dominated by E13 shear strain. Based on the component analysis, as torsion was increased, both the P3 strains and stresses decreased. It was also observed that decreases in P3 strains were not very large, but the change in P3 stresses

between the 45 degree case to the 55 degree case was large. This suggests that at this location, increases of ARA beyond 55 degrees could potentially be causing excessing shearing to the tissue and damaging the myocardium with such warping.

4.4 Implications for Applied Apical Torsion as a Means for Cardiac Assist

4.4.1 Significance of Study Findings

Based on the results of these simulations, it appears that AAT alone may not be a viable method of cardiac assist due to the large deformations that result in very high strains and stresses in the myocardium. Although previous results demonstrated that applied torsion could potentially improve cardiac hemodynamics substantially, these resulting regional cardiac biomechanics suggest that it would come at the potential cost of damaging the myocardium. The rendered P3 strains for the 65 degree simulation revealed large regions of super-physiologic strains across the myocardium (Figure 24). Additionally, it was observed that even with a lower level of applied torsion at 45 degrees, regions of the myocardium experienced P3 stresses above 100 kPa and P3 strains above 0.60 (Tables 15 and 16). The maximum principal strain observed in the baseline HF model was at node 14 with a finite strain of 0.562 or a principal stretch of 46%. Though not conclusive, these large strain values strongly suggest that repeated application of such high levels of torsion may cause damage to the myocardium over the long term. Similarly for the stresses, there are large changes in maximum principal stresses throughout various locations within both ventricles, and when visualized through the P3 stress rendering for the 65 degree case, localized regions of very high P3 stresses were observed (Figure 26). Of especial concern are the regions of localized high stress at the ventricular base. Although this specific ventricular model did not include the anatomy of the heart valves, it is hard to argue that such high stresses and strains

would not affect the physiologic mechanics of the heart valves or potentially contribute to valvular regurgitation.

Though it may not be realistic to utilize such supra-physiological rotations for cardiac assist, it would be reasonable to utilize AAT coupled with external compression of the ventricle. As mentioned before, the absence of native left ventricular rotation leads to an increase in myocardial stress and strain, which leads to a decrease in ventricular efficiency, and subsequently a reduction in ejection fraction. Therefore theoretically, reintroducing the left ventricular torsion to native physiological levels of 10-15 degrees of net rotation should help to restore a more uniform fiber stress and strain distribution in the myocardium. This in tandem with direct cardiac compression could provide adequate improvements to cardiac hemodynamics.

4.4.2 Study Limitations

Although these results provide important insights into the potential effects of AAT on regional heart wall mechanics, there are limitations to our model. Currently, our computational model exists as a bi-ventricular representation of the beating heart where the base of the model lies just below the valvular plane and excludes the rest of the cardiac anatomy, i.e., both atria, the heart valves, cardiac skeleton, chordae tendineae, and papillary muscles. This lack of anatomy coupled with the boundary conditions of the model reinforces that the results of the parametric simulations at the ventricular base are approximations at best. A more detailed computational model of the heart that includes the rest of the cardiac anatomy and their respective biomechanical properties would provide more realistic results. Moreover, to avoid very long simulations, the total number of high-order finite elements is relatively small. Although the tri-cubic Hermite interpolation makes the smaller number of elements viable, it also contributes to

the strain and stress concentrations, particularly at the ventricular base. So, the strain and stress concentrations there are very conservative and probably larger than would occur with many more elements and nodes. Nevertheless, we believe that even more distributed strains and stresses would still be quite large for larger peak rotations. Also, although we currently are able to compare the subsequent regional biomechanics for our parametric simulations, we are limited to comparing tVAD cardiac assist with a patient-specific HF model. To the best of our knowledge, there exist no patient specific healthy heart computational models that can be used for comparison, which would provide important information regarding the stress/strain profiles of normal myocardium and help determine whether and to what extent AAT may be used to restore native contractile motion to diseased hearts. Lastly, although large levels of AAT alone may not prove to be a viable form of cardiac assist, a thorough investigation on the effects of AAT used in tandem with direct cardiac compression on global hemodynamics and regional wall mechanics should be conducted to further evaluate the utility of AAT as a therapy.

Chapter 5

Further Evaluation of the Effects of tVAD for Cardiac Assist

In the previous chapters, computational simulations of the effects of tVAD assist were evaluated for the design parameters of device CA and ARA. However, additional parameters for the device design and operation should also be assessed. For example, during the operation of a cardiac assist device, the timing of the therapy is an important consideration. Ideally for the tVAD, the rotation should be applied with the onset of systole, with maximum rotation applied at peak systole, which would best mimic the native left ventricular twisting motion. However, it would be beneficial to understand how varying the timing at which the AAT is applied would affect cardiac hemodynamics. Additionally, the results of the parametric computational studies in Chapter 3 suggested that the increased hemodynamic effects of AAT could potentially be further improved by extending the time by which the torsion is applied. In this chapter, two additional timing schemes for AAT are evaluated.

Furthermore, the development of a patient-specific computational model for parametric studies has proven to be a very useful and important tool to better predict the effects of cardiac assist devices on the heart. However, ideally, the computational workflow established in Chapters 2 and 3 could also be used to evaluate the effectiveness of AAT on various types of heart failure, such as patients with different INTERMACS profiles [16], or different disease

states that contribute to HF such ischemia, pulmonary hypertension, hypertrophy, etc. [1,16]. The long-term goal of this work would be to determine which subset of end stage heart failure patients would benefit most from this device. In that vein, a first attempt was undertaken whereby the existing bi-ventricular model of a dilated cardiomyopathy patient was modified to create a new heart model in more severe heart failure.

5.1 Parametric Timing Studies

5.1.1 Materials and Methods

The goal of these timing studies was to determine optimum timing parameters for tVAD actuation. In all of our previous computational simulations described in Chapters 2 and 3, the AAT was applied with the onset of systole in a sinusoidal stepwise method up to PT of 187.5 msec, at which point the maximum rotation angle was applied. After, the heart is rotated back to its starting point in a linear stepwise manner for the remainder of the cardiac cycle. Based on the resulting PV Loops of the parametric computational simulations in Chapter 3, it was noted that with this PT of 187.5 msec and with higher ARA, the ejection of blood appears to end substantially earlier than the start of isovolumic relaxation. As such, two additional timing schemes were evaluated in an effort to determine optimal timing for rotation mechanics.

To do this, additional lines of logic were added to the existing Python script such that the peak time for the cardiac cycle was varied from the original PT of 187.5 msec in one of two ways: 1) the ventricle was rotated to PT in a sinusoidal stepwise method, which was set to another later time point in the cardiac cycle such as 247.5 msec, 287.5 msec, and 387.5 msec, and then returned linearly to its initial position thereafter; and 2) the ventricle was rotated to the original PT of 187.5 msec in the sinusoidal stepwise method, then the ventricle was held for either 50 msec, 100 msec, or 200 msec before being returned to its initial position over the

remainder of the cardiac cycle (Appendix B). In order to facilitate the convergence of our computational simulations, the timing simulations utilized the 18-element, high-order computational model of the beating left ventricle based on clinical measurements of a severe heart failure (HF) patient from Chapter 2. In each of these simulations, the maximum applied rotation angle was 75 degrees. The same computational workflow from Chapter 2 was used in this set of experiments and the resulting cardiovascular hemodynamics for each simulation were then collated and compared with the original 75 degree 18-element model simulations. However, SW calculations were amended based on the newer method of calculation as described in Chapter 3.

5.1.2 Results of Parametric Timing Studies

In this parametric study for the timing of tVAD actuation, the effects of varying the timing of the applied torsion on hemodynamics were evaluated. In our first set of simulations, we prescribed a new set PT at 50, 100 and 200 msec above the original PT of 187.5 msec and saw that with later PT at which maximum rotation would be applied, there was an initial increase in hemodynamic return for PT at 237.5 msec, but for subsequent test cases, there was a decrease in the EF and SW when compared to the original PT setting (Figure 31, Table 17). In our second set of simulations, the heart was rotated to its maximum angle at the original PT of 187.5 msec, but was then held in that position for an additional 50, 100 and 200 msec before returning to its untwisted state. With increasing delayed return to an untwisted state, there was an increase in the hemodynamic returns, with an increase in EF, PSP, and SW and a decrease in ESV (Figure 32, Table 17).

Table 17: Resulting hemodynamics from rotation studies for parametric timing studies done for a patient-specific single left ventricular model.

Timing (msec)	*EF (%)*	*PSP (mmHg)*	*ESV (mL)*	*SW (mmHg*mL)*
Original PT				
187.5	18.12	158.5	144.2	4526
New PT				
PT at 237.5	19.06	167.7	141.2	4917
PT at 287.5	18.68	161.2	141.0	4595
PT at 387.5	15.64	132.1	145.0	3149
Original PT Plus Hold to Time				
Hold for 50	19.73	169.0	139.2	5179
Hold for 100	20.52	170.9	135.7	5379
Hold for 200	21.74	171.9	128.0	5505

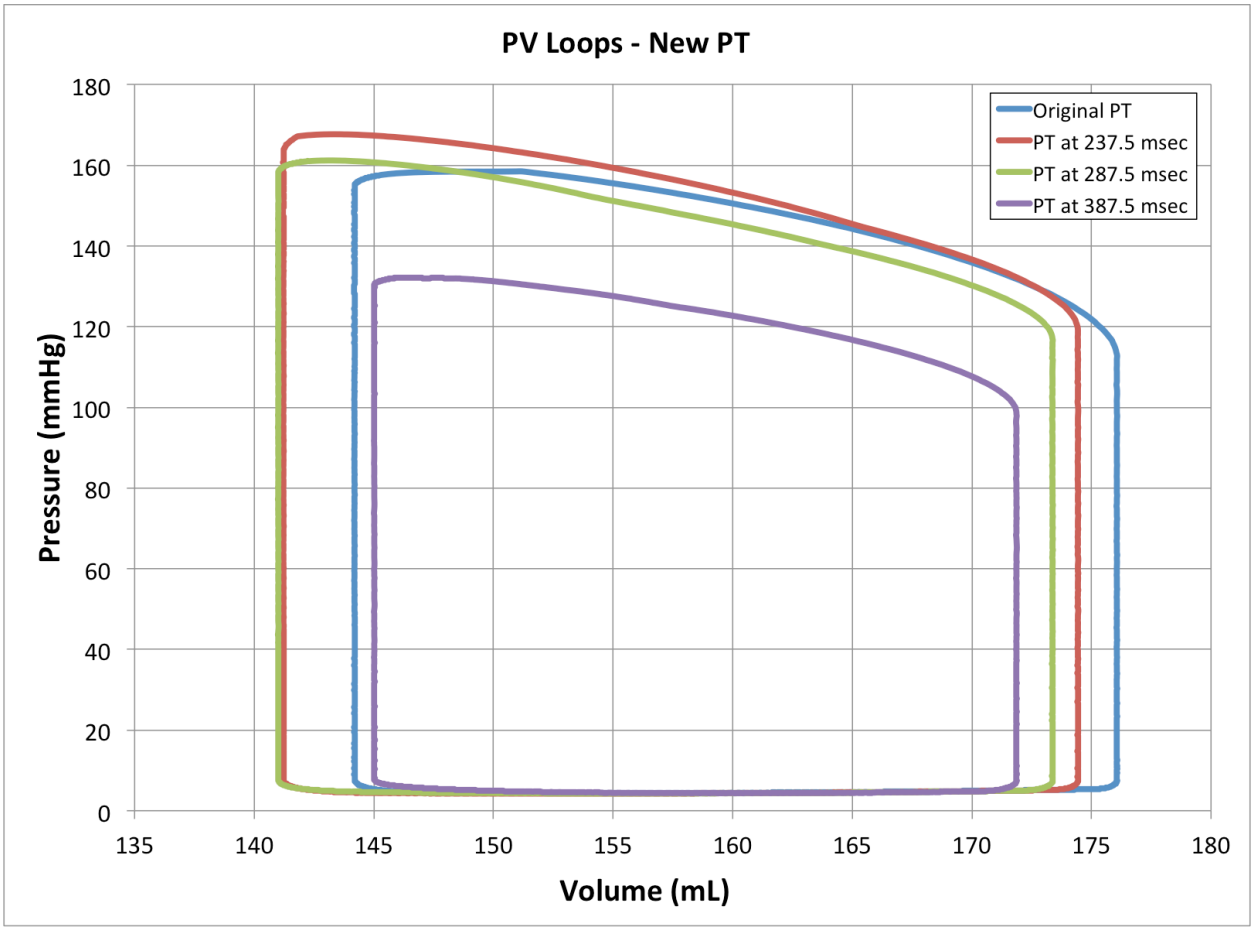

Figure 31: Resulting PV Loops from parametric timing studies where a new, later time point PT was selected for a patient-specific single left ventricular model.

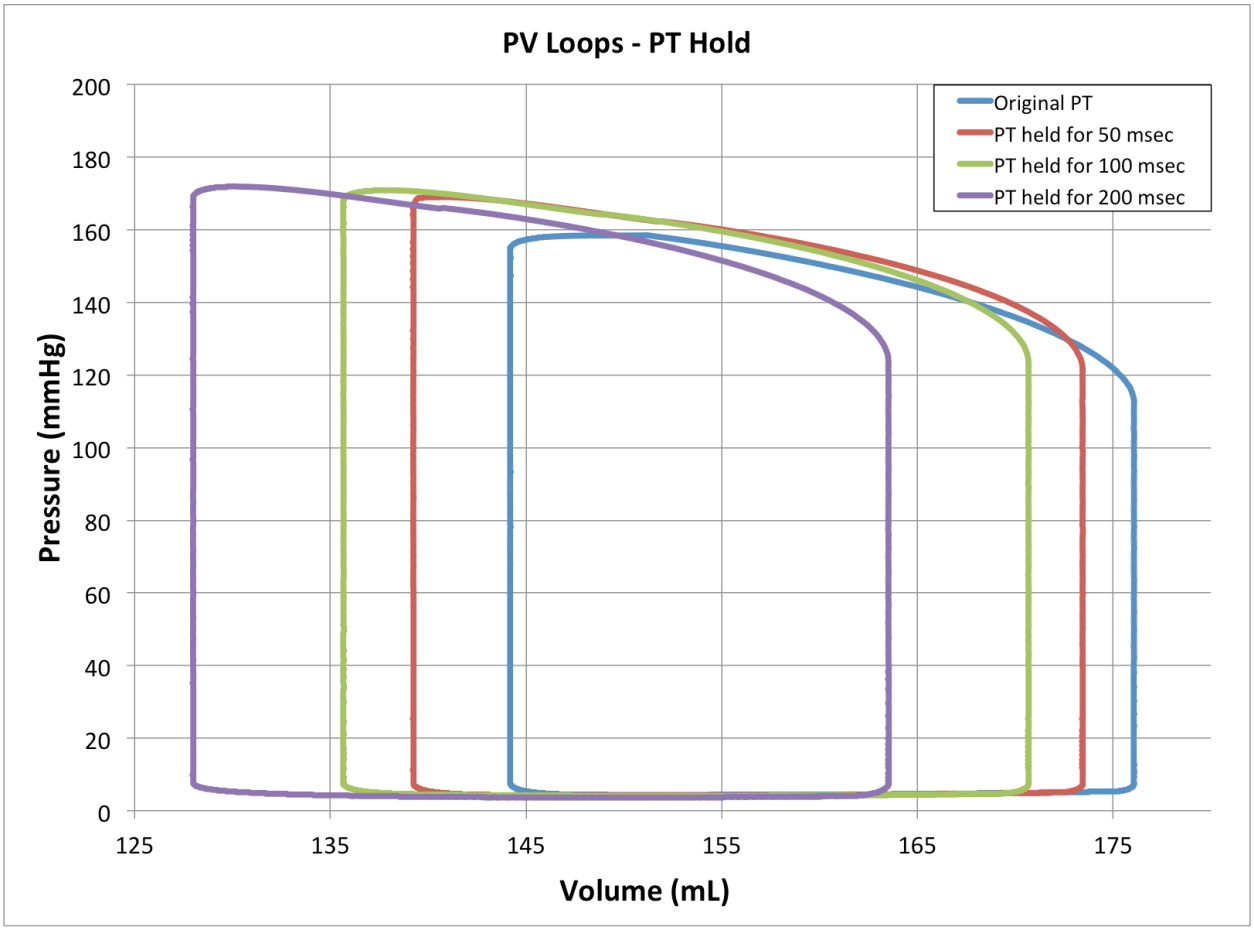

Figure 32: Resulting PV Loops from parametric timing studies where the heart was rotated to the original PT of 187.5 msec, and then held to the specific time before being returned for a patient-specific single left ventricular model.

5.2 Development of a New Patient-Specific Model

5.2.1 Materials and Methods

This section describes the development of a new patient model for computational simulations. In this set of experiments, the 80-element bi-ventricular model described in Chapter 3 was used a new dilated cardiomyopathy bi-ventricular model with a lower EF of 15%. All initial boundary conditions, passive properties of the model, circulatory model were the same. The cellular model is the same Hill-type model with length dependent activation as presented in Chapter 3, but the maximum isometric tension at the longest sarcomere length was modified, as seem in Table 18. Using the same workflow as described in Chapters 2 and 3, the new NoVAD HF EF15% model was run to convergence, forming the basis for the subsequent AAT simulations.

Table 18: Parameters of the cellular model for the EF 15% bi-ventricular model

Dynamic Cellular Model	**Parameters**
Unloaded Sarcomere Length (microns)	1.95
Active Stress Scaling Parameter (kPa)	0.95
Intracellular Calcium Concentration (micromole/l)	4.35
Maximum Isometric Tension (kPa) at Longest Sarcomere Length	70.00
Length-Dependent Calcium Sensitivity Constant (kPa)	1.80
Sarcomere Length at which Active Force is Zero (micron)	1.58
Maximum Peak Intracellular Calcium Concentration (micromole/ml)	4.35
Hill Coefficient in Calcium Sensitivity	2.00
Slope of Relation between Time-to-Peak Tension and Sarcomere Length (ms/micron)	52.49
Intercept of Relation between Time-to-Peak Tension and Sarcomere Length (ms)	55.26
Slope of Relation between Relaxation Duration and Sarcomere Length (ms/micron)	131.20
Intercept of Relation between Relaxation Duration and Sarcomere Length (ms)	-94.34
Twitch Duration Scaling Factor	1.4625
Cardiac Cycle Duration (ms)	750.00

For AAT on this new NoVAD HF EF 15% model, the device coverage area was held at the large device coverage area of 24% up the ventricular longitude, and applied angles of rotation

were varied for 45, 55, and 65 degrees. Cardiovascular hemodynamics of both the left and right ventricles for the NoVAD EF 15% simulation and each of the AAT EF 15% simulations were then collated and compared per the methods of Chapter 3.

5.2.2 Results

This set of simulations demonstrated that this new NoVAD HF model with an EF of 15% could also be used for parametric computational simulations. Based on the results of these computational simulations, it was demonstrated we created a NoVAD HF model with a reduced LV EF of 15% and SW of 3099 mmHg*mL (Table 19) and RV EF of 32% and SW of 1431 mmHg*mL (Table 20). Based on our simulations varying the levels of AAT assist, we observed that increasing applied rotation angles resulted in the PV loops for both the left and right ventricles became larger overall (Figures 33 and 34). This was supported by the increases in SW with increasing levels of ARA, when compared to the NoVAD HF model. Furthermore, the PV loops widened and shifted leftwards with increasing ARA, which suggests that the ventricle is emptying more completely. This is further supported by the decreasing ESV with increasing ARA for both ventricles (Tables 19 and 20).

Table 19: Resulting left ventricular hemodynamics from rotation studies for the baseline heart failure case (No VAD) and 24% device coverage areas.

	Angle (°)	***EF (%)***	***PSP (mmHg)***	***ESV (mL)***	***SW (mmHg*mL)***
No VAD		14.98	100.6	229.1	3099
24% Coverage	***45°***	17.56	112.3	211.1	4056
	55°	19.85	123.3	202.15	4987
	65°	22.40	141.5	188.92	6386

Table 20: Resulting right ventricular hemodynamics from rotation studies for the baseline heart failure case (No VAD) and 24% device coverage areas.

	Angle (°)	*EF (%)*	*PSP (mmHg)*	*ESV (mL)*	*SW (mmHg*mL)*
No VAD		31.96	44.54	89.57	1431
24% Coverage	***45°***	36.51	45.56	79.08	1562
	55°	39.57	49.19	72.84	1795
	65°	49.68	52.71	52.70	2167

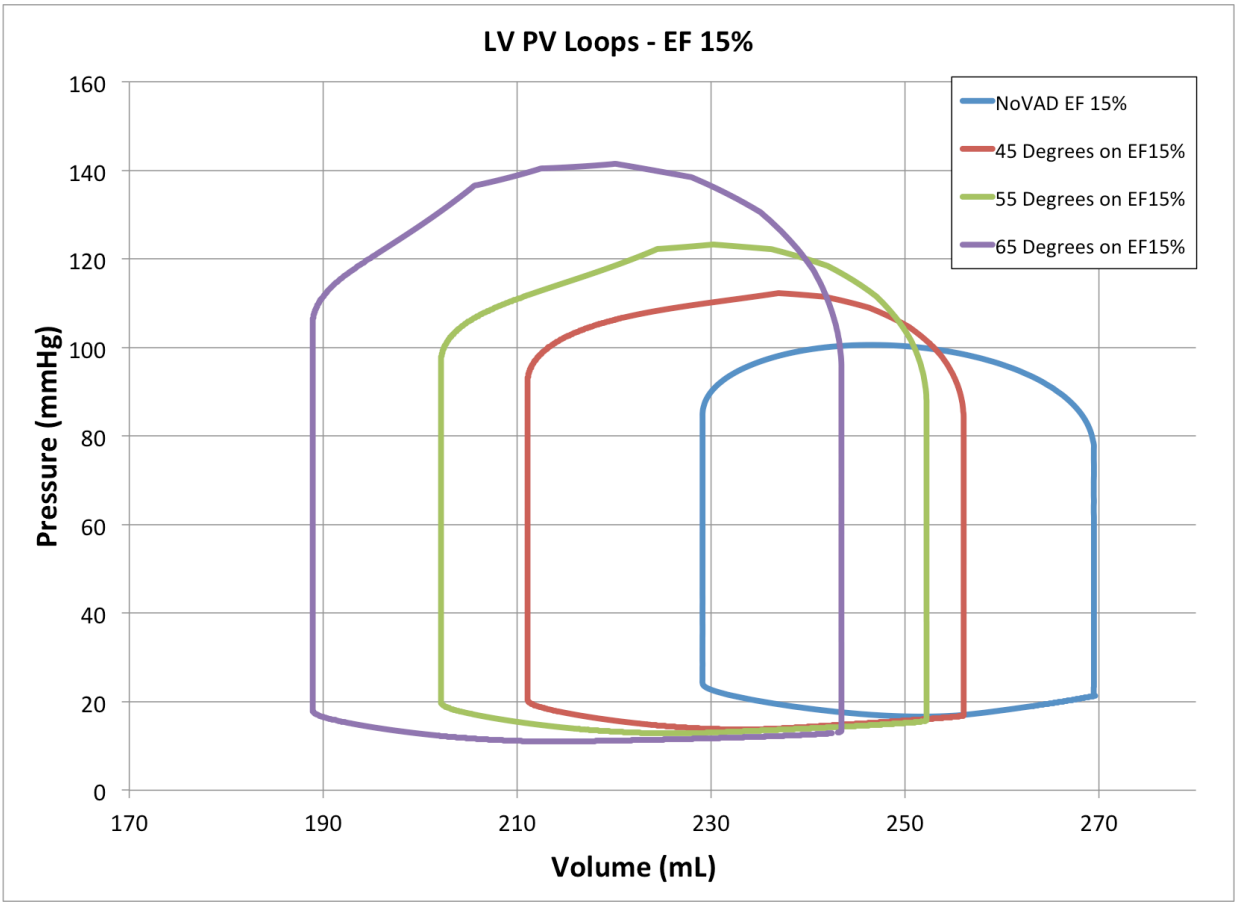

Figure 33: Resulting LV PV Loops for the computational study of the effects of applied rotation angle on a heart failure model with EF 15%

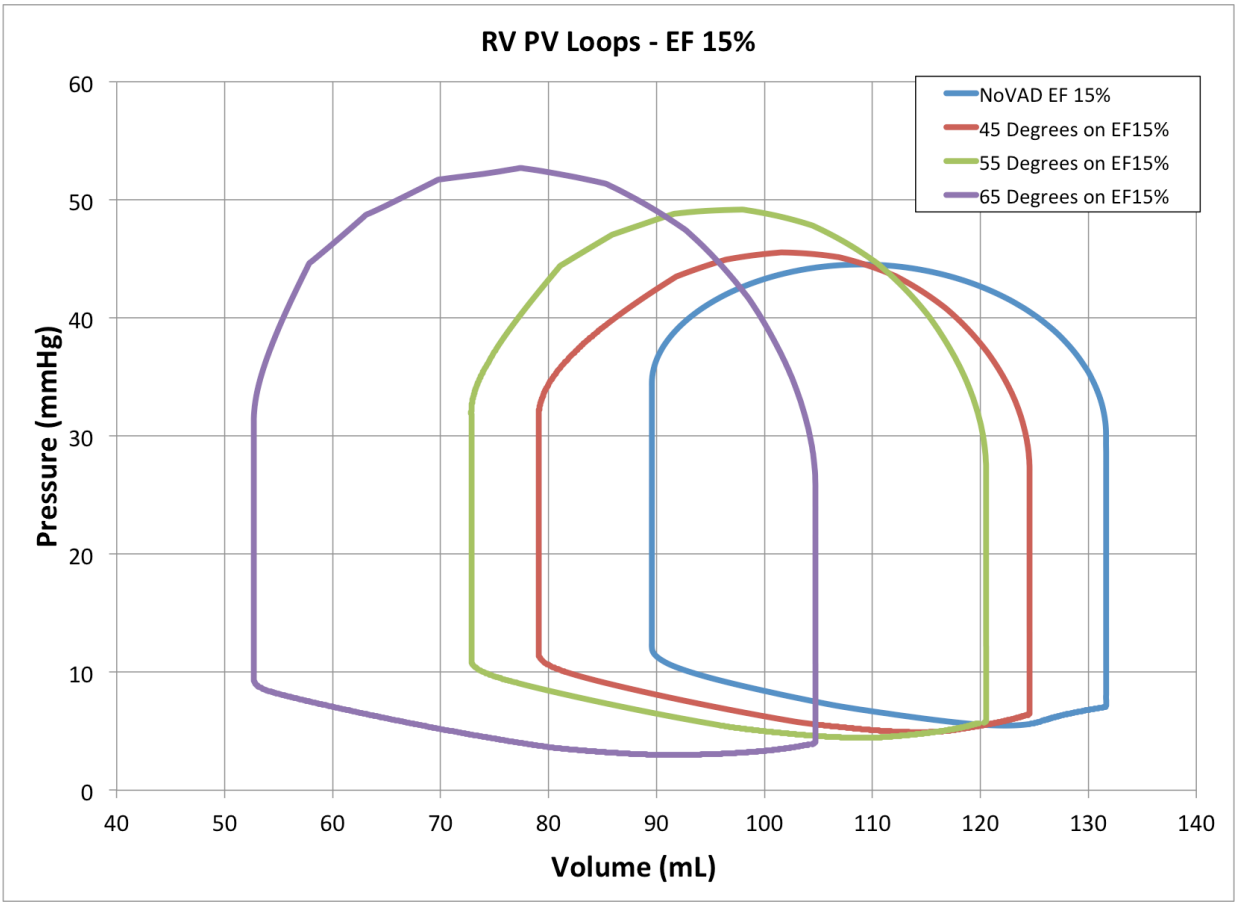

Figure 34: Resulting RV PV Loops for the computational study of the effects of applied rotation angle on a heart failure model with EF 15%

5.3 Discussion

The work done on determining optimal timing for tVAD actuation suggests that although there may be a slight improvement by changing the original PT of 187.5 msec by 50 msec, changing PT to a time point beyond 50 msec does not appear to provide added hemodynamic improvement. However, applying the original PT of 187.5 msec and then holding the heart in that maximum rotated angle for a prescribed amount of time – 50, 100, or 200 msec – appears to benefit hemodynamic performance. This confirms that timing of AAT is also an important parameter to consider for the design of the tVAD. Looking forward, this study should be

repeated in the bi-ventricular HF model to understand how such timing schemes may affect bi-ventricular hemodynamics.

The new EF 15% bi-ventricular model reaffirms that AAT has the ability to improve cardiovascular hemodynamics with varying levels of tVAD assist. More importantly though is the fact that the new EF 15% bi-ventricular model demonstrates the ability to create new heart models of different diseased states. Surprisingly, changing a single model parameter had the effect of reducing EF. The ability to test the effectiveness of multiple parameters for the effects of a potential medical device is especially useful when coupled with the ability to generate patient-specific heart models with various disease pathologies, such as hypertrophic cardiomyopathies or pulmonary hypertension. Future work should invest in creating additional models with patient profiles of varying levels of HF and different disease pathologies that commonly require cardiac assist.

Chapter 6

Prototype of a Torsional Ventricular Assist Device

Previously, a first generation tVAD was created from a commercial surgical device (Urchin Evo Heart Position, Medtronic, Inc.), which was attached to the apex of the heart by vacuum suction and actuated with a rotary servomotor [25]. Although in vitro and in vivo experiments with this device yielded promising information about the effects of AAT on cardiac hemodynamics, the goal of the parametric computational simulations described previously was to determine design parameters for a second-generation tVAD. Some of the design parameters determined from the computational studies described in the previous chapters are, but are not limited to, the coverage area of the device over the epicardial surface (i.e., how far the fingers of the claw will be extending up the epicardium from the apex of the heart), the amount of applied rotation, the timing of the rotation (i.e., how quickly is the rotation applied), and the direction of applied rotation. Parallel to the computational parametric simulations, an initial design for a second-generation tVAD that consists of the glove interface, claw actuator, and deployment handle that will be actuated by a separate rotary motor system was created (Figure 35).

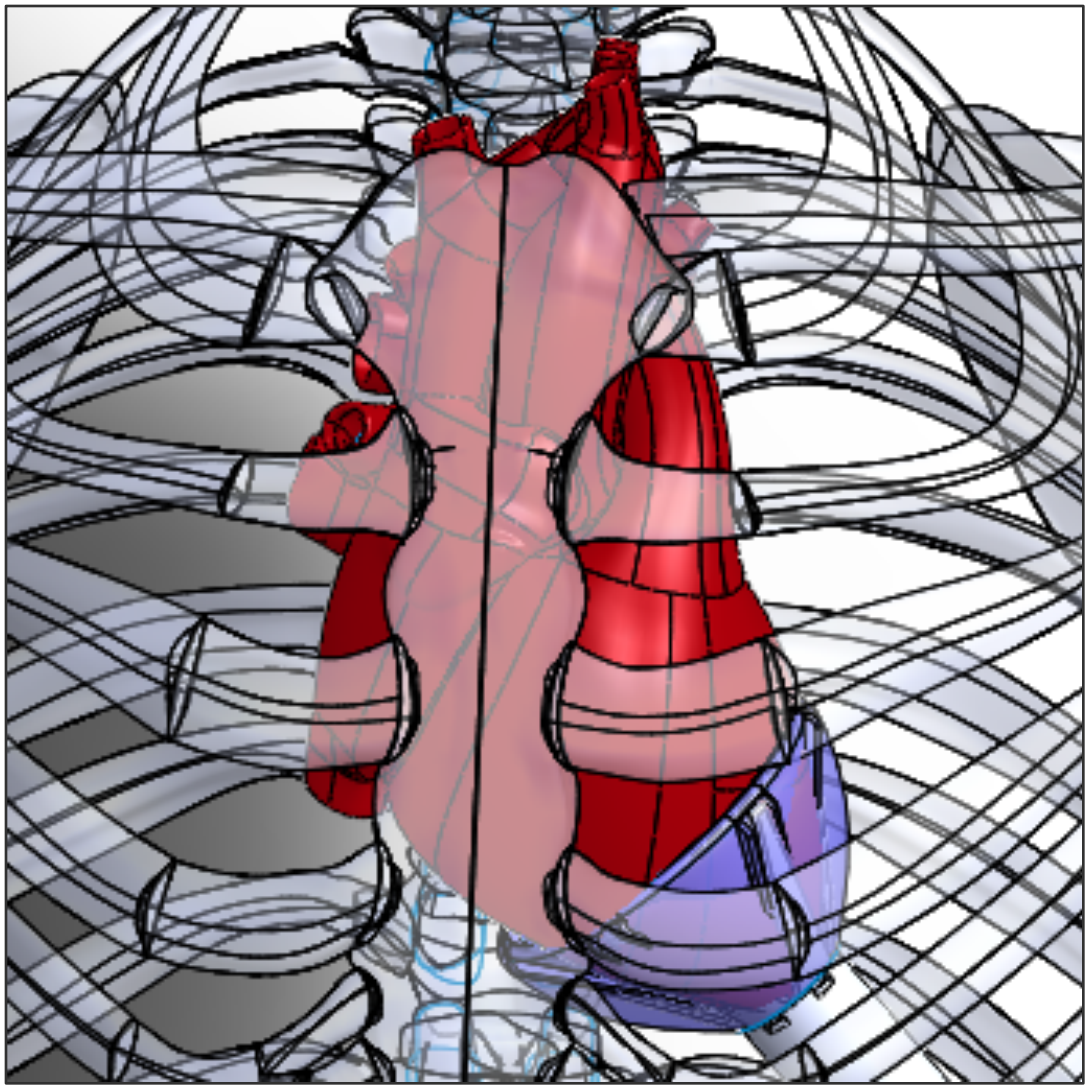

Figure 35: Solidworks rendering of the second-generation tVAD prototype attached to the apex of the heart.

6.1 Device Components

We created our prototype design (Figure 36) using the CAD software package Solidworks 2015 (Dassault Systèmes Solidworks Corp., Waltham MA). In our development of the tVAD prototype, we sought to create a device that would avoid blood contact, allow for rapid deployment through a small incision, and be simple to remove. With those three goals in mind, we developed a tVAD prototype that consists of three main components: a flexible mesh interface, a "claw" actuator mechanism, and a transcostal deployment system. The tVAD

approach lends itself to minimally invasive placement across the chest wall, thus we designed the device for deployment via a mini-thoracotomy. Although this approach can, in principle, be used to provide both short and long-term care, our initial design will focus on the development of the tVAD for use as an acute therapy. In the following section, we describe each of the main system components in order of their direct interface and/or interaction with the heart. The tVAD prototype consists of three main parts: a flexible cup interface, a mechanical claw actuator, and a handle for manual insertion and deployment. The device actuation would be with a rotary servomotor.

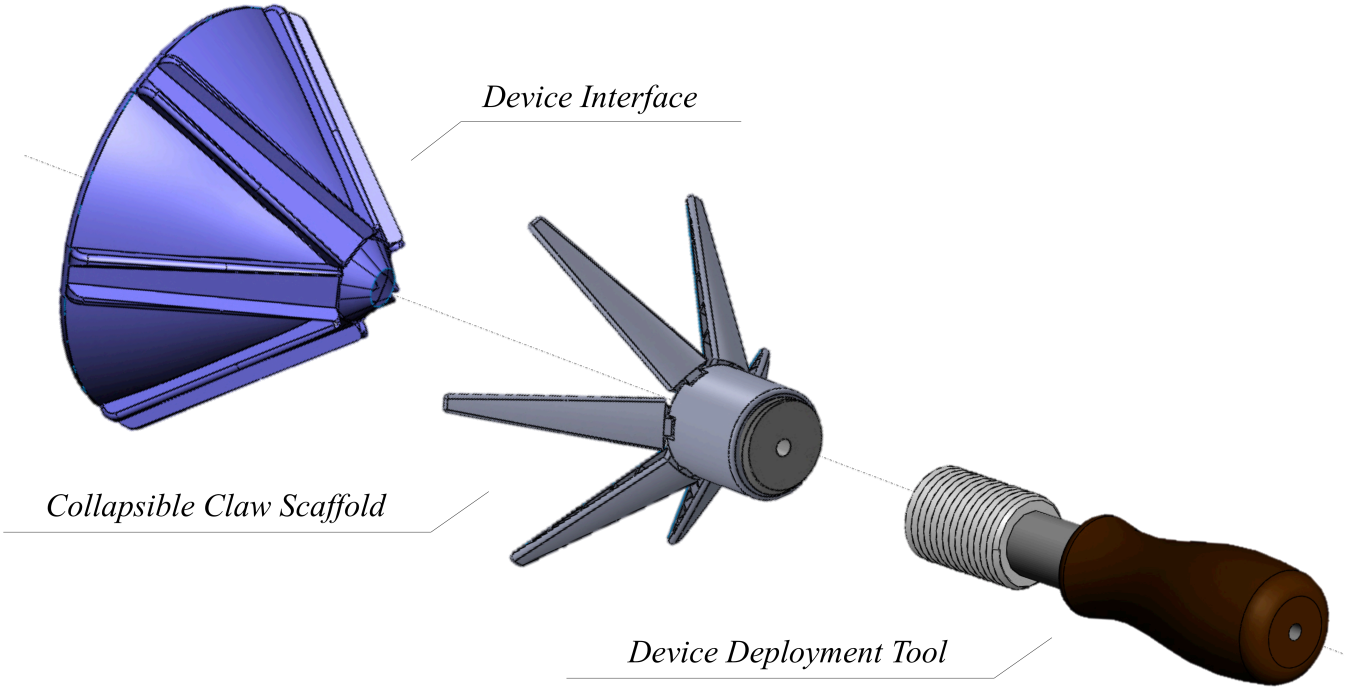

Figure 36. Exploded view of proposed tVAD prototype components featuring (from left to right): device interface, claw scaffold, and deployment tool.

6.1.1 Device Interface

The flexible cup interface (Figure 37) is glove-like, in that it holds the "fingers" of the claw in place while providing a smooth protective layer both at the epicardial interface and the outside (pericardial-facing) surface. On the cardiac side, the cup interface spreads the distribution

of the applied torsional forces evenly across the heart surface, minimizing the risk of tissue damage. The pericardial side serves to shield surrounding tissues from abrasion as the external actuator motor rotates the claw. Because of its glove-like design, a clinician can easily explant the device by simply sliding the claw and its fingers out of the cup's inner pocket. Ideally, the material should be something that can be easily interfaced with the epicardium. We would want the cup to be made of a biocompatible and flexible material, such as a polymer such as silicone or coated nitinol, patterned as a mesh net. Indeed, a number of other epicardial cardiac assist devices are made of one or a combination of those materials [25-27].

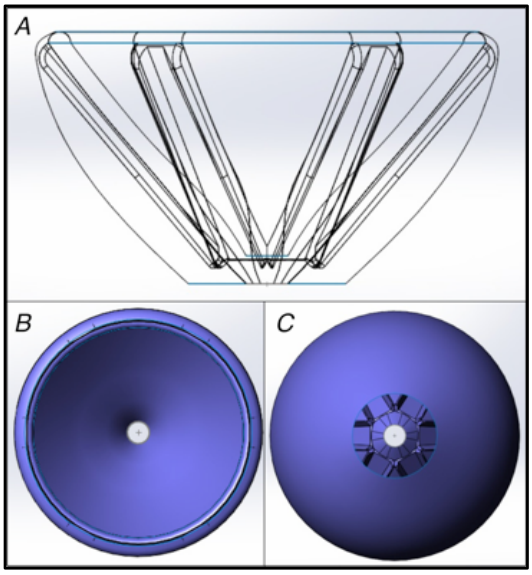

Figure 37: Glove-like flexible cup interface that features an inner pocket a) with webbing for claw segments to fit between smooth epicardial b) and pericardial c) surface interfaces to minimalize tissue trauma.

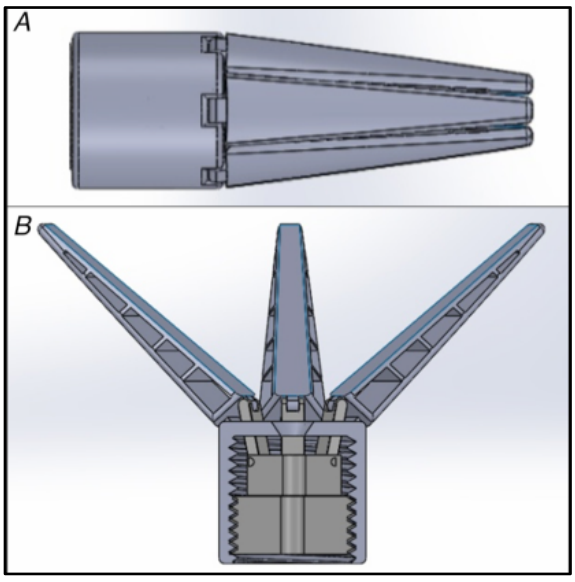

Figure 38: Collapsible claw-like mechanical actuator a) that features a threaded deployment system and b) flexible finger-like truss segments that allow for a snug fit onto the epicardial surface.

6.1.2 Claw Scaffold

The six actuator fingers (Figure 38) fit within the flexible 'glove' and are pre-threaded with sutures that fasten them to the interior webbing of the mesh interface. Should the device need to be explanted, the sutures can be unfastened and removed, allowing the device to freely slide out of the glove's pocket. The entire assembly is collapsible to allow for minimally invasive deployment and removal. When collapsed, the claw is three centimeters in diameter and can be expanded to fit snugly around the apex of the heart.

The interior segments of each truss-like finger will be made less stiff than the exterior segments, thus allowing each finger to flex and conform to the surface of the heart. Possible biocompatible materials to be considered for the actuator include a combination of nitinol for its shape memory qualities and 316L stainless steel or titanium, known for stiffness and resistance to cyclic loading [62]. The flexion of the finger's truss structures could possibly be achieved by either varying the thickness of the material, patterning it so that the material is more flexible, or using a different, more flexible material. The collapsed claw and mesh interface are implanted onto the apex of the heart via the deployment system, which consists of a spring-loaded handle that allows clinicians to carefully twist open the collapsed device and position the claw and mesh onto the beating heart through a small incision.

6.2 Proposed Implantation and Device Actuation

6.2.1 Device Implant and Deployment

Because the tVAD is designed to sit on the epicardium, it lends itself to a minimally invasive implant through a mini-thoracotomy, where the ribs would be spread to a 2.5in.x2.5in. operating window, which would allow for access to the apex of the heart. The collapsed device, with the claw already pre-inserted into the glove interface, will be connected to a deployment

tool that is connected to the base of the tVAD. As the deployment tool is turned, it will allow for the collapsed device to be opened to fit the diameter of the heart at the apex.

To ensure that the tVAD is securely fixed to the apex of the heart, we plan to first use active suction to position and secure the device to the epicardial surface. Once deployed and correctly positioned, the device will then rely on a surgical adhesive as the final means of adhering the device to the surface of the heart. The interior surface of the cup interface will be pre-coated with the adhesive and the active suction will continue to be applied until the adhesive has had sufficient time to cure and set.

6.2.2 Device Actuation

Device rotation will be driven by a programmable servomotor (SmartMotor model SM2337DT-PLS, Animatics Corp., Santa Clara, CA) which keys into the base of the truss assembly after detachment of the deployment handle. The motor connects to the claw mechanism via a stiff metal driveshaft that traverses a fixed transcostal bushing placed to protect surrounding tissue and provide rotational stability. Rotation dynamics will be programmed to mimic those rotation parameters found to be most effective in computational simulations.

Chapter 7

Determining an Attachment Method for Epicardial MCS Devices

A fundamental part of the tVAD design is the method of device implantation, which will of necessity involve attaching the device to the surface of the heart. This presents a considerable challenge as the epicardial surface of the heart exists in a wet environment and is extremely slippery. Suturing the tVAD directly on to the epicardium would be the most direct approach, but this would inevitably lead to regions of high stress during active torsioning of the heart and likely cause tears in the compromised tissue, especially the typically friable tissue of CHF patients. Using a biocompatible adhesive would be a simple solution, but the vast majority of commercial bioadhesives are intended for wound closures or patching and are simply not strong enough to withstand the amount of shear forces that will be applied during torsional assist. Previously, active suction was used to secure the first generation tVAD prototype to the cardiac apex [25]. Though this proved to be very effective, it would not be prudent to utilize active suction over a period of time extending beyond a few minutes as this could potentially cause lasting damage to the tissue.

For acute cardiac assist, the tVAD will be required to provide sustained cardiac assist for timescales on the order of hours to days. In this case, adhesion strategies would need to emphasize rapid application using mechanical (suction, surface contouring) and/or chemical

agents (bioadhesives) and could not employ secondary anchoring methods involving tissue ingrowth or collagen (scar) formation. For longer-term applications, semi-permanent to permanent methods of attachment involving some type of durable adhesive and/or tissue ingrowth mechanism will need to be developed to compete with the various bridge and destination therapy VADs currently available on the market.

With these specifications in mind, the aim of this work is to develop a strategy for acute attachment of the tVAD to the cardiac apex. While long-term attachment of the tVAD is important, in the interest of time and considering the scope of this thesis project, this aspect of device development focused on the attachment of the tVAD to the heart for acute rescue of cardiac hemodynamics. For an acute care tVAD, a bioadhesive may be sufficient for the intended timescale of hours to days. To investigate this possibility, candidate bioadhesives were identified and qualitatively tested on explanted animal hearts to determine whether the adhesive was viable on the slippery surface of the epicardium. Adhesives that passed this initial test were subject to quantitative shear stress and pull testing to determine the extent to which the adhesive withstood the torsional shearing loads that the tVAD would be applying at the epicardial interface.

7.1 Qualitative Testing

7.1.1 Materials and Methods

In order to better understand the material properties of the candidate adhesives, qualitative experiments were conducted to grossly examine if an adhesive would resist being sheared off the epicardial surface of a lamb heart (Salem's Market, Pittsburgh, PA). Adhesives were applied directly to a material sample of potential device interfaces that was subsequently bonded to the epicardium of the lamb heart (Figure 39). The substrate-adhesive-epicardial

system was allowed to cure for one minute. We then applied a shearing motion onto the material substrate to simulate the potential shearing that the tVAD-adhesive-epicardial system would experience and observed the results.

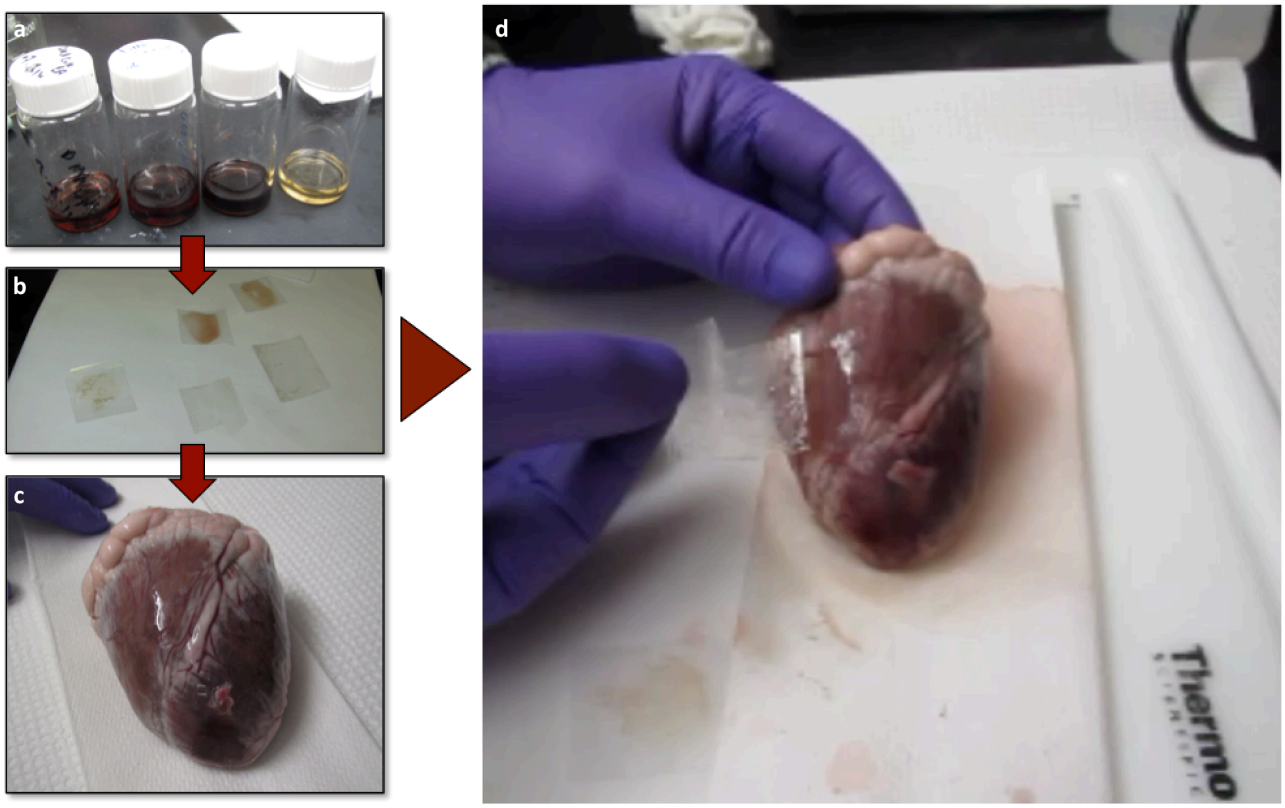

Figure 39: a) Various adhesives are applied onto b) a sample material substrate, which is then placed on the c) epicardium of a lamb heart; d) a shearing motion was then applied to the sample to qualitatively observe if the adhesive would withstand the shearing force.

7.1.2 Results

In our initial qualitative studies, a number of adhesives immediately slipped and sheared the material substrate off of the heart. However, a few adhesives appeared to have potential for the application of maintaining device attachment to the epicardium. Specifically, VetbondTM (3M, St. Paul, MN), GlutureTM (Zoeitis, Parsippany, NJ) and Benzocaine methacrylamide (BenzMA) (Dr. Stefanie Sydlik, Carnegie Mellon University, Pittsburgh, PA) qualitatively appeared to withstand attempts to peel or shear the material-adhesive-epicardium system apart

for potential device materials of stainless steel and silicones [63]. Based on these results, we then proceeded to quantitatively test the material-adhesive-epicardium systems to determine maximum adhesive energies for such interfaces.

7.2 Quantitative Testing

7.2.1 Materials and Methods

7.2.1.1 Determining Adhesive Energy Requirements

Previously, the torque measurements as a function of applied apical rotation at intervals of 10 degrees have been reported [64]. In these experiments, a prototype device was attached to the apex of a passive porcine heart and a silicone model of a heart at peak systole, both with a contact area of 20.4 cm^2. Based on previous computational parametric studies, it has been determined that 75 degrees of applied rotation yields the most hemodynamic return [61]. Therefore, we conservatively selected the 80 degree applied rotation case, which yielded about 11 N-cm and 20 N-cm of torque for the porcine and silicone heart, respectively. In these experiments, the device was directly interfaced to the epicardium via vacuum suction, a completely mechanical coupling. We can assume that the work is done tangent to the surface of the heart in a shearing motion, and that the work applied to the heart is through contact area between the device and epicardium. Based on these assumptions, we calculated adhesion energy requirements to be between 53.9 J/m2 and 98.04 J/m2, and expect the true adhesion energy of the system to lie somewhere between this lower and upper bound (Table 21).

Model	Applied Torque (N-m)	Adhesion Energy(J/m^2)
Porcine Heart (passive)	11	53.92
Silicone Heart (peak systole)	20	98.04

Table 21: Adhesive energy requirements based on an effective contact area of 20.4 cm2 for an applied torsion angle of 80 degrees.

7.2.1.2 Bioadhesive Shear Testing

Based on these initial qualitative experiments, we identified three adhesives – VetbondTM (3M, St. Paul, MN), GlutureTM (Zoeitis, Parsippany, NJ) and Benzocaine methacrylamide (BenzMA) (Dr. Stefanie Sydlik, Carnegie Mellon University, Pittsburgh, PA) – to test [63]. We then repeated the initial experiments quantitatively using ASTM-F2255 – a test protocol for the comparison of tissue adhesives for the purpose of bonding tissue to medical devices – with rectangular material samples to determine lap shear stresses [65]. Samples were prepared by adhering the epicardium of lamb hearts to different device materials – stainless steel, stainless steel mesh, P70 silicone (Silicones, Inc., High Point, NC) and P592 silicone (Silicones, Inc., High Point, NC) – and allowed them to cure for at least one hour at room temperature (Figure 40). The overlapping surface area was then determined. An Instron 4400 Universal Testing Machine with a 30 kN load cell and mechanically tightened grips was used to measure force in tension versus displacement of the crosshead (Figure 41). The crosshead was raised at a rate of 0.1 mm/s until adhesive failure occurred. The resulting loads were integrated over the crosshead displacement to obtain a measurement of the work done on the system. This work divided by the initial adhesive cross- sectional area was the adhesion energy of the material-adhesive-epicardial system used for comparison with our adhesive load requirements.

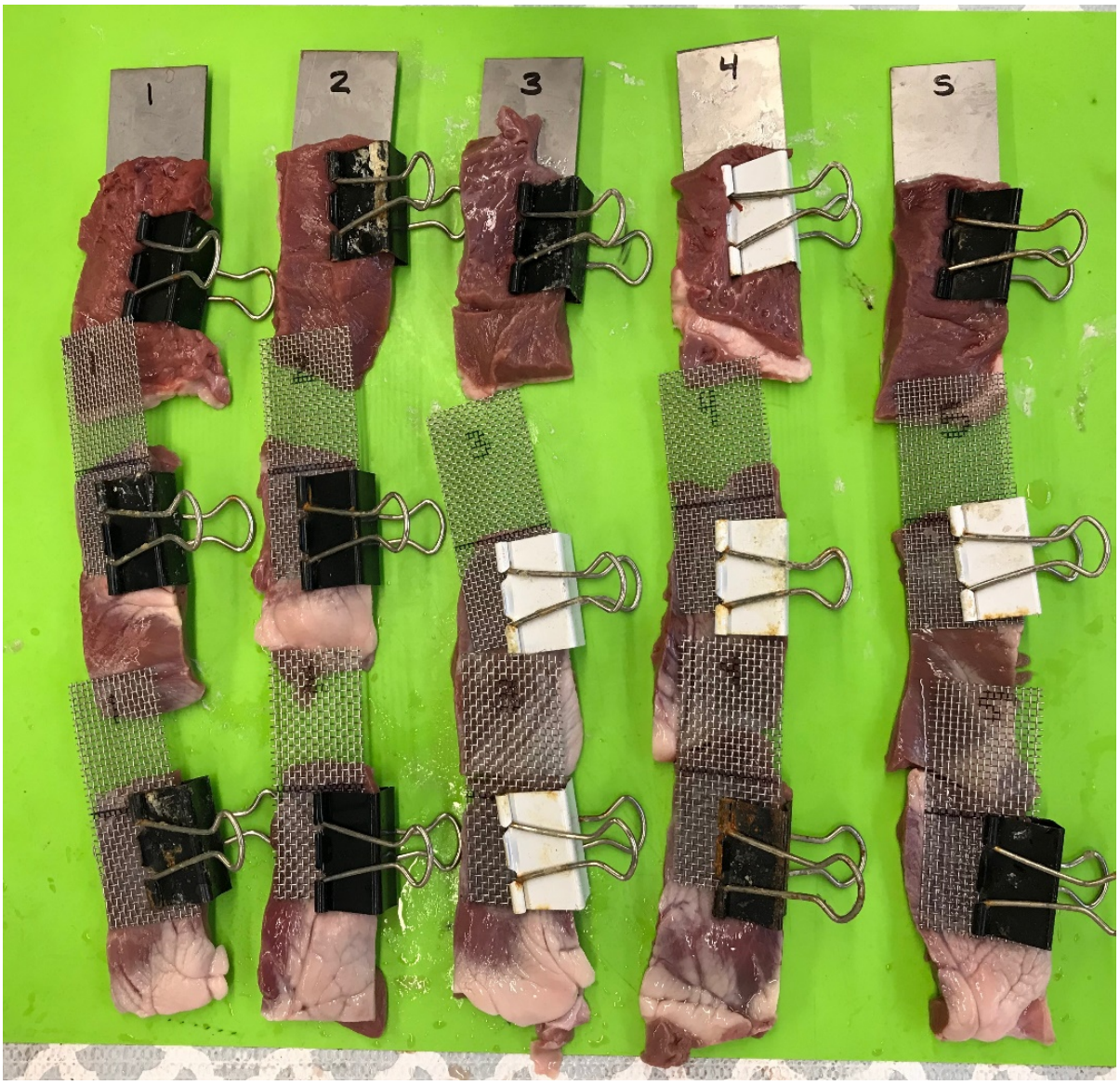

Figure 40: Rectangular samples of different substrates bonded with various adhesives to lamb epicardium prepared for testing.

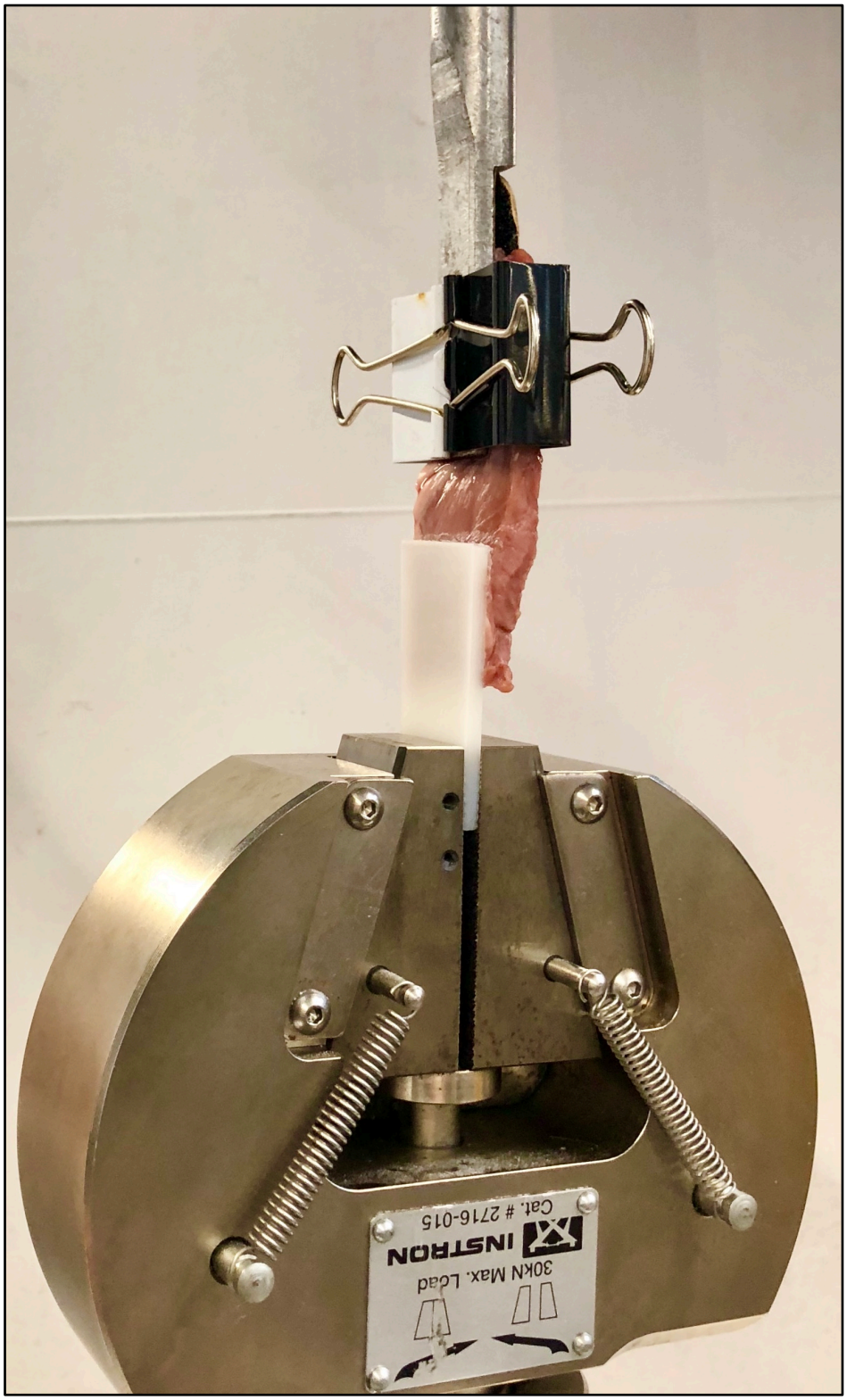

Figure 41: Experimental set up for lap shear testing of material- adhesive-epicardial systems using a 30 kN load cell on an Instron 4400 Universal Testing Machine.

Following the results of this initial lap-shear study, additional testing to determine the effects of adhesive curing time. For this set of experiments, rectangular slips of 316 stainless steel sheets (316S), 18 (18M) and 14 (14M) wires/inch stainless steel mesh, and P70 and P592 silicone were adhered to ovine epicardial tissue and cured for 5 and 60 minutes at room temperature and then tested with the same ASTM-F2255.

The final set of experiments evaluated the potential effectiveness of the material-adhesive-epicardial system when tested in a more physiologically realistic environment. This study compared *Vetbond*™ and *GLUture*™ (butyl and octyl/butyl cyanoacrylate adhesives, respectively) as they bond rectangular strips of 316 stainless steel sheets (316S), 18 mesh (18M), and 14 mesh (14M) stainless steel to ovine epicardial tissue. Stainless steel samples were selected for their overall performance in the first round of quantitative testing. In this second round of quantitative testing, adhesive was applied to a 900 mm^2 overlapping contact surface area of the specimens. The samples were then allowed to cure for 10 minutes in room air. The overlapping contact area was then wrapped with *Parafilm M®,* and the specimens were moved to a bath of 0.9% saline solution maintained at 35°C for 60 minutes. The same lap-shear protocols from the previous quantitative studies – ASTM-F2255 – were then used to determine the adhesion energy of the material-adhesive-epicardium systems. The resulting loads were integrated over crosshead displacement to determine the work done on the system, which was then divided by the initial contact area to determine the adhesion energy of the system.

7.2.2 Results

In these initial experiments, the following cyanoacrylate adhesives known for their strong adhesion to tissues were selected for testing: VetbondTM (99.9% by wt. N-butyl cyanoacrylate) and GlutureTM (60% by wt. 2-Octyl Cyanoacrylate and 40% by wt. N-butyl cyanoacrylate).

These adhesives were used to bond the cardiac tissue to stainless steel samples (smooth and meshed), all of which yielded adhesion energies above the upper bounds of our previously calculated adhesion energy requirements (Table 22). This suggests that stainless steel is potentially a good material candidate for a device that interfaces the heart and applies solely torsion. BenzMA (10% by wt. Benzocaine methacrylamide and 90% by wt. VetbondTM), which was provided by Dr. Stefanie Sydlik at Carnegie Mellon University (Pittsburgh, PA), was also tested. BenzMA is part of a novel family of therapeutic methacrylic (TMA) monomers, which allow for direct delivery of a therapeutic agent to the site of injury. Furthermore, TMAs allow for the tuning of adhesive mechanical properties; specifically BenzMA has been reported to have higher values of shear stress at failure and toughness when compared to VetbondTM [63]. BenzMA was used to bond different smooth silicone samples to the epicardium of lamb hearts to determine their resulting adhesion energies.

Overall, the silicones yielded adhesion energies below the lower bound of the adhesion energy requirements. However, it can be noted that the adhesion energy for P70 silicone was 10% less than the lower bound adhesion energy requirement, suggesting that P70 silicone surface modification, such as increased roughness or functionalization, might yield higher adhesion energies in the P70-BenzMA-epicardial system. We observed that the 14M could withstand the shear forces during systole when paired with Vetbond™ but would only be able to withstand shear forces at diastole when paired with GLUture™. Most of the tests failed due to mechanical failure of the adhesive. The rest experienced failure due to the epicardial samples ripping while the adhesive remained intact. Vetbond™ experienced 93.33% failure due to the adhesives failing, while GLUture™ tensile tests experienced only 60% adhesive failure. The decrease in the number of adhesive failures for GLUture™ suggests that it produces a more pliant bond.

Table 22: Adhesion energies generated from lap shear testing of material-adhesive-epicardial systems.

Adhesive	Adhesion Energy (J m^{-2})	
	Stainless Steel	**Stainless Steel Mesh**
Vetbond™	98.66	435.9
Gluture™	354.3	119.6
	P70 Silicone	**P592 Silicone**
BenzMA	48.09	0.0011

These initial quantitative tests were encouraging, so additional samples for each stainless steel-adhesive-epicardium system with varying amounts of adhesive curing time were tested. The results indicated that the majority of the samples tested (80%) exceeded these energy requirements, suggesting that the steel and P592 silicone surface materials combined with either adhesive could potentially secure the device to the heart during actuation (Table 23).

Table 23: Adhesive energy results from lap shear testing where adhesive curing time was varied

Adhesives	Cure time (min)	Average Adhesion Energies (J/m^2) (n=5)				
		Stainless Steel			Silicone	
		316S	**18M**	**14M**	**P70**	**P592**
Vetbond™	*5*	293.60	226.37	243.72	98.42	171.92
	60	270.07	343.27	357.05	115.71	203.55
GLUture™	*5*	270.07	32.30	22.02	75.22	148.49
	60	293.60	379.96	164.74	70.05	250.28

In the final set of adhesion testing where the material-adhesive-epicardium system was allowed to be hydrated during adhesive curing time, we determined that the 316S and 18M could potentially withstand the shear forces during peak systole when paired with either adhesive (Table 24). The 14M withstood shear forces during systole when paired with *Vetbond™* but

would only be able to withstand shear forces at diastole when paired with *GLUture*™. In this study, the majority of the material-adhesive-epicardium systems failed due to mechanical failure of the adhesive (Table 25). The remainder experienced failure caused by the epicardial samples ripping while the adhesive remained intact. *Vetbond*™ experienced 93.33% failure due to the adhesives failing, while *GLUture*™ tensile tests experienced only 60% adhesive failure. The decrease in the number of adhesive failures for *GLUture*™ suggests that it produces a more pliant bond.

Table 24: Adhesive energy results from lap shear testing where the adhesive was allowed to cure in a more physiologically realistic environment

Adhesive	Adhesion Energy (J m^{-2}) (n=5)		
	Stainless Steel		
	316S	18M	14M
Vetbond™	107.47	190.74	171.94
Gluture™	168.92	182.52	70.80

Table 25: Percent of tests that failed due to adhesive failure from lap shear testing where the adhesive was allowed to cure in a more physiologically realistic environment

Adhesive	Percent Failure (n=5)		
	Stainless Steel		
	316S	18M	14M
Vetbond™	100%	100%	80%
Gluture™	40%	60%	80%

7.3 Significance

Based on the initial experiments investigating the material-adhesive-epicardial systems, stainless steel has been identified as a good potential candidate for the construction of a torsional cardiac assist device. For these epicardial circulatory assist devices, one of the most important design considerations is how to engineer a secure method of attaching the device to the

epicardium without causing undue damage to the epicardial tissue and coronary arteries. Although the design of an epicardial cardiac assist device can be optimized to mechanically match material properties of the cardiac tissue, there will be an inherent mechanical mismatch between the epicardial tissue and the materials of the device due to the time varying stiffness of the myocytes during a cardiac cycle. This could result in a failure of adhesion of the device and catastrophic decrease in cardiac support. This mismatch will make it tough to rely solely on adhesives as the method of attachment. Instead, adhesives coupled with another means of mechanical attachment, whether with vacuum suction, suturing, velcro latching, etc., would prove beneficial. This multifaceted approach for device attachment would provide redundancy to the system as well as robustness to the time varying mechanical properties.

The results of the adhesion energy for the silicone demonstrate that both the material and adhesive properties are crucial to design a fully optimal system. These silicones are somewhat similar in their mechanical properties; however, they are drastically different in terms of how well they adhere to the epicardial surface. The P70-BenzMA system demonstrated superior adhesion energy when compared to the P592-BenzMA system. That being said, the adhesion energy will limit the amount of torsion the silicone-adhesive-epicardium interface can withstand. We have already established the upper and lower bounds for 80 degrees of applied apical torsion and the adhesion energy for the P70-BenzMA falls below this range. The conservative maximum rotation that this system could withstand is around 28 degrees. While this is only for compression via torsion, it is important to realize that characterizing the adhesion energy of the silicone-adhesive-epicardial system plays just as critical as a role in the device design as does the material properties, as both limit the dynamic actuation of direct cardiac compression.

The lap-shear tests for the stainless steel samples showed that the 316S and 18M combined with either adhesive could potentially secure the device to the epicardium during applied apical torsion. Observing the percent failure due to adhesive and tissue failure determined that the *Vetbond*™ created a stronger, but more brittle bond between the tissue and metal substrates, while the *GLUture*™ created a ductile bond between different components. Therefore, the results suggest that the 316S or 18M bonded with an octyl/butyl cyanoacrylate bioadhesive would be a better fit to secure an alternative CAD as it actuates on the heart.

7.3.1 Future Work

A true stress mapping of the epicardial surface at peak systole would yield a more powerful understanding of the loading requirements at the attachment interfaces. Although our calculations of stress and strain across the epicardial surface is a simplification and an estimate of the shear stress that the surface of the heart would experience, it does provide an initial adhesion energy requirement for design consideration. With that said, a more accurate mapping of the stresses and strains of the heart would allow for a better understanding of the time and spatially changing cardiac biomechanics providing insights to inform safer and more robust device designs.

Chapter 8

Summary and Conclusion

Inspired by the left ventricular twisting of the heart, AAT represents a novel approach for providing cardiac assist while avoiding blood contacting surfaces. A tVAD would theoretically be able to provide cardiac assist while avoiding blood activation through a less invasive surgical implant procedure. Furthermore, because the left ventricular twisting motion of the heart is lost in diseased states, the addition of AAT as a therapy also has the benefit of reintroducing the twisting motion to help reduce wall stresses and improve cardiac output. Previous initial proof-of-concept theoretical, computational, and experimental results demonstrated that AAT has the potential to provide cardiac assist to a failing heart [25]. In an effort to better understand the mechanisms by which AAT affects the heart and to determine design parameters for a second-generation tVAD, parametric computational simulations were performed to determine optimum device design parameters. This was achieved by using an established bi-ventricular computer model to quantify the effects of applied apical torsion on cardiovascular hemodynamics to determine optimum device parameters for hemodynamic performance and regional cardiac biomechanics to understand the working limits of such applied torsion for cardiac assist. Additionally, testing was conducted in an effort to develop a method for securely attaching the tVAD to the epicardial surface of the heart with minimal tissue damage.

In developing a computational simulation workflow for the interrogation of different design parameters for the tVAD, we were able to achieve two things. First, we were able to determine the optimal working parameters based on the tVAD's effects on global hemodynamics and establish the practical limits of the AAT therapy due to the resulting regional cardiac biomechanics. Based on the results of these computational parametric simulations, increasing levels of AAT assist appears to yield substantial increases in cardiovascular hemodynamic returns (Chapter 3). However, such supraphysiological-rotations result in very large maximum principal strains and stresses in certain regions of the heart, which suggests a potential for damage to the myocardial tissue. The implication is that AAT alone for cardiac assist, especially at large ARA of 65 degrees and above, may not be realistic (Chapter 4). However, even at lower angles of applied rotation, there was an increase in hemodynamic performance, which suggests that AAT at physiological or just slightly above physiological levels could help restore hemodynamic function slightly, but more importantly, help improve local regional biomechanics of the myocardium and (possibly) cause the heart to return towards a physiologically healthier state. This idea is especially promising when coupled with another epicardial cardiac assist mechanism, such as direct cardiac compression. Along this vein, a new tVAD prototype was designed based on the optimized device coverage area parameters (Chapter 6). Although this prototype of the tVAD solely utilizes AAT as a means for cardiac assist, it can be amended to include features for direct cardiac compression, as well. With regards to interfacing the device to the epicardium, based on our attachment studies, CA adhesives appear to provide a bond sufficient for the extreme surpa-rotation test cases, and should be more than sufficient for AAT at more physiologically normal levels of 10-15 degrees of rotation (Chapter 7).

Despite the shortcomings of the supraphysiological-rotations of the AAT cases tested here, results of these studies have yielded a better understanding of how tVAD assist would likely affect the heart, and beyond that, a computational workflow that can be used to evaluate the effects of other modes of cardiac assist that sit external to the circulation. This workflow was first developed using a simple left ventricular porcine prolate model, which was then scaled to be more anatomically and physiologically similar to that of a human heart. With these simple prolate models, design parameters of device coverage area, angles of applied rotation, and timing of AAT could be tuned to improve cardiac hemodynamic output (Chapters 2 & 5). With this established workflow, heart failure models were created to test the effectiveness (based on hemodynamic returns) and safety (based on the limits of the regional cardiac biomechanics) for a device that sits at the epicardium of the heart and provides cardiac assist through AAT (Chapters 3 & 4). The bi-ventricular model was further scaled to simulate a more severe level of HF, with a resulting LV EF was 15% (Chapter 5).. It is foreseeable that model parameters such as passive model parameters (bulk modulus), initial hemodynamic model parameters (Windkessel elements, vessel compliance, vessel resistance, etc.) , and cellular model parameters (cellular model type, maximum isometric tension (kPa) at longest sarcomere length, etc.) can be varied to correlate with other disease states, such as pulmonary hypertension.

Although the parametric computational studies to evaluate the tVAD, as designed, did not result in as encouraging a conclusion as we had hoped, the results still generated useful information about the potential and limitations of AAT, a computational workflow for applying ventricular rotations, and a better understanding of the computational limits of the computational workflow. Moving forward, it would be very informative to understand the effects of AAT at physiological levels on cardiovascular hemodynamics and regional cardiac biomechanics.

Furthermore, in parallel to the work investigating the effects of AAT, efforts have been made in our lab to evaluate the potential effectiveness of direct cardiac compression. In that vain, it would also be very useful to examine the utility of AAT combined with direct cardiac compression for cardiac assist, compare these different methods of cardiac assist. To facilitate this, the computational simulation workflow should prove to be a very useful tool for understanding how AAT, operating at more physiological levels and coupled with direct cardiac compression, would affect the hemodynamics and biomechanics of a failing heart. Additionally, because AAT is artificially restoring the ventricular twisting mechanism, it would be useful to understand the potential remodeling of the heart due to AAT and direction cardiac compression for different patient profiles. Furthermore, additional testing should be conducted to further evaluate the attachment method for MCS devices that interface with the epicardium. To that end, it would be useful to conduct tests that evaluated the effects of a cyclic load onto the substrate-adhesive-myocardium system.

Conclusion

This dissertation presents the key findings of my research for developing a second generation tVAD for cardiac assist. Thorough exploration of the design considerations for a second generation tVAD yielded a better understanding of how AAT affects cardiac hemodynamics and regional cardiac biomechanics, and hence the realistic limitations of this mode of cardiac assist. The results of the computational parametric studies concluded that AAT at large levels of assist could potentially provide substantial cardiovascular hemodynamic support, but at the cost of potentially damaging the myocardium. Although the application of such high levels of AAT alone are likely to be an unrealistic approach in practice, there is more work to be done to determine the utility of AAT at physiologic levels both as a standalone

therapy and/or coupled with direct cardiac compression. Beyond the design considerations of the tVAD, the workflow for the parametric computational simulations is an important tool that we can now use for future evaluations of similar devices and their potential effects on different heart failure models.

Appendix A

Parametric Study on Effects of tVAD Support on Cardiovascular Hemodynamics

A.1 Example of Python Script Used for Computational Parametric Simulations

The below script was originally written by Roy Kerckhoffs and amended by Lewis Waldman for the original proof of concept computational simulations of AAT, and is a representative example of the scripts used in the computational parametric simulations of AAT [25]. The script has been amended for the of simulations as described in Chapter 3.

```
---------------------------------------------------------------------------------------------------------------
#*************************************************************
class Unbuffered(object):
   def __init__(self, stream):
      self.stream = stream
   def write(self, data):
      self.stream.write(data)
      self.stream.flush()
   def __getattr__(self, attr):
      return getattr(self.stream, attr)

import sys
sys.stdout = Unbuffered(sys.stdout)

import os

import numpy
import math

parallel = True
#parallel = False

self.Load_File(r'C:\im04\BiV5_prolate80_lvad3_lrg_55_newmethod.cont6', log=0)

SimName = 'BiV5_prolate80_lvad3_lrg_55_newmethod_65'

outputDir = 'C:/im04/%s'%(SimName)

pi = math.pi
outputsteps = 10.0 # Number of steps output is requested (1.0 = every time step, 2.0 = every
other time step, etc)
iterations = 250 # Number of maximum iterations for FE solve to converge
time_increment = 0.5 # Time increment in ms.
#time_increment = 0.1666666667 # Time increment in ms.
errorMaxsumsol = 1.0e-3 # Convergence criterion on sum of incremental solutions
errorMaxresid = 1.0e-3 # Convergence criterion on residual forces
steps = 900 # Number of simulation steps to take. Note that total number of steps = steps times
outputsteps
#currentTime = 1500 # Initial time
currentTime = 0 # Initial time

bcnodes = [0,2,4,6] # Nodes defined in deformed coordinate 3 to prescribe boundary conditions
to (in this example, these are nodes 10,11,12,31,32,33)

#amplitude =0.0 # amplitude of sine in radians
amplitude =1.134464 # amplitude of sine in radians (this is 65 degrees in radians right now)
```

```
#amplitude = 5*pi/12.0 # amplitude of sine in radians; this is 75 degrees (3/12, 4/12, 5/12 sames as 45, 60, 75 degrees)
#amplitude = pi/4.0 # amplitude of sine in radians
#amplitude =0.959931 # amplitude of sine in radians (55 degrees)
#amplitude = pi/3.0 # amplitude of sine in radians
#amplitude = pi/6.0 # amplitude of sine in radians
period = 750 # Basic Cycle Length [ms]
peaktime = 187.5 # Time in cardiac cycle of peak rotational amplitude [ms]

#define parameters
#outputDir = '%s'%(SimName)
try:
   os.mkdir(outputDir)
except OSError:
   sys.stderr.write("Warning %s already exists!\n"%outputDir)

#Load, send, and calculate mesh

#self.Load_File('.cont6',log=0) # This is the cont file this script runs with
self.Send(None, log=0)
self.CalcMesh([('Calculate', None), ('Do not Calculate', None), ('Calculate', None), ('Global arc length scale factors (for nodal derivs wrt arc lengths)', None)], log=0)

#Perform simulations
StartStep = int(currentTime/(outputsteps*time_increment))
for step in range(StartStep+1,StartStep+steps+1):
      Time = currentTime + time_increment*outputsteps
      Time_local = Time % period
      for node in range(len(bcnodes)):
         if Time_local<peaktime:
            self.stored_data.init.obj.dc3.nodes[bcnodes[node]].value = amplitude*pi/(2.0*peaktime)*sin(2.0*pi*Time_local/(2.0*peaktime))
         else:
            self.stored_data.init.obj.dc3.nodes[bcnodes[node]].value = -amplitude/(period-peaktime)
         #self.stored_data.init.obj.dc3.nodes[bcnodes[node]].value = 0.005
         print(self.stored_data.init.obj.dc3.nodes[bcnodes[0]].value)

      self.stored_data.store(self.stored_data.init.obj)
      self.Send(None, log=0)

      self.Snonlin([outputsteps, iterations, time_increment,  currentTime, Time, errorMaxsumsol, errorMaxresid,1, {'delta':1e-6,'info': 'gui_biomechanics_sol', 'sol_tol': 10, 'linear_solver': 0, 'update_param': 0.0, 'solution_output': 1, 'Krylovi_subspace': 10, 'trans_routine': 0, 'min_i_eigen': 0.0, 'max_r_eigen': 0.0, 'max_i_eigen': 0.0, 'solver_iterations': 200, 'vector_output': 3, 'abort': 1,
```

```
'line_search': 1, 'stopping': 1, 'min_r_eigen': 0.0, 'additibe_const': 0.0, 'Newton_Raphson': 0,
'preconditioning': 0, 'equilibrium': 2, 'parallel':parallel}], log=0)
        #self.UICWithSolution(log = False)
        #self.LnodalSolution(log=0, scripting = True, writeFile = "temp2.xls")
        self.LnodalSolution(log=0, scripting = True, writeFile = "temp.xls")
        self.LnodalSolution(log=0, scripting = True, writeFile =
"%s/nodes_%s_%d.xls"%(outputDir, SimName, step))
        self.UICWithFile(r'temp.xls',log = False)

        currentTime = Time
        #self.LcauchyStress("%s/stress_%s_%d.xls"%(outputDir, SimName, step), log = 0)
        #self.Lstrain(log=0, writeFile = "%s/strains_%s_%d.xls"%(outputDir, SimName, step))
        #self.Lstress("%s/stresses_%s_%d.xls"%(outputDir, SimName, step), log=0)
        #self.LnodalSolution(log=0, scripting = True, writeFile =
"%s/nodes_%s_%d.xls"%(outputDir, SimName, step))
        #self.Relem([0, 1, 3, 3, [0.0], ['all']],log = False)
```

A.2 Comments on Image J for Stroke Work Calculations

This method is considerably easier than using MatLab for the same purpose and just as accurate. When using the latter, it is necessary to perform two integrations using the trapz function for nonuniform grids. It is also vital to consider precise outflow valve openings and closings to isolate the ejection curves and inflow valve openings and closings to isolate the filling curves. But, this is unnecessary when Image J is used to get the entire area of each PV-loop with a single click of the Wand tool and use of the Measure function. When done properly, Image J gives virtually identical results to the more cumbersome use of MatLab for this purpose. In the case of the largest rotation and largest CA, results from Matlab were compared with Image J. They were virtually identical, 9145 mmHg-ml using Image J and 9171 mmHg-ml using MatLab, a difference of less than 0.3%.

Appendix B

Further Evaluation of the Effects of tVAD for Cardiac Assist

B.1 Example of Python Script Used for Varying the Timing of AAT

The below lines of logic were added to the Python Script used for the computational parametric simulations. They initial parameters were amended depending on the simulation. To change the time at which max rotation angles would be applied, PT was simply changed in the line of logic to the desired value.

---

peaktime = 287.5 # Time in cardiac cycle of peak rotational amplitude [ms] original pt = 187.5

In order to apply a hold time after the prescribed maximum rotation angle was applied, two definitions of PT were set. The first value is the original peaktime, while the second value is the time at which the device should begin being returned to its initial position.

---

peaktime = 187.5 # Time in cardiac cycle of peak rotational amplitude [ms] original pt = 187.5
peaktime2 = 387.5 # PT + hold time of 200 before returning to 0 [ms] *chose 200 ms because peak pressures in 75D simulation ~375 ms point

---

These values are then fed into the lines of logic that describe how the torsion is applied during the cardiac cycle. The bolded portion of the script below are the amended lines of logic that allow for the simulated device to be rotated to the prescribed rotation angle, then held in place for a specified time after rotation, and then returned to its starting position.

```
#Perform simulations
StartStep = int(currentTime/(outputsteps*time_increment))
for step in range(StartStep+1,StartStep+steps+1):
        Time = currentTime + time_increment*outputsteps
        Time_local = Time % period

         for node in range(len(bcnodes)):

        if Time_local<peaktime: #From start of cardiac cycle to PT - applied apical torsion
(during systole)
                    self.stored_data.init.obj.dc3.nodes[bcnodes[node]].value =
amplitude*pi/(2.0*peaktime)*sin(2.0*pi*Time_local/(2.0*peaktime))
                        temporary
=amplitude*pi/(2.0*peaktime)*sin(2.0*pi*Time_local/(2.0*peaktime))

      elif Time_local>peaktime and Time_local<peaktime2: #From PT to PT2 - after
rotation, the heart is held in the rotated state
                    self.stored_data.init.obj.dc3.nodes[bcnodes[node]].value =  temporary

       else: #From PT2 to end of cardiac cycle - ventricle is untwisted to initial state
                    self.stored_data.init.obj.dc3.nodes[bcnodes[node]].value = -
amplitude/(period-peaktime)

                #self.stored_data.init.obj.dc3.nodes[bcnodes[node]].value = 0.005
                print(self.stored_data.init.obj.dc3.nodes[bcnodes[0]].value)
```

References

1. Centers for Disease Control and Prevention (2016) Heart Failure Fact Sheet. Centers for Disease Control and Prevention.

2. Mayo Clinic Staff (2016) Heart Failure. Treatments and Drugs. Mayo Clinic, n.d. Web.

3. Texas Heart Institute (2016) Heart Assist Devices - Texas Heart Institute. Texas Heart Institute.

4. Bentley, T. Scott. “2017 U.S. Organ and Tissue Transplant Cost Estimates and Discussion.” 2017 U.S. Organ and Tissue Transplant Cost Estimates and Discussion, Milliman, 3 Aug. 2017, www.milliman.com/insight/2017/2017-U_S_-organ-and-tissue-transplant-cost-estimates-and-discussion/.

5. “Transplant Trends.” Transplant Trends, UNOS, 29 Oct. 2018, unos.org/data/transplant-trends/.

6. “Organ Procurement and Transplantation Network.” National Data - OPTN, OPTN: Organ Procurement and Transplantation Network - OPTN, optn.transplant.hrsa.gov/data/view-data-reports/national-data/.

7. Trivedi, J.r., et al. “Risk Factors of Waiting List Mortality for Patients Awaiting Heart Transplant.” The Journal of Heart and Lung Transplantation, vol. 35, no. 4, 2016, doi:10.1016/j.healun.2016.01.602.

8. "What Is a Ventricular Assist Device?" - NHLBI, NIH. N.p., n.d. Web. 10 Aug. 2015.

9. Broglio, Kathleen, DNP, ANP-BC, ACHPN, Frances Eichholz-Heller, MSW, LMSW, ACHP-SW, and Shunichi Nakagawa, MD. "Left Ventricular Assist Devices." Journal of Hospice & Palliative Nursing 17.5 (2015): 380-81. Print.

10. Wever-Pinzon, Omar, et al. “Cardiac Recovery During Long-Term Left Ventricular Assist Device Support.” Journal of the American College of Cardiology, vol. 68, no. 14, 2016, pp. 1540–1553., doi:10.1016/j.jacc.2016.07.743.

11. Redman, Emily. “To Save His Dying Sister-In-Law, Charles Lindbergh Invented a Medical Device.” Smithsonian.com, Smithsonian Institution, 9 Sept. 2015, www.smithsonianmag.com/smithsonian-institution/save-his-dying-sister-law-charles-lindbergh-Invented-medical-device-180956526/.

12. Kirklin, James K., and David C. Naftel. “Mechanical Circulatory Support.” Circulation: Heart Failure, vol. 1, no. 3, 2008, pp. 200–205., doi:10.1161/circheartfailure.108.782599.

13. “Comparison of Popular LVADs.” Reliant Heart, reliantheart.com/for-medical-professionals/comparison-of-popular-european-lvads/.

14. Rigatelli, Gianluca et al. “Past and present of cardiocirculatory assist devices: a comprehensive critical review” Journal of geriatric cardiology : JGC vol. 9,4 (2012): 389-400.

15. Wiedemann, Dominik, et al. “Ventricular Assist Devices – Evolution of Surgical Heart Failure Treatment.” European Cardiology Review, vol. 9, no. 1, 2014, p. 54., doi:10.15420/ecr.2014.9.1.54.

16. Kirklin, James K., et al. “Eighth Annual INTERMACS Report: Special Focus on Framing the Impact of Adverse Events.” The Journal of Heart and Lung Transplantation, vol. 36, no. 10, 2017, pp. 1080–1086., doi:10.1016/j.healun.2017.07.005.

17. Zlotin, B. and Zusman, A. (2008). Directed Evolution®. In Encyclopedia of Statistics in Quality and Reliability (eds F. Ruggeri, R. S. Kenett and F. W. Faltin). doi:10.1002/9780470061572.eqr418

18. United States, Food and Drug Administration. “Guidance for Industry - Q9 Quality Risk Management .” Guidance for Industry - Q9 Quality Risk Management , Food and Drug Administration, June 2006. www.fda.gov/downloads/Drugs/Guidances/ucm073511.pdf.

19. Kamm, Daniel. “Https://Fda-Consultant.com/risk1.Pdf.” An Introduction to Risk/Hazard Analysis for Medical Devices, FDA-Consultant, 6 May 2005, fda-consultant.com/risk1.pdf.

20. United States, Food and Drug Administration. “SUMMARY OF SAFETY AND EFFECTIVENESS DATA (SSED) - Heartware HVAD.” SUMMARY OF SAFETY AND EFFECTIVENESS DATA (SSED) - Heartware HVAD, Food and Drug Administration, 2012.

21. United States, Food and Drug Administration. “SUMMARY OF SAFETY AND EFFECTIVENESS DATA (SSED) - Heartware HVAD.” SUMMARY OF SAFETY AND EFFECTIVENESS DATA (SSED) – Thoratec Heartmate III, Food and Drug Administration, 2017.

22. Ulrich Geisen, Claudia Heilmann, Friedhelm Beyersdorf, Christoph Benk, Michael Berchtold-Herz, Christian Schlensak, Ulrich Budde, Barbara Zieger; Non-surgical bleeding in patients with ventricular assist devices could be explained by acquired von Willebrand disease, European Journal of Cardio-Thoracic Surgery, Volume 33, Issue 4, 1 April 2008, Pages 679–684, https://doi.org/10.1016/j.ejcts.2007.12.047

23. Genovese, Elizabeth A., et al. “Incidence and Patterns of Adverse Event Onset During the First 60 Days After Ventricular Assist Device Implantation.” The Annals of Thoracic Surgery, vol. 88, no. 4, 2009, pp. 1162–1170., doi:10.1016/j.athoracsur.2009.06.028.

24. Sengupta, Partho P., et al. “Twist Mechanics of the Left Ventricle.” JACC: Cardiovascular Imaging, vol. 1, no. 3, 2008, pp. 366–376., doi:10.1016/j.jcmg.2008.02.006.

25. Trumble DR, McGregor WE, Kerckhoffs RP, Waldman LK. Cardiac Assist With a Twist: Apical Torsion as a Means to Improve Failing Heart Function. ASME. J Biomech Eng. 2011;133(10):101003-101003-10. doi:10.1115/1.4005169.

26. Criscione, John C., and Saurabh Biswas. Device for Proactive Modulation of Cardiac Strain Patterns. Texas A&M University System, assignee. Patent US12242197. 29 May 2012. Print.

27. Roche, Ellen T., et al. “Soft Robotic Sleeve Supports Heart Function.” Science Translational Medicine, American Association for the Advancement of Science, 18 Jan. 2017, stm.sciencemag.org/content/9/373/eaaf3925.short. Accessed 30 Dec. 2018.

28. Horvath, M.A., Varela, C.E., Dolan, E.B. et al. Ann Biomed Eng (2018) 46: 1534. https://doi.org/10.1007/s10439-018-2046-2

29. McCulloch, Andrew, et al. “Introduction to Cardiac Physiology and Modeling with Continuity 6.3.” Continuity: Introduction to Cardiac Modeling. 2014, https://continuity.ucsd.edu/continuity-documentation/theory/

30. Guccione JM, McCulloch AD, and Waldman LK. (1991) Passive material properties of intact ventricular myocardium determined from a cylindrical model. J Biomech Eng Trans 113: 42–55.

31. Doll S and Schweizerhof K. (1999) On the development of volumetric strain energy functions. J Appl Mech 67(1): 17-21.

32. Bergel DA and Hunter PJ (1979). The mechanics of the heart, in Quantitative Cardiovascular Studies, Clinical and Research Applications of Engineering Principles (N. H. C. Hwang, D. R. Gross and D. J. Patel, eds), University Park Press, Baltimore, chapter 4, pp. 151–213.

33. Hunter PJ (1995), Myocardial constitutive laws for continuum mechanics models of the heart, in Molecular and Subcellular Cardiology: Effects of Structure and Function (S. Sideman and R. Beyar, eds), Plenum Press, chapter 30, pp. 303–318.

34. Walker JC, Ratcliffe MB, Zhang P, Wallace AW, Fata B, Hsu EW, Saloner D, and Guccione JM. (2005) MRI-based finite-element analysis of left ventricular aneurysm. Am J Physiol Heart Circ Physiol. 289:H692–H700.

35. Kerckhoffs RCP, Neal M, Gu Q, Bassingthwaighte JBB, Omens JH, McCulloch AD (2007) Coupling of a three- dimensional finite element model of cardiac ventricular mechanics to lumped systems models of the systemic and pulmonic circulation. Ann Biomed Eng 35:1-18 (PMCID: 2872168).

36. Bovendeerd PHM, Arts T, Huyghe JM, van Campen DH, Reneman RS. Dependence of local left ventricular wall mechanics on myocardial fiber orientation – a model study. J Biomech 1992; 25:1129–1140.

37. Givertz,MM (2011) Ventricular Assist Devices: Important Information for Patients and Families. Circulation 124.12 (2011): e305-e311

38. Kerckhoffs RCP (2010) Patient-Specific Modeling of the Cardiovascular System: Technology-Driven Personalized Medicine. Springer Science & Business Media.

39. Krishnamurthy A, Villongco CT, Chuang J, Frank LR, Nigam V, Belezzuoli E, Stark P, Krummen DE, Narayan S, Omens JH, McCulloch AD, Kerckhoffs RCP (2012) Patient-specific models of cardiac biomechanics. J Comput Physics 244:4-21 (PMCID: 3667962) doi:10.1016/j.jcp.2012.09.015.

40. Villongco, Christopher T et al. “Patient-specific modeling of ventricular activation pattern using surface ECG-derived vectorcardiogram in bundle branch block” Progress in biophysics and molecular biology vol. 115,2-3 (2014): 305-13.

41. Barge-Caballero, Eduardo, et al. “Preoperative INTERMACS Profiles Determine Postoperative Outcomes in Critically Ill Patients Undergoing Emergency Heart Transplantation.” Circulation: Heart Failure, vol. 6, no. 4, 2013, pp. 763–772., doi:10.1161/circheartfailure.112.000237.

42. Chemla, Denis, Jean-Louis Hébert, Catherine Coirault, Karen Zamani, Isabelle Suard, Patrice Colin, and Yves Lecarpentier. "Total Arterial Compliance Estimated by Stroke Volume-to-aortic Pulse Pressure Ratio in Humans." Am J Physiol Heart Circ Physiol 274.2 (1998): H500-505.

43. Dabestani, Ali, Gregory Mahan, Julius M. Gardin, Katsu Takenaka, Cora Burn, Alice Allfie, and Walter L. Henry. "Evaluation of Pulmonary Artery Pressure and Resistance by Pulsed Doppler Echocardiography." Am J Cardiol 59.6 (1987): 662-68.

44. Del Río, Miguel, Domingo Liotta, and Claudio O. Cervino. "VASCULAR RESISTANCE AND VASCULAR IMPEDANCE." A Practical Textbook of Congenital and Acquired Diseases of the Aorta. Buenos Aires, Argentina: U of, 2003. 52-53. Print.

45. Finkelstein, Stanley M., Jay N. Cohn, V.ross Collins, Peter F. Carlyle, and Wenda J. Shelley. "Vascular Hemodynamic Impedance in Congestive Heart Failure." Am J Cardiol 55.4 (1985): 423-27.

46. Freis, Edward D., Harold W. Schnaper, Robert L. Johnson, and George E. Schreiner. "Hemodynamic Alterations In Acute Myocardial Infarction. I. Cardiac Output, Mean Arterial Pressure, Total Peripheral Resistance, Central And Total Blood Volumes, Venous Pressure And Average Circulation Time 12." J Clin Invest 31.2 (1952): 131-40.

47. Gamble, G., J. Zorn, G. Sanders, S. Macmahon, and N. Sharpe. "Estimation of Arterial Stiffness, Compliance, and Distensibility from M- Mode Ultrasound Measurements of the Common Carotid Artery." Stroke 25.1 (1994): 11-16.

48. Lehmann, E. D., K. D. Hopkins, A. Rawesh, R. C. Joseph, K. Kongola, S. W. Coppack, and R. G. Gosling. "Relation Between Number of Cardiovascular Risk Factors/Events and Noninvasive Doppler Ultrasound Assessments of Aortic Compliance." Hypertension 32.3 (1998): 565-69.

49. Liu, Z. R., C. T. Ting, S. X. Zhu, and F. C. Yin. "Aortic Compliance in Human Hypertension." Hypertension 14.2 (1989): 129-36.

50. London, G. M., M. E. Safar, A. C. Simon, J. M. Alexandre, J. A. Levenson, and Y. A. Weiss. "Total Effective Compliance, Cardiac Output and Fluid Volumes in Essential Hypertension." Circulation 57.5 (1978): 995-1000.

51. Murgo, J. P., N. Westerhof, J. P. Giolma, and S. A. Altobelli. "Effects of Exercise on Aortic Input Impedance and Pressure Wave Forms in Normal Humans." Circ Res 48.3 (1981): 334-43.

52. Normal Hemodynamic Parameters and Laboratory Values. Irvine, CA: Edwards Lifesciences LLC, 2009. Print.

53. O'rourke, M. F., J. A. Staessen, C. Vlachopoulos, D. Duprez, and G. E. E. Plante. "Clinical Applications of Arterial Stiffness; Definitions and Reference Values." Am J Hypertens 15.5 (2002): 426-44.

54. Tanaka, H., F. A. Dinenno, K. D. Monahan, C. M. Clevenger, C. A. Desouza, and D. R. Seals. "Aging, Habitual Exercise, and Dynamic Arterial Compliance." Circulation 102.11 (2000): 1270-275.

55. Usyk TP, Mazhari R, and McCulloch AD. (2000) Effect of laminar orthotropic myofiber architecture on regional stress and strain in the canine left ventricle. J Elasticity 61: 143–164.

56. Cao Y, Miller MI, Winslow RL, Younes L. Large deformation diffeomorphic metric mapping of vector fields. Medical Imaging, IEEE Transactions on. 2005;24(9):1216–1230.

57. Alexander DC, Pierpaoli C, Basser PJ, Gee JC. Spatial Transformations of Diffusion Tensor Magnetic Resonance Images. IEEE Transactions on Medical Imaging. 2001;20(11):1131–1139.

58. Horvath MA, Roche ET, Vogt DM, Mooney DJ, Pigula FA, Walsh CJ. (2015) Soft Pressure Sensing Sleeve for Direct Cardiac Compression Device. ASME. International Design Engineering Technical Conferences and Computers and Information in Engineering Conference, Volume 3: 17th International Conference on Advanced Vehicle Technologies; 12th International Conference on Design Education; 8th Frontiers in Biomedical Devices ():V003T14A011. doi:10.1115/DETC2015-47567

59. Mayo Clinic Staff (2016) Heart Failure. Treatments and Drugs. Mayo Clinic, n.d. Web. http://www.mayoclinic.org/diseases- conditions/ heart- failure/basics/treatment/con-20029801. Accessed 08 August 2016

60. Soohoo E, Ma H, Alcasid A, Trumble DR (2016) Torsional Ventricular Assist Device (tVAD): Design Considerations and Prototype Development. J. Med Dev MED-16-1057. doi: 10.1115/1.4033117

61. Soohoo, Elaine, Lewis K. Waldman, and Dennis R. Trumble. "Computational Parametric Studies Investigating the Global Hemodynamic Effects of Applied Apical Torsion for Cardiac Assist." Annals of Biomedical Engineering (2017)

62. Chen, Qizhi, and George A. Thouas. “Metallic Implant Biomaterials.” Materials Science and Engineering: R: Reports, vol. 87, 2015, pp. 1–57., doi:10.1016/j.mser.2014.10.001.

63. Wright, Zoe M., Brian D. Holt, and Stefanie A. Sydlik. "Covalently-controlled Drug Delivery via Therapeutic Methacrylic Tissue Adhesives." J. Mater. Chem. B 5.37 (2017): 7743-755

64. Trumble, Dennis R. "Development and Testing of a Muscle- powered Cardiac Assist Device." Diss. Carnegie Mellon U, 2010.

65. ASTM F2255-05(2015) Standard Test Method for Strength Properties of Tissue Adhesives in Lap-Shear by Tension Loading, ASTM International, West Conshohocken, PA, 2015, https://doi.org/10.1520/F2255-05R15